

Melt Origin across a Rifted Continental Margin: a Case for Subduction-related Metasomatic Agents in the Lithospheric Source of Alkaline Basalt, NW Ross Sea, Antarctica

Kurt S. Panter^{1*}, Paterno Castillo², Susan Krans³, Chad Deering⁴, William McIntosh⁵, John W. Valley⁶, Kouki Kitajima⁶, Philip Kyle⁷, Stan Hart⁸ and Jerzy Blusztajn⁸

¹Department of Geology, Bowling Green State University, Bowling Green, OH 43403, USA; ²Scripps Institute of Oceanography, University of California San Diego, La Jolla, CA 92093, USA; ³Department of Earth and Environmental Sciences, Michigan State University, East Lansing, MI 48824, USA; ⁴Department of Geology & Mining Engineering & Sciences, Michigan Tech University, Houghton, MI 49931, USA; ⁵New Mexico Bureau of Geology & Mineral Resources, Socorro, NM 87801, USA; ⁶Department of Geoscience, University of Wisconsin, Madison, WI 53706, USA; ⁷Department of Earth & Environmental Science, New Mexico Tech, Socorro, NM 87801, USA; ⁸Woods Hole Oceanographic Institution, Woods Hole, MA 02543, USA

*Corresponding author. Telephone: 01 419 372 7337. E-mail: kpanter@bgsu.edu

Received August 4, 2017; Accepted March 23, 2018

ABSTRACT

Alkaline magmatism associated with the West Antarctic rift system in the NW Ross Sea (NWRS) includes a north–south chain of shield volcano complexes extending 260 km along the coast of Northern Victoria Land (NVL), numerous small volcanic seamounts located on the continental shelf and hundreds more within an ~35 000 km² area of the oceanic Adare Basin. New ⁴⁰Ar/³⁹Ar age dating and geochemistry confirm that the seamounts are of Pliocene–Pleistocene age and petrogenetically akin to the mostly middle to late Miocene volcanism on the continent, as well as to a much broader region of diffuse alkaline volcanism that encompasses areas of West Antarctica, Zealandia and eastern Australia. All of these continental regions were contiguous prior to the late-stage breakup of Gondwana at ~100 Ma, suggesting that the magmatism is interrelated, yet the mantle source and cause of melting remain controversial. The NWRS provides a rare opportunity to study cogenetic volcanism across the transition from continent to ocean and consequently offers a unique perspective from which to evaluate mantle processes and the roles of lithospheric and sub-lithospheric sources for mafic alkaline magmas. Mafic alkaline magmas with > 6 wt % MgO (alkali basalt, basanite, hawaiiite, and tephrite) erupted across the transition from continent to ocean in the NWRS show a remarkable systematic increase in silica-undersaturation, P₂O₅, Sr, Zr, Nb and light rare earth element (LREE) concentrations, as well as LREE/HREE (heavy REE) and Nb/Y ratios. Radiogenic isotopes also vary, with Nd and Pb isotopic compositions increasing and Sr isotopic compositions decreasing oceanward. These variations cannot be explained by shallow-level crustal contamination or by changes in the degree of mantle partial melting, but are considered to be a function of the thickness and age of the mantle lithosphere. We propose that the isotopic signature of the most silica-undersaturated and incompatible element enriched basalts best represent the composition of the sub-lithospheric magma source with low ⁸⁷Sr/⁸⁶Sr (≤0.7030) and δ¹⁸O_{olivine} (≤5.0‰), and high ¹⁴³Nd/¹⁴⁴Nd (~0.5130) and ²⁰⁶Pb/²⁰⁴Pb (≥20). The isotopic ‘endmember’ signature of the sub-lithospheric source is derived from recycled subducted materials and was transferred to the lithospheric mantle by small-degree melts (carbonate-rich silicate liquids) to form amphibole-rich metasomes. Later melting of the metasomes produced silica-undersaturated

liquids that reacted with the surrounding peridotite. This reaction occurred to a greater extent as the melt traversed through thicker and older lithosphere continentward. Ancient and/or more recent (~550–100 Ma) subduction along the Pan-Pacific margin of Gondwana supplied the recycled subduction-related material to the asthenosphere. Melting and carbonate metasomatism were triggered during major episodes of extension beginning in the Late Cretaceous, but alkaline magmatism was very limited in its extent. A significant delay of ~30 to 20 Myr between extension and magmatism was probably controlled by conductive heating and the rate of thermal migration at the base of the lithosphere. Heating was facilitated by regional mantle upwelling, possibly driven by slab detachment and sinking into the lower mantle and/or by edge-driven mantle flow established at the boundary between the thinned lithosphere of the West Antarctic rift and the thick East Antarctic craton.

Key words: $^{40}\text{Ar}/^{39}\text{Ar}$ ages; geochemistry; Sr–Nd–Pb–O isotopes; West Antarctic rift system

INTRODUCTION

The source and processes that generate alkaline magmas in intraplate continental settings, particularly in young rifts such as East Africa and West Antarctica, remain enigmatic. The debate revolves broadly around whether melt is produced within the asthenospheric or lithospheric mantle, whether the melting and ultimately eruption is triggered by passive extension, lithospheric drip or upwelling plumes, and is further perpetuated by the uncertainty in how melt is modified as it rises through the continental plate. The Late Cenozoic magmatism found within the West Antarctic Rift System (WARS, Fig. 1a) has been explained by a variety of models that attempt to reconcile the petrology, geochemistry and isotopic signatures of mafic alkaline rocks within the context of the last several hundred million years of Antarctica's tectonic history, specifically the tectonic events leading up to and including the breakup of the proto-Pacific margin of Gondwana, which separated Zealandia from West Antarctica in the Late Cretaceous.

A unifying model for WARS magmatism is warranted given the relative uniformity of mafic alkaline compositions emplaced within a very broad (~1500 × 2500 km) region of thinned continental lithosphere over the last 48 Myr. The mafic compositions are similar to ocean island basalts (OIB) and have HIMU-like isotopic affinities ($^{206}\text{Pb}/^{204}\text{Pb} > 19.5$, $^{87}\text{Sr}/^{86}\text{Sr} < 0.7035$, $^{143}\text{Nd}/^{144}\text{Nd} > 0.5128$). Furthermore, the magmatism has been linked compositionally and tectonically to a much broader region of long-lived, diffuse, alkaline volcanism that encompasses West Antarctica, Zealandia and eastern Australia (Finn *et al.*, 2005). Existing models for WARS magmatism and beyond, however, are varied but can be distilled into two fundamental types: those that involve mantle plumes and those that do not. Both types require mantle sources for the alkaline magmas that have been enriched in incompatible minor and trace elements relative to primitive mantle to explain their geochemical and radiogenic isotope compositions. For the mantle plume source, enrichments are considered to be via addition of oceanic crust and

sediment subducted and recycled deep within the mantle (Hofmann & White, 1982; Zindler & Hart, 1986; Weaver, 1991; Chauvel *et al.*, 1992; Willbold & Stracke, 2010). Models proposed for West Antarctica include a mantle plume beneath the active Erebus volcano (Kyle *et al.*, 1992), a large plume that may have helped initiate and control the position of continental break-up in the Late Cretaceous (Lanyon *et al.*, 1993; Weaver *et al.*, 1994; Storey *et al.*, 1999) and older 'fossil' plumes proposed to have underplated and accreted to the base of the Gondwana lithosphere prior to break-up (Rocholl *et al.*, 1995; Hart *et al.*, 1997; Panter *et al.*, 2000; Kipf *et al.*, 2014). For non-plume sources the enrichment has been ascribed to mantle metasomatism caused either by small degrees of melting during the early phase of rifting prior to continental break-up (Rocchi *et al.*, 2002; Nardini *et al.*, 2009) or by slab-derived fluids related to a prolonged period of subduction that occurred prior to rifting (Finn *et al.*, 2005; Panter *et al.*, 2006; Martin *et al.*, 2013, 2014; Aviado *et al.*, 2015).

In this study we offer a unique perspective on this debate through interpretation of geochemical, isotopic (Sr, Nd, Pb and O), and age ($^{40}\text{Ar}/^{39}\text{Ar}$) data for basalts erupted across the transition from oceanic lithosphere to thinned continental lithosphere adjacent to the East Antarctic craton. The Neogene alkaline magmatism of the NW Ross Sea (NWRS) include deposits on land as well as numerous seamounts on the continental shelf and hundreds more located within the oceanic Adare Basin (Fig. 1b). Oceanic basalt from the NWRS have been shown to be of the same age and petrogenetically akin to basalt from the rest of the WARS (Panter & Castillo, 2007). Apart from the Cameroon volcanic line in West Africa (Fitton & Dunlop, 1985; Njome & de Wit, 2014) we know of no other place on Earth where contemporaneous, small-volume, alkaline volcanism occurs across a rifted continental margin, and in particular, a region that has experienced a relatively recent and rapid transition (~110–80 Ma) from subduction to extension to break-up without voluminous magmatism (i.e. no flood basalts; Finn *et al.*, 2005). Thus the geochronology and petrology of NWRS basalts allow for a novel assessment of lithospheric (continental and

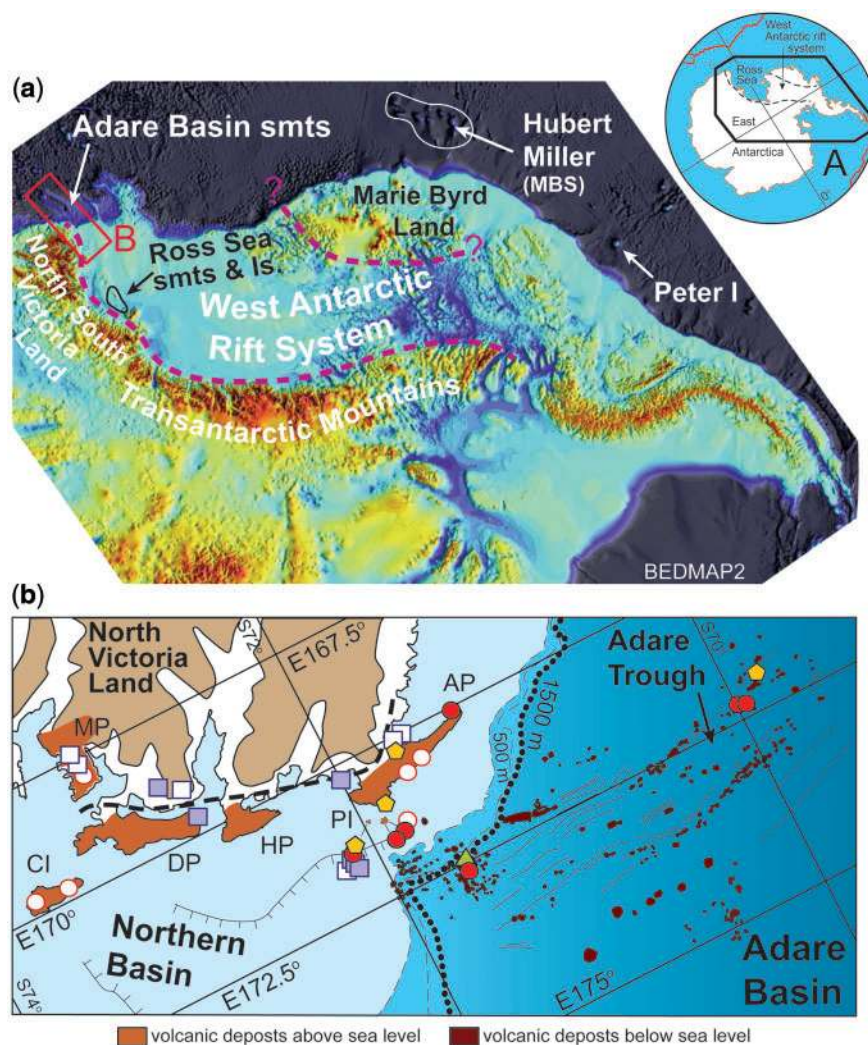


Fig. 1. Regional and sample location maps. (a) Subglacial surface elevation map (BEDMAP2; Fretwell *et al.*, 2013) with the approximate boundaries of the West Antarctic rift system delimited by red dashed lines. Also shown are locations of oceanic volcanic fields (seamounts and islands) that are compared in this study. MBS, Marie Byrd Seamounts. (b) Regional map of the NW Ross Sea (NWRS) showing the extent of Late Cenozoic volcanism above and below sea level. Faults and volcanic seamounts in the Adare Basin were mapped by Granot *et al.* (2010) using a combination of seismic and multibeam bathymetry data. The locations of the basalts examined in this study (solid color symbols) and from other studies (open symbols) are shown with symbol shapes corresponding to their major element compositional name as defined in Fig. 3. Volcanic deposits along the northern coastline of Victoria Land and islands are part of the Hallett volcanic province (Kyle, 1990). Here we defined NWRS basalts as those that are included in the Hallett volcanic province, the Malta Plateau of the Melbourne volcanic province (Kyle, 1990), as well as seamounts located on the continental shelf and within the Adare Basin. The bold dashed line delimits the approximate boundary between the East Antarctic craton and the West Antarctic rift. The bold dotted line at 1500 mbsl delimits the approximate boundary between rifted continental lithosphere and oceanic lithosphere. AP, Adare Peninsula; PI, Possession Islands; HP, Hallett Peninsula; DP, Daniel Peninsula; CI, Coulman Island; MP, Malta Plateau.

oceanic) and sub-lithospheric sources for alkaline magmatism, as well as the potential overprint of these domains by subduction-related processes.

TECTONIC AND MAGMATIC HISTORY

The pre-Cenozoic fabric of Northern Victoria Land (NVL), which includes the continental portion of the NWRS (Fig. 1b), is expressed by three fault-bounded lithotectonic blocks (Wilson, Bowers and Robertson Bay terranes) that were amalgamated via subduction during the Ross orogeny in late Neoproterozoic to late

Ordovician times (Borg & Stump, 1987; Boger & Miller, 2004; Di Vincenzo *et al.*, 2016). Devonian and Carboniferous calc-alkaline intrusions in NVL (Admiralty suite, 370–350 Ma; Stump, 1995) indicate younger subduction-related magmatism. All of this was part of the more extensive Terra Australis orogen that is characterized by convergent deformation along the entire 18 000 km pre-dispersal length of the Pan-Pacific margin of the Gondwana supercontinent from the Neoproterozoic to the end of the Paleozoic (Cawood, 2005). The Terra Australis orogen terminated with the assembly of Pangaea and heralded the beginning of the

late Carboniferous to Triassic Gondwanide orogeny (Cawood, 2005), which is manifested in NVL by deformed siliciclastic strata (Vaughan & Pankhurst, 2008). Following a period of erosion that produced the Kukri peneplain (Isbell, 1999), early to middle Jurassic rifting and magmatism marked the initial stages of Gondwana break-up and the separation of Africa and South America from the Dronning Maud Land margin of Antarctica. Flood basalts and intrusions of the Ferrar large igneous province were emplaced in a narrow linear band over a distance of 3500 km within a very short time interval at ~ 183 Ma (Elliot & Fleming, 2004; Burgess *et al.*, 2015; Ivanov *et al.*, 2017). The origin of Ferrar magmatism remains controversial; some researchers relate it to mantle plume activity and long-distance transport of magma within the crust (Storey & Kyle, 1997; Elliot *et al.*, 1999; Vaughan & Storey, 2007) whereas others call for mantle melting fluxed by slab fluids from subduction along the length of the Gondwana margin (Hergt *et al.*, 1991; Ivanov *et al.*, 2017).

The subduction of the Phoenix oceanic plate beneath the eastern margin of Gondwana ceased, abruptly, in the Cretaceous (Bradshaw, 1989; Mukasa & Dalziel, 2000; Tulloch *et al.*, 2009) and the extension that formed the present-day WARS began. The sudden change from a mostly compressional tectonic regime to a tensional one has been explained by the oblique subduction of the Pacific–Phoenix spreading center (Bradshaw, 1989), possibly with the aid of a mantle plume that weakened the lithosphere and controlled the location of rifting between Zealandia and the Marie Byrd Land margin of Antarctica (Weaver *et al.*, 1994). The shutting down of subduction has also been explained by the mechanism of slab capture (Luyendyk, 1995) and also by a collision with a young and thermally buoyant Hikurangi oceanic plateau (Davey *et al.*, 2008). Whatever the cause, rifting led to the final disintegration of Gondwana and the isolation of Antarctica by 83 Ma (magnetic isochron C34; Veevers, 2012, and references therein). It has been estimated that this early rifting phase resulted in 500–1000 km of crustal extension across the entire Ross Sea between Marie Byrd Land and the western boundary of the East Antarctica craton (DiVenere *et al.*, 1994; Luyendyk *et al.*, 1996). During the Late Cretaceous and early Cenozoic, north–south-oriented basins, including the Northern Basin (Fig. 1b) and Victoria Land Basin, and ridges (e.g. Coulman High) were formed (Cooper *et al.*, 1987).

The early phase of broadly distributed extension in the WARS transformed into a more focused phase of extension in the Paleogene (Huerta & Harry, 2007, and references therein). This phase of rifting in the western Ross Sea led to ~ 300 km of extension between East and West Antarctica between 80 and 40 Ma (Molnar *et al.*, 1975; Cande *et al.*, 2000), and was accompanied by rapid exhumation and uplift of the adjacent Transantarctic Mountains (Fitzgerald *et al.*, 1986) and the oldest known igneous activity associated with the

WARS. The Meander Intrusive Group consists of Eocene–Oligocene (48–23 Ma) plutonic and subvolcanic alkaline rocks found in NVL (Müller *et al.*, 1991; Tonarini *et al.*, 1997). Rocchi *et al.* (2002, 2005) and Nardini *et al.* (2009) proposed a multi-stage model for the origin of these rocks that calls upon upper mantle enrichment by small-degree melts during Late Cretaceous rifting (amagmatic phase). This was followed more than 30 Myr later by melting of this enriched mantle by a combination of warm asthenosphere flow beneath the rift towards the East Antarctic craton and localized decompression in response to the reactivation of NW–SE trans-lithospheric faults by far-field plate-tectonic stresses (Rocchi *et al.*, 2002).

By the middle Cenozoic WARS extension was focused in the Victoria Land Basin, which lies along the central and southern margin of the western Ross Sea, and the Adare Basin located in the north western Ross Sea (NWRS; Fig. 1b). The Adare Basin represents a fossil spreading center, the slowest arm (ultraslow; $\sim 12 \text{ mm a}^{-1}$ full-spreading rate) of a three-ridge junction between the Australia, East Antarctic and West Antarctic plates, that was active from 43 to 26 Ma (chrons C20–C8) and resulted in ~ 140 – 170 km of ENE–WSW plate separation (Cande *et al.*, 2000; Cande & Stock, 2006; Granot *et al.*, 2013). Post-spreading events were minor and occurred at ~ 24 Ma and ~ 17 Ma, resulting in an additional 7 km of extension and the creation of the Adare Trough by normal faulting (Granot *et al.*, 2010, 2013). These faults display an en echelon NW–SE structural trend (Fig. 1b). A strong kinematic relationship between sea floor spreading and the WARS is supported by magnetic, seismic and structural trends that show continuity across the shelf break into the Northern Basin (Cande & Stock, 2006; Davey *et al.*, 2006; Damaske *et al.*, 2007; Ferraccioli *et al.*, 2009; Selvans *et al.*, 2012). This indicates a continuity in crustal type that is most probably oceanic (Selvans *et al.*, 2012, 2014; Granot *et al.*, 2013). Granot *et al.* (2013) suggested that the shallow bathymetry of the Northern Basin (Fig. 1b) may be accommodated by thick deposits of glacio-marine sediments on top of oceanic crust that have filled the basin.

Neogene alkaline volcanism along the northern coastline of Victoria Land and offshore islands comprises the Hallett volcanic province, which consists of roughly north–south elongated shield volcanoes that range in age from ~ 14 Ma to ~ 2 Ma (Kyle, 1990; Müller *et al.*, 1991; Armienti *et al.*, 2003; Nardini *et al.*, 2003; Mortimer *et al.*, 2007; Smellie *et al.*, 2011). Volcanism on the adjacent continental shelf and Adare Basin was first identified through ocean bottom bathymetry (Panter & Castillo, 2007) and consists of hundreds of relatively small volcanic centers distributed over an area of $\sim 35\,000 \text{ km}^2$. The trend of volcanism overlaps with the roughly north–south pattern of normal faulting, particularly the major bounding faults of the Adare Trough, and is generally aligned with volcanism on land in the Hallett volcanic province (Fig. 1b). The age of

seamount volcanism was first constrained by seismic stratigraphic relationships. Granot *et al.* (2010) noted that all of the volcanic features are exposed above the seafloor surface, penetrating nearly the entire stratigraphic sequence (to the late Pliocene) and that buried intrusions, which might indicate an older period of magmatism, are not observed along the ~3200 km length of the multi-channel seismic data collected in the Adare Basin. The spatial distribution, relative age and preliminary petrological data all indicate that the volcanic activity in the oceanic Adare Basin is an extension of WARS volcanism. Based on this it was proposed that both the continental and oceanic portions of the WARS in the NWRS share a common origin (Panter & Castillo, 2007, 2008; Panter *et al.*, 2016).

SAMPLE DETAILS AND METHODS

This study is based on rock samples collected from seafloor dredging, rock and powder samples acquired from personal collections and rock samples provided by the U.S. Polar Rock Repository, Byrd Polar and Climate Research Center (<http://research.bpcrc.osu.edu/rr/>). Dredge samples were collected during a 38 day, National Science Foundation funded, marine geophysical survey cruise (NBP0701) from December 2006 to January 2007 onboard the icebreaker RV/IB *Nathaniel B. Palmer*. The dredging was accomplished at a relatively high level of precision by using the *Palmer's* automatic dynamic global positioning system, depth sounding using a pinger attached to the wire at ~300 m above the dredge, and detailed seafloor bathymetry.

The primary objective of this study is to evaluate mantle sources and processes responsible for alkaline volcanism across the continental–oceanic transition in the NWRS. To accomplish this we selected 30 relatively unfractionated basalts (MgO > 6 wt %). Petrographic data along with mineral chemistry, major and trace elements, Sr–Nd–Pb–O isotopes, and ⁴⁰Ar/³⁹Ar geochronology were obtained on subsets of these samples (Table 1). The location of the samples is indicated in Fig. 1b and their whole-rock geochemistry and isotopic compositions are presented in Tables 2 and 3. Twelve of the 30 samples are from other studies (see Table 2 for details and references) and of those 12, four (MA-009a, MA-117, P74794, P74833) were analyzed in this study for mineral chemistry and oxygen isotopes on olivine separates (Table 3) and two of those (MA-009a, MA-117) were also analyzed for Sr–Nd–Pb isotopes on whole-rock powders (Table 2). An additional sample, SAX20 (Nardini *et al.*, 2009), is not from the NWRS but from a location to the south within the Melbourne volcanic province (Kyle, 1990) and is included for comparison.

Mineral chemistry

Rocks were crushed and sieved to separate phenocrysts between 250 µm and 2 mm in diameter. Six to eight

phenocrysts (olivine, clinopyroxene, amphibole and plagioclase) from each sample were mounted and singly polished on 1 cm diameter epoxy rounds. These were then secured into 1 inch brass mounts (three rounds per mount) and carbon coated for analysis by electron microprobe. Major and minor element chemistry was measured on a Cameca SX-100 Electron Microprobe Analyzer at the University of Michigan EMAL laboratory using a 15 kV accelerating voltage beam, 15 nA beam current, and 10–12 µm spot size. A total of 311 unknowns were analyzed: 174 olivine, 76 clinopyroxene, 23 amphibole, and 38 plagioclase grains. The following elemental routines were performed for each mineral: Si, Cr, Fe, Mn, Mg, Ca, P, Ni for olivine; Si, Al, Ti, Cr, Fe, Mn, Mg, Ca, Na, K, P, Ni, Cl for clinopyroxene; Mg, Al, K, Ca, Ti, Cr, Mn, Fe, Na, P, Si, Sr, Ba for plagioclase; Mg, Al, K, Ca, Ti, Cr, Mn, Fe, Na, P, Si, Cl, F for amphibole. Measurements (a total of 475 unknowns) were taken primarily within the cores of minerals (or presumed cores on fragments), and also at rim and intermediate grain locations when compositional or textural variations were observed (Krans, 2013).

Major and trace elements

Concentrations of major oxides and some of the trace elements in whole-rock powders were determined by X-ray fluorescence spectrometry (XRF) at the GeoAnalytical Laboratory of Washington State University (Castillo *et al.*, 2010) and at New Mexico Tech (Hallett & Kyle, 1993). For some samples concentrations of rare earth elements (REE) and other trace elements (Rb, Sr, Y, Ba, Pb, Th, Zr, Nb, and Hf) on whole-rocks were determined by high-resolution inductively coupled plasma mass spectrometry (ICP-MS) using a Finnigan Element 2 system at the Scripps Institution of Oceanography (SIO) Analytical Facility, following the method of Janney & Castillo (1996) with some modifications. Prior to ICP analysis, rock samples were crushed in an alumina ceramic jaw crusher. The resultant rock chips were ultrasonically washed in deionized water for 30 min, dried in an oven overnight at ~110°C, and then fresh-looking pieces were hand-picked under a binocular microscope. The selected chips were powdered in an alumina ceramic grinder. For each sample, about 25 mg of powder was digested with an ultrapure 2:1 concentrated HF–HNO₃ solution in a Teflon beaker, and the mixture was placed on a hot plate (~60°C) and dried under a heat lamp. About 2 ml of ultrapure 12N HNO₃ was twice added to the digested sample and evaporated to dryness. After drying, the digested sample was diluted 4000-fold with 2% HNO₃ solution containing 1 ppb In as an internal standard. The instrument drift was monitored and corrected by measuring an in-house rock standard as an unknown within the run. For selected samples some trace elements for whole-rocks were analyzed by instrumental neutron activation at New Mexico Tech (Hallett & Kyle, 1993).

Table 1: Summary of $^{40}\text{Ar}/^{39}\text{Ar}$ results and analytical methods

Sample	Locality	Latitude	Longitude	Rock type	Irrad. #	Material	Age analysis	Integrated age (Ma)	2σ	n	isochron age (Ma)	2σ	n	MSWD	$^{40}\text{Ar}/^{36}\text{Ar}$	2σ	Plateau age (Ma)	2σ	n	MSWD	^{36}Ar (%)	$^{36}\text{Ar}/\text{K}$	K/Ca	2σ	Preferred age (Ma)	Method	
Adare seamounts																											
D2-1	trough W scarp	69.861	171.844	hawaiite	NM-217	GM conc.	furnace step-heat	15.93	0.76	10	4.56	0.27	10	1.63	296.2	2.3	4.61	0.19	10	1.52	100.0	49.4	0.11		15.93 ± 0.76	integrated	
D3-1	trough W scarp	70.000	171.990	hawaiite	NM-217	GM conc.	furnace step-heat	4.93	0.66	10	3.76	0.13	11	4.03	293.1	1.5	3.35	0.11	4	0.37	59.9	137.9	0.53	0.28	4.61 ± 0.19	plateau	
D4-1	trough center	70.070	172.316	basanite	NM-251	GM conc.	laser step-heat	3.44	0.08	11	2.51	0.09	8	7.94	311.0	16.0	2.61	0.02	5	1.65	50.3	67.1	1.2	0.3	3.35 ± 0.11	plateau	
D4-3	trough center	70.070	172.316	basanite	NM-251	GM conc.	laser step-heat	2.45	0.02	11	2.51	0.09	8	7.94	311.0	16.0	2.61	0.02	5	1.65	50.3	67.1	1.2	0.3	2.51 ± 1.09	isochron	
D7-1	continental shelf	71.820	171.900	basanite	NM-217	GM conc.	furnace step-heat	0.47	0.73	10	0.29	0.15	10	6.14	295.9	3.5	0.32	0.23	7	6.95	91.7	95.7	0.35	0.36	0.32 ± 1.09	plateau	
D9-1	S basin	71.628	172.523	tephrite	NM-217	GM conc.	furnace step-heat	2.91	0.30	10	2.89	0.16	10	15.82	293.1	6.8	2.86	0.14	10	14.68	100.0	167.92	0.925	1.15	2.86 ± 0.76	plateau	
D12-1	S basin	71.631	172.634	basanite	NM-217	GM conc.	furnace step-heat	3.52	0.50	10	2.87	0.07	9	8.05	298.0	10	2.89	0.06	9	6.27	99.8	149.5	0.35	0.39	2.89 ± 0.06	plateau	
D15-1	S basin	71.579	172.733	tephrite	NM-217	GM conc.	furnace step-heat	3.12	0.22	9	2.82	0.04	2	8.82	298.0	10	2.82	0.04	2	8.82	55.3	187.5	0.30	0.47	3.12 ± 0.22	integrated	
D16-1	S basin	71.597	172.821	tephrite	NM-217	GM conc.	furnace step-heat	2.97	0.56	11	2.66	0.19	11	1.25	296.9	1.9	2.76	0.13	9	1.44	99.2	158.2	0.27	0.31	2.76 ± 0.13	plateau	
D17-1	S basin	71.499	173.486	trachyte	NM-217	GM conc.	furnace step-heat	0.20	0.07	10	0.14	0.01	9	1.81	295.2	4.0	0.14	0.02	9	1.58	99.9	286.2	11.8	14.9	0.14 ± 8.02	plateau	
Possession Islands																											
A227B	McCormick Is.	71.842	170.976	hawaiite	NM-251	GM conc.	laser step-heat	0.168	0.031	11	0.058	0.029	8	2.05	295.5	1.6	0.053	0.031	8	2.54	95.6	163.2	0.30	0.34	0.053 ± 3.031	plateau	
HC-SPI-4 (3873)*	Possession	71.885	171.167	tephrite	NM-251	GM conc.	laser step-heat	0.10	0.04	11	0.17	0.02	11	6.98	294.3	2.1	0.16	0.02	5	0.54	77.6	107.5	0.30	0.31	0.16 ± 7.02	plateau	
NV-3C (5166)*	Possession	71.885	171.167	benmorite	NM-251	GM conc.	laser step-heat	1.40	0.03	10	1.41	0.01	8	0.64	298.2	6.0	1.42	0.0	8	0.19	85.6	293.4	2.3	2.1	1.42 ± 3.01	plateau	
NV-4C (5171)*	Foyn	71.950	171.083	hawaiite	NM-251	GM conc.	laser step-heat	0.25	0.14	11	0.49	0.32	10	2.12	294.6	3.9	0.33	0.1	8	0.71	98.3	102.6	0.21	0.22	0.33 ± 2.10	plateau	
A225A	Foyn	71.957	171.093	basanite	NM-251	GM conc.	laser step-heat	0.26	0.03	11	0.076	0.042	10	3.00	301.3	2.4	0.24	0.03	3	0.85	66.5	82.8	0.16	0.30	0.24 ± 0.03	plateau	

*Sample provided by the Polar Rock Repository—PRR-# (<http://research.bpcrc.osu.edu/rr/>). MSWD, mean square weighted deviation. Integrated age calculated by summing isotopic measurements of all steps. Plateau age is inverse-variance-weighted mean of selected steps. Plateau age error is inverse-variance-weighted mean error (Taylor, 1982) times root MSWD and where MSWD > 1. Decay constants and isotopic abundances after Steiger & Jäger (1977). Electron multiplier sensitivity for MAP 215-50 averaged $8.54e^{-17}$ moles pA^{-1} for furnace analyses and $4.37e^{-17}$ for laser analyses. Laser analyses sensitivity on Argus VI averaged $9.84e^{-17}$ moles pA^{-1} . MAP 215-50 total system blank and background for groundmass concentrate analyses averaged 5850, 7.10, 5.21, 22.4, 20.4×10^{-18} moles at masses 40, 39, 38, 37 and 36, respectively. Argus VI total system blank and background for K-feldspar analyses averaged 409, 2.52, 1.10, 2.49, 7.75×10^{-18} moles at masses 40, 39, 38, 37 and 36, respectively. Argus VI total system blank and background for groundmass concentrate analyses averaged 358, 2.8, 0.19, 0.50, 1.3 $\times 10^{-18}$ moles on masses 40, 39, 38, 37 and 36, respectively. J-factors determined by CO_2 laser-fusion of six single crystals from each of 10 radial positions around the irradiation tray. Correction factors for interfering nuclear reactions were determined using K-glass and CaF_2 and are as follows: ($^{40}\text{Ar}/^{39}\text{Ar}$) $_{\text{K}} = 0.0000 \pm 0.0004$; ($^{36}\text{Ar}/^{37}\text{Ar}$) $_{\text{Ca}} = 0.00028 \pm 0.00001$; ($^{39}\text{Ar}/^{37}\text{Ar}$) $_{\text{Ca}} = 0.00068 \pm 0.00005$.

Table 2: Geochemical and radiogenic isotope (Sr, Nd, Pb) analyses of NWRS basalts

Sample no.:	SAX20	MA009a	MA-117	MP24	A223	MP8	HC-DP-3 3839	MP34	MP32	P74794	P74833	A210B
Dec. latitude S:	-73.770	-73.040	-73.020	-73.063	-72.872	-72.830	-72.667	-73.490	-73.490	-71.668	-71.653	-72.023
Dec. longitude E:	165.950	167.470	167.630	167.750	168.970	169.098	169.633	169.580	169.580	170.080	170.120	170.160
Geographical location:	Greene Point, MVP	Malta Plateau	Malta Plateau	Malta Plateau	W of Daniell Peninsula	W of Daniell Peninsula	Daniell Peninsula	Coulman Island	Coulman Island	Robertson Bay	Robertson Bay	SW of Cape Roget
Rock name (TAS):	TEPH	AKB	AKB	BAS	AKB	AKB	AKB	BAS	BAS	AKB	AKB	AKB
<i>Major elements (wt %)</i>												
SiO ₂	41.61	49.89	47.48	43.79	46.31	44.68	45.16	43.20	44.32	47.71	48.95	45.65
TiO ₂	3.69	2.45	2.66	2.83	2.24	2.74	3.19	3.11	3.42	2.49	2.10	2.35
Al ₂ O ₃	12.05	13.60	14.38	14.02	14.48	15.06	14.12	14.92	15.87	13.88	16.15	13.42
FeO _i	14.79	11.15	11.58	10.47	11.86	12.91	11.68	11.78	12.06	11.32	10.17	10.60
MnO	0.29	0.16	0.19	0.18	0.19	0.20	0.19	0.19	0.20	0.17	0.16	0.19
MgO	9.52	9.35	8.49	12.64	9.49	9.63	9.11	11.24	8.44	9.41	8.04	13.08
CaO	9.42	9.96	10.98	11.15	11.22	11.03	12.94	11.09	10.52	11.26	10.23	9.83
Na ₂ O	5.42	2.23	2.66	3.02	2.75	2.55	2.25	2.83	3.36	2.45	2.83	3.16
K ₂ O	1.57	0.89	1.16	1.32	0.95	0.80	0.85	1.04	1.12	0.94	1.00	1.17
P ₂ O ₅	1.63	0.32	0.43	0.57	0.50	0.39	0.52	0.61	0.68	0.38	0.37	0.55
LOI	0.90	0.82	0.44	0.84		0.73	2.44	0.58	0.60	0.54	-0.48	
Total	100.00	100.82	100.45	100.00	99.99	100.00	100.01	100.00	100.00	100.55	100.00	100.00
Mg#	53.4	59.9	56.7	68.3	58.8	57.1	58.2	63.0	55.5	59.7	58.5	68.8
<i>CIPW norm minerals (wt %)</i>												
Ne	23.7		2.4	12.5	5.0	5.5	5.0	10.3	9.2	1.1		8.6
Lc												
Di	26.5	18.7	22.8	24.9	23.0	20.5	28.6	21.2	18.8	24.0	16.3	21.2
Hy		17.7									1.5	
Ol	23.7	9.6	19.9	24.8	22.5	24.5	18.4	25.1	21.0	21.0	19.0	27.7
<i>Trace elements (ppm)</i>												
Sc	17.4	17			32	33	35	32.8	26.3		21	25
V	130	254	302				317			259	180	
Cr	369	272	349		7	465	389	713	382	477	304	479
Ni		86	93				116			150	99	
Cu		22	42				81			69	28	
Zn		108	108				83			88	74	
Ga							17			20	21	
Rb	72	21	30	38	39	20	21	24	32	20.5	22.9	26
Sr	1494	461	531	640	608	552	657	667	867	477	585	592
Y	49	24	33	23	40.9	24	26.8	25	30	23.9	21.8	26.4
Zr	500	172	200	194	225	158	217	204	236	167	160	397
Nb	183.2	28	52	70.6	42.4	40.3	57.6	67.5	85.3	41.3	40.1	67.7
Cs					0.31					0.15	0.12	0.54
Ba	830	229	337	431	256	251	273	329	399	236	252	418
La	125.1	24.36	32.71	40.5	32.77	29.3	39.2	39.8	51.8	29.8	29	43.60
Ce		50.9	66.81	86	69.05	65	78.0	81	109	61.1	58.3	82.99
Pr	28	6.39	8	10.2	9.32	8		10	13	7.54	7.01	10.90
Nd	104.3	25.92	32.01	39	36.09	33	40.0	40.3	51.2	30.3	27.8	39.98
Sm	18.9	5.47	7.08	7.3	7.59	6.9		7.7	9.9	6.6	5.81	7.54
Eu	5.7	1.77	2.13	2.5	2.46	2.4		2.6	3.2	2.23	1.95	2.39
Gd	17.7	5.09	6.76	7.7		7.3		8.3	10	6.16	5.36	
Tb	2.24	0.82	1	1.01	1.16	1.01		1.06	1.25	0.94	0.82	1.10
Dy	11.8	4.54	5.67	5.1	6.34	5.5		5.5	6.5	5.22	4.67	5.19
Ho	1.93	0.8	1.1	0.89	1.16	0.99		1.01	1.18	0.98	0.87	0.90
Er	4.96	2.07	3.06	2.25	3.38	2.58		2.58	3.12	2.43	2.22	2.64
Tm	0.61	0.29	0.4	0.29		0.35		0.33	0.39	0.32	0.29	
Yb	3.76	1.73	2.55	1.87	2.77	2.05		2.1	2.4	1.85	1.74	2.11
Lu	0.57	0.37	0.37	0.26	0.27	0.3		0.29	0.33	0.27	0.27	0.26
Hf	12.8			4.62	4.86	4.69		4.99	5.6	4.32	3.99	7.48
Ta	10.25			4.17	2.70	2.57		3.91	4.78	2.67	2.56	3.90
Pb	5			2.2	2.01	1.7	1.4	2.1	2.43	1.87	2.13	2.45
Th	16.65			5.89	5.01	3.43	5.0	5.22	6.05	3.78	4.02	5.07
U	4.93			1.63	0.91	1.02	2.6	1.46	1.82	0.96	0.92	1.68
<i>Radiogenic isotopes (measured values)</i>												
⁸⁷ Sr/ ⁸⁶ Sr	0.70284	0.705035	0.703786	0.70316	0.703424	0.703357			0.702854			0.703458
¹⁴³ Nd/ ¹⁴⁴ Nd	0.512979	0.512748	0.512824	0.512876	0.512883	0.512902						0.512891
²⁰⁶ Pb/ ²⁰⁴ Pb	19.5683	19.222	19.32	19.6465	19.703	19.6407			19.7314			19.363
²⁰⁷ Pb/ ²⁰⁴ Pb	15.5399	15.625	15.62	15.5665	15.599	15.5169			15.5955			15.615
²⁰⁸ Pb/ ²⁰⁴ Pb	38.9781	39.327	39.27	39.2801	39.387	39.2011			39.2857			39.202

(continued)

Table 2: Continued

Sample no.:	A240B-1	A232B	NV-6E	VC-21	A227B	AW82205	HC-FI-2A	NV-4	NV-4C	NV-4B	A225A	HC-SPI-2
PRR-#:												
Dec. latitude S:	-71.302	-71.703	-71.619	-71.694	-71.842	-71.950	-71.950	-71.950	-71.950	-71.955	-71.957	-71.885
Dec. longitude E:	170.210	170.298	170.556	170.557	170.976	171.083	171.083	171.083	171.083	171.092	171.093	171.167
Geographical location:	Cape Adare	Adare Peninsula	Adare Peninsula	Adare Peninsula	McCormick Island	Foyn Island	Foyn Island	Foyn Island	Foyn Island	Foyn Island	Foyn Island	Possession Island
Rock name (TAS):	BAS	HAW	BAS	BAS	HAW	AKB	AKB	AKB	HAW	AKB	BAS	BAS
<i>Major elements (wt %)</i>												
SiO ₂	42.53	46.87	42.72	44.94	46.92	45.57	45.46	45.73	45.64	45.06	45.46	41.48
TiO ₂	3.80	2.87	3.86	3.24	2.83	2.96	3.01	2.97	3.13	2.80	3.15	3.53
Al ₂ O ₃	14.54	15.43	13.67	14.56	15.73	14.74	14.58	14.55	15.39	13.42	15.50	13.08
FeO _t	12.66	11.54	13.05	12.86	10.59	11.43	11.71	11.39	11.32	11.73	11.22	12.20
MnO	0.21	0.21	0.17	0.18	0.21	0.19	0.19	0.19	0.19	0.19	0.20	0.22
MgO	8.72	7.14	10.02	7.07	7.36	9.23	9.33	9.45	7.84	11.23	7.74	9.56
CaO	11.95	9.84	10.98	11.14	9.92	10.71	10.62	10.65	10.55	10.89	10.58	12.79
Na ₂ O	3.47	3.75	3.84	3.76	4.30	3.50	3.45	3.55	3.95	3.13	4.06	4.59
K ₂ O	1.42	1.61	0.94	1.54	1.54	1.06	1.05	0.93	1.31	0.99	1.37	1.41
P ₂ O ₅	0.69	0.73	0.74	0.70	0.60	0.61	0.61	0.60	0.67	0.57	0.71	1.15
LOI	0.82						0.38	2.70	0.49		0.56	0.70
Total	99.99	99.99	100.00	100.00	100.00	100.00	100.01	100.01	99.99	100.00	99.99	100.01
Mg#	55.1	52.5	57.8	49.5	55.3	59.0	58.7	59.7	55.3	63.1	55.2	58.3
<i>CIPW norm minerals (wt %)</i>												
Ne	15.9	8.0	15.0	12.7	11.4	9.1	8.9	8.7	11.3	9.0	12.3	21.0
Lc												6.5
Di	28.6	19.4	26.5	26.9	21.6	22.7	22.5	22.8	22.7	25.0	22.9	31.9
Hy												
Ol	18.3	18.4	21.8	16.9	16.8	20.7	21.3	21.0	17.8	24.1	17.4	18.4
<i>Trace elements (ppm)</i>												
Sc	30	25			22	25	25	25	24		23	27
V	312	235	235	240		278	251	250	253	209	263	255
Cr	305	260	225	218	230	431	367	388	269	395	238	332
Ni	115	99	435	373		177	174	173	119	411	117	156
Cu	72	57	226	206		60	55	55	54	101	58	65
Zn	95	100	75	80		91	97	92	96	78	94	109
Ga	21	21				21	19	19	21		21	20
Rb	32	32	21	75	37	26	24	17	33	16	36	44
Sr	800	787	800	695	812	684	672	642	761	592	831	1034
Y	35.0	35.0	30	30		30.0	27.5	26.2	29.0	27	33.0	33.7
Zr	263	276	225	311		223	224	227	269	203	280	331
Nb	83.0	70.0	58	68		71.0	64.1	62.1	77.8	53	82.0	107.6
Cs	0.40	0.69			0.47	0.29					0.33	
Ba	422	616	323	419	527	319	311	300	379	269	396	564
La	52.50	51.80	43	49	64.00	42.20	43.2	37.9	50.3	39	54.20	73.9
Ce	103.60	105.20	78	84	125.20	85.00	84.6	80.2	101.4	70	107.80	138.9
Pr			10.3	10.6						8.8		
Nd	50.00	45.90	44	44	51.10	40.50	40.1	40.8	45.4	36	46.40	61.3
Sm	9.95	9.66	9.7	9.1	9.97	8.18				7.6	9.18	
Eu	3.04	3.44	2.9	2.8	3.11	2.58				2.3	2.82	
Gd			9	9						7		
Tb	1.21	1.13	1.2	1.2	1.16	1.01				1	1.08	
Dy			5.9	5.7						5.1		
Ho			1	1						0.8		
Er			2.6	2.5						2.3		
Tm												
Yb	2.32	2.33	2.4	2.4	2.63	2.05				2.1	2.19	
Lu	0.33	0.30	0.3	0.4	0.35	0.26				0.3	0.34	
Hf	6.73	6.44	5.6	5.3	7.64	5.41				4.6	6.47	
Ta	5.25	4.24	4.4	5.1	6.03	4.51				3.8	5.19	
Pb	2.00	5.00	1.7	1.9	4.30	2.00	0.9	1.1	3.1	1	2.00	2.9
Th	6.11	5.53	4.6	6.4	7.77	4.37	5.3	5.5	6.6	4.6	6.64	9.1
U	1.70	2.00	1	2.3	2.11	0.90	1.2	0.6	2.2	0.9	2.04	2.6
<i>Radiogenic isotopes (measured values)</i>												
⁸⁷ Sr/ ⁸⁶ Sr	0.702944	0.703741			0.702900	0.702900	0.702780				0.702970	0.702870
¹⁴³ Nd/ ¹⁴⁴ Nd	0.512930	0.512874			0.512937	0.512945	0.513000				0.512935	0.513000
²⁰⁶ Pb/ ²⁰⁴ Pb	20.026	19.432			20.180	20.184					20.044	
²⁰⁷ Pb/ ²⁰⁴ Pb	15.633	15.642			15.680	15.653					15.587	
²⁰⁸ Pb/ ²⁰⁴ Pb	39.504	39.285			39.794	39.703					39.438	

(continued)

Table 2: Continued

Sample no.:	AW82214	NV-3B	D2-1	D4-1	D4-3	D9-1	D12-1
PRR-#:							
Dec. latitude S:	-71.900	-71.900	-69.861	-70.070	-70.070	-71.628	-71.631
Dec. longitude E:	171.167	171.200	171.844	172.316	172.316	172.523	172.634
Geographical location:	Possession Island	Possession Island	Adare Trough, W scarp	Adare Trough, center	Adare Trough, center	S Adare Basin	S Adare Basin
Rock name (TAS):	BAS	BAS	HAW	BAS	BAS	TEPH	BAS
<i>Major elements (wt %)</i>							
SiO ₂	41.64	44.78	46.75	43.07	41.98	45.26	44.60
TiO ₂	3.47	3.60	2.63	2.99	4.75	3.18	3.06
Al ₂ O ₃	13.07	15.82	17.18	12.92	13.59	15.18	13.34
FeO _t	12.23	12.93	7.85	10.20	13.35	11.48	11.47
MnO	0.22	0.22	0.15	0.20	0.27	0.26	0.21
MgO	9.78	6.45	8.83	13.32	9.86	6.39	10.70
CaO	12.60	10.37	10.43	10.84	10.41	9.42	10.02
Na ₂ O	4.29	3.65	3.43	3.64	3.15	5.58	4.12
K ₂ O	1.52	1.21	1.73	1.88	1.74	2.16	1.54
P ₂ O ₅	1.17	0.96	1.01	0.94	0.90	1.09	0.93
LOI			3.68	1.79	1.22	1.73	1.17
Total	99.99	100.00	99.99	100.00	100.00	100.00	99.99
Mg#	58.8	47.1	66.7	70.0	56.8	49.8	62.5
<i>CIPW norm minerals (wt %)</i>							
Ne	19.7	8.5	7.4	16.7	13.0	21.1	14.8
Lc	7.0			4.4			
Di	32.1	18.3	15.2	27.6	22.9	24.5	24.7
Hy							
Ol	18.8	18.6	18.1	24.6	22.3	14.8	22.6
<i>Trace elements (ppm)</i>							
Sc	27		25	27	30	16	22
V	296	215	197	233	325	185	214
Cr	375	35	277	540	244	135	355
Ni	167	296	162	338	139	71	205
Cu	30	101	40	46	42	25	46
Zn	101	87	71	81	115	136	102
Ga	21		17	16	23	21	19
Rb	47	20	34	31	37	40	35
Sr	1034	925	901	861	1131	1216	1007
Y	38.0	28	35.0	26.5	35.5	33.7	30.3
Zr	332	217	256	292	394	553	347
Nb	118.0	61	75.1	93.6	96.2	155.0	89.4
Cs	0.54						
Ba	626	371	604	467	595	558	401
La	73.80	47	59.06	51.01	70.8	88.58	56.48
Ce	142.60	83	105.27	95.53	152.4	167.12	111.97
Pr		10.7	12.80	10.29		17.06	12.05
Nd	61.50	46	46.44	40.58	69.4	63.93	48.43
Sm	12.01	9.6	8.45	7.23		10.77	9.11
Eu	3.68	3.1	2.80	2.45		3.35	2.90
Gd		9		14.75		24.44	18.03
Tb	1.39	1.2	1.09	1.11		1.45	1.30
Dy		5.6	6.10	4.90		6.38	5.74
Ho		0.9	1.09	0.90		1.14	1.03
Er		2.4	3.05	1.91		2.50	2.14
Tm			0.42	0.31		0.41	0.34
Yb	2.37	2.2	2.87	1.72		2.35	1.94
Lu	0.31	0.3	0.39	0.28		0.34	0.28
Hf	7.57	5.2					
Ta	6.89	4.7					
Pb	2.00	1.6	2.83	2.52	13.0	3.44	2.01
Th	8.33	5.5	7.26	5.33	9.0	6.77	4.81
U	2.80	1	1.75	1.41	4.7	2.20	1.33
<i>Radiogenic isotopes (measured values)</i>							
⁸⁷ Sr/ ⁸⁶ Sr	0.702884	0.70343		0.702870		0.702900	0.702779
¹⁴³ Nd/ ¹⁴⁴ Nd	0.512945	0.51282		0.513000		0.512960	0.513001
²⁰⁶ Pb/ ²⁰⁴ Pb	19.851	20.028		19.237		20.234	20.111
²⁰⁷ Pb/ ²⁰⁴ Pb	15.620	15.658		15.583		15.653	15.625
²⁰⁸ Pb/ ²⁰⁴ Pb	39.354	39.916		38.812		39.715	39.551

Sample numbers in bold are from this study. PRR, samples on loan from the Polar Rock Repository (<http://research.bpcrc.osu.edu/rr/>). Rock name based on total alkali vs silica diagram (TAS) shown in Fig. 2. FeO_t is total iron expressed as FeO, normalized to 100%. LOI, loss on ignition. Mg# = 100Mg/(Mg + Fe²⁺). Major elements (wt %) by XRF and trace elements (ppm) by XRF and ICP-MS. CIPW normative (wt %) calculated following Irving & Baragar (1971). Samples SAX20, MP24, MP8, MP34, MP32 are from Nardini *et al.* (2009). Samples MA009a and MA-117 are from Rocholl *et al.* (1995) with Sr, Nd and Pb isotopes from this study italicized. Samples P74794 and P74833 are from Mortimer *et al.* (2007). Samples NV-6E, NV-21, NV-4B and NV-3B from Aviado *et al.* (2015). Samples A223, A210B, A240B-1, A232B, A227B and A225A were collected and described by Hamilton (1972) and re-analyzed in this study.

Table 3: Oxygen isotope data from olivine phenocrysts

Sample ¹	Location	Fo ²	SIMS $\delta^{18}\text{O}$ (‰)	2SD	SEM	n_a	Core* $\delta^{18}\text{O}$ (‰)	2SD	SEM	n_a	LF $\delta^{18}\text{O}$ (‰)	2SD	MgO (wr) (wt %)
HC-DP-3 (3839)	Daniel Pen.	84 ± 2	4.89	0.22	0.03	5							9.11
HC-FI-2A (3842)	Foyn Is.	81 ± 5	5.06	0.23	0.08	7					4.88	0.20	9.33
HC-SPI-2 (3872)	Possession Is.	75 ± 9	5.23	0.28	0.07	7					4.90	0.12	9.56
HC-DP-1 (3873)	Daniel Pen.	81 ± 5	5.27	0.24	0.07	6					4.90		4.51
NV-4 (5169)	Foyn Is.	83 ± 2	4.82	0.18	0.07	7	4.87	0.27	0.06	7	4.86	0.22	9.45
NV-4C (5171)	Foyn Is.	82 ± 5	4.71	0.22	0.06	7	4.62	0.21	0.05	6			7.84
A214B	W of Daniel P.	76 ± 7	5.10	0.16	0.05	4							4.10
A223	W of Daniel P.	87 ± 3	5.25	0.23	0.12	5					5.03		9.49
A225A	Foyn Is.	81 ± 3	5.15	0.24	0.08	8	5.56	0.15	0.03	6			7.74
A227B	McCormick Is.	82 ± 5	5.08	0.23	0.04	9							7.36
A232B	Adare Pen.	81 ± 4	5.30	0.20	0.08	6					5.06		7.14
A240B-1	Cape Adare	82 ± 5	5.20	0.21	0.07	6							8.72
D12-1	S Adare Basin	84 ± 2	5.35	0.39	0.07	9							10.70
D2-1	Adare Trough	87 ± 1	5.25	0.41	0.05	4							8.83
D4-1	Adare Trough	90 ± 1	5.04	0.13	0.10	5					5.25		13.32
D4-3	Adare Trough	79 ± 1	5.43	0.23	0.11	4	5.50	0.26	0.05	7	5.17	0.14	9.86
D9-1	S Adare Basin	79 ± 1	5.05	0.39	0.10	5							6.39
MA-009a	Malta Plateau	78 ± 7	5.44	0.21	0.08	8	5.73	0.26	0.06	6			9.35
MA-117	Malta Plateau	79 ± 7	5.39	0.23	0.11	7	5.78	0.18	0.04	6	5.26	0.12	8.49
P74794	Robertson Bay	80 ± 7	5.33	0.41	0.03	6							9.41
P74833	Robertson Bay	70 ± 7	5.15	0.24	0.11	7	5.40	0.13	0.03	6			8.04

¹Numbers in parenthesis are PPR-# of samples on loan from Polar Rock Repository (<http://research.bpcrc.osu.edu/rr/>).

²Fo (%) = 100Mg/(Mg + Fe²⁺) with ± 1σ.

SIMS data are averages of multiple spot analyses (n_a) on 2–3 grains. Precision to 2 standard deviations (2SD) on standard San Carlos olivine is ±0.28‰. Core* is the average calculated for multiple SIMS spot analyses (n_a) within the core of a single olivine grain. Laser fluorination (LF) data are based on 4–5 olivine grains. Standard deviation precision (2SD) based on repeat analysis. Precision on standard UWG-2 (Core Mountain Garnet) is ±0.10‰ (2σ). SEM, standard error of mean. (wr), whole-rock MgO content (wt %).

Radiogenic isotopes (Sr, Nd, Pb)

Radiogenic isotopes were analyzed at the Scripps Institution of Oceanography (SIO) and the Woods Hole Oceanographic Institution (WHOI). At SIO whole-rock powders were dissolved following the dissolution procedure described above for the ICP-MS analyses. Lead was first separated from the dissolved samples using small ion exchange columns in an HBr medium. Residues from Pb extraction were collected and then passed through ion-exchange columns using HCl as eluent to collect Sr and REE. Finally, Nd was separated by passing the REE cuts through small ion exchange columns using alpha hydroxyisobutyric acid as eluent. The Pb, Sr and Nd isotopes were measured by thermal ionization mass spectrometry (TIMS) using a nine-collector, Micromass Sector 54 system at SIO. Lead isotopes were fractionation corrected using the isotope values of NBS 981 relative to those of [Todt et al. \(1996\)](#). Strontium isotopes were fractionation corrected to $^{86}\text{Sr}/^{88}\text{Sr} = 0.1194$ and are reported relative to NBS 987 $^{87}\text{Sr}/^{86}\text{Sr} = 0.70258$. Neodymium isotopes were measured in oxide forms, fractionation corrected to $^{146}\text{Nd}/^{144}\text{Nd} = 0.72225$ ($^{146}\text{Nd}/^{144}\text{Nd} = 0.7219$) and are reported relative to $^{143}\text{Nd}/^{144}\text{Nd} = 0.511850$ for the La Jolla Nd standard. Analytical uncertainties based on repeated measurements of standards are ±0.010 for $^{206}\text{Pb}/^{204}\text{Pb}$ and $^{207}\text{Pb}/^{204}\text{Pb}$, ±0.024 for $^{208}\text{Pb}/^{204}\text{Pb}$, ±0.000018 for $^{87}\text{Sr}/^{86}\text{Sr}$, and ±0.000014 for $^{143}\text{Nd}/^{144}\text{Nd}$. Routine analytical blanks are generally <35 pg for Sr, <10 pg for Nd and <60 pg for Pb. At WHOI Sr and Nd

chemistry for whole-rock powders was determined with Sr-Spec and Ln-Spec resin, respectively. Lead was separated following the HBr–HNO₃ procedure of [Abouchami et al. \(1999\)](#) using a single column pass. Sr, Nd and Pb analyses were carried out on the NEPTUNE multi-collector ICP-MS system. For Sr and Nd, the internal precision is 10–20 ppm (2σ); external precision, after adjusting to 0.710240 and 0.511847 for the SRM987 and La Jolla Nd standards respectively, is estimated to be 15–25 ppm (2σ). Pb analyses carry internal precisions on 206, 207, 208/204 ratios of 15–50 ppm; SRM997 Tl was used as an internal standard, and external reproducibility (including full chemistry) ranges from 20 ppm (2σ) for $^{207}\text{Pb}/^{206}\text{Pb}$, to 120 ppm (2σ) for $^{208}\text{Pb}/^{204}\text{Pb}$.

Oxygen isotopes

Oxygen isotopes on olivine separates were analyzed by traditional laser fluorination/gas source mass spectrometry (LF) and also *in situ* by secondary ionization mass spectrometry (SIMS) at the University of Wisconsin–Madison (WiscSIMS) Laboratory ([Table 3](#)). In both cases, the composition of olivine was first determined by electron microprobe analysis (EMPA), specifically the forsterite content, which was needed to produce a calibration curve to correct for SIMS bias in measured oxygen values relative to SCOL (see [Valley & Kita, 2009](#)). Olivines chosen for analysis by SIMS contain varying percentages of melt and oxide inclusions, which unlike LF, are easily avoided by the SIMS

technique ($\sim 10\ \mu\text{m}$ diameter spot size). Furthermore, the small number of olivine grains separated owing to the limited amount of material for some of the samples required the use of single crystal SIMS analysis.

For LF, olivine was analyzed in 1.6–2.6 mg aliquots (~ 4 –5 grains) using a CO_2 laser probe system (BrF_5 reagent) attached to a dual-inlet five-collector Finnigan/MAT 251 mass spectrometer. In cases where a given sample yielded two size populations of phenocrysts, aliquots were grouped comparatively by size. Measurements for unknowns were corrected by the average difference between measured and accepted values for UWG-2 Gore Mountain garnet standard ($\delta^{18}\text{O}_{\text{VSMOW}} = 5.80\text{‰}$, Valley *et al.*, 1995) measured on the same day. Daily standard deviation for UWG-2 was ± 0.08 – 0.10‰ (2SD, $n=8$). Duplicates were attempted for all runs but were obtained on only five of the nine samples analyzed (Table 3) owing to sample size and number of highest quality olivines available. Duplicate measurements of unknowns had an average reproducibility of $\pm 0.16\text{‰}$ for olivine (2SD).

The best olivine grains (i.e. pristine cores with few to no inclusions and no alteration) from each sample were also selected for SIMS. Mineral compositions determined by EMPA are within $15\ \mu\text{m}$ of SIMS analyses, but within $5\ \mu\text{m}$ of pits. Olivine grains were sorted based on relative size and cast in three 2.5 cm mounts. Unknowns and grains of the San Carlos olivine standard were placed within 5 mm of the center of each mount. Mounts were ground and polished to minimize grain topography to less than $1\ \mu\text{m}$ (Kita *et al.*, 2009). Reflected light and back-scattered electron images were taken of each grain prior to analysis to assess compositional zoning and select locations on individual grains to be measured *in situ* by electron microprobe and SIMS. Over 100 olivine phenocrysts from 21 samples (2–3 grains per sample; Table 3) were measured following the procedures of Kita *et al.* (2009) and Valley & Kita (2009). A CAMECA IMS-1280 large-radius, multi-collection SIMS system was used with a primary $^{133}\text{Cs}^+$ beam intensity of 1.5–1.8 nA (spot size $\sim 10\ \mu\text{m}$). The secondary ion beams for ^{16}O , $^{16}\text{O}^1\text{H}$, and ^{18}O were collected with Faraday cup detectors at MRP ~ 2500 (mass-resolving power). The OH/O ratio is a relative measure of the amount of hydrogen in the volume of olivine analyzed. Ratios of OH/O are background corrected by subtracting the OH/O in bracketing analyses of SCOL, to remove variability owing to sample and vacuum conditions and provide a sensitive check against cryptic hydrous alteration or contamination (Wang *et al.*, 2014). Given the wide range of olivine compositions (Fo-70 to Fo-90; Table 3) a calibration curve based on multiple olivine standards with Mg# from 100 to 1 (HN-OL, SCOL, OR-OL, Fayalite 50278; Supplementary Data Table A3; supplementary data are available for downloading at <http://www.petrology.oxfordjournals.org>) was used to correct for bias in the oxygen isotopic values of the unknowns relative to the San Carlos olivine standard (Valley & Kita, 2009). A bracketed average was

calculated from 3–4 analyses of the running standard (San Carlos olivine) before and after analyses of unknowns to yield an average standard precision of $\pm 0.28\text{‰}$ (2SD). Eight unknowns representing the most extreme $\delta^{18}\text{O}_{\text{ol}}$ values were also selected and an additional 5–6 analyses were taken from cores to test intra-grain reproducibility. The Core* value reported in Table 3 is the average of multiple spots in the core of a single olivine grain in an individual sample.

$^{40}\text{Ar}/^{39}\text{Ar}$ dating

Selected basalt samples dredged from seamounts and a basalt from the Possession Islands were crushed, sieved, leached with dilute HCl, washed in distilled water and hand-picked to remove phenocrysts and any altered material to produce a groundmass concentrate. The samples were irradiated in two batches. Samples for batch NM-217 were loaded into a machined Al disc and irradiated for 7 h in the D-3 position, Nuclear Science Center, College Station, TX. Samples for batch NM-251 were irradiated for 20 h in the C.T. position, US Geological Survey TRIGA, Denver, CO. Fish Canyon Tuff sanidine (FC-2), with an assigned age of 28.02 Ma (Renne *et al.*, 1998), was used as the neutron flux monitor in both batches.

Samples in batch NM-217 were measured using a Mass Analyzer Products 215-50 mass spectrometer on line with automated all-metal extraction system. Groundmass concentrates were step-heated using a Mo double-vacuum resistance furnace. Reactive gases were removed during a 12 min reaction with two SAES GP-50 getters, one operated at $\sim 450^\circ\text{C}$ and the other at 20°C . Gas was also exposed to a W filament operated at $\sim 2000^\circ\text{C}$ and a cold finger operated at -140°C . Samples in batch NM-251 were measured using an Argus VI mass spectrometer on line with an automated all-metal extraction system. Groundmass concentrates were step-heated by a 50 W Synrad CO_2 laser. Reactive gases were removed during a 2 min reaction with two SAES GP-50 getters. Getters, W filament and cold finger were operated at the same temperatures as batch NM-217. Electron multiplier sensitivities, blanks and other analytical parameters for both batches are reported in Table 1.

RESULTS

Field data—Adare Basin seamounts

The NBP0701 dredging campaign produced a total of $\sim 1000\text{lb}$ of rock from 17 sites within the Ross Sea (Supplementary Data Table A1 and Figs A1–A9). Ice-rafted debris (IRD) was recovered from all dredge sites, but a total of 48 *in situ* mostly basaltic lava samples were collected from the western flank of the Adare Trough and individual seamounts within the basin and on the continental shelf. The lava samples were initially distinguished shipboard from IRD by their angularity, absence of manganese coatings and glassy texture.

Further examination in thin section revealed a predominance of textures indicative of rapid undercooling (described below) as would be expected for lava erupted on the seafloor. The main strategy was to collect lava from these seamounts with increasing distance from the continent. Individual seamounts are steep-sided, conical-shaped edifices that range in height and basal diameter from ~ 100 m to >700 m and from <1 km to ~ 4 km, respectively, with minimum exposed volumes between 0.03 and 3 km³. In some areas, closely spaced seamounts are merged on elevated platforms (Supplementary Data Figs A7 and A8) that were most probably constructed by the coalescence of lava flows. The morphological characteristics of the seamounts are consistent with monogenetic volcanoes.

Four sites were dredged in the central portion of the Adare Trough. Samples from three of the sites (D1, D2 and D3) on the western flank at ~ 1000 to <2000 m below sea level (mbsl) include basaltic boulders and IRD such as dolerite and metamorphic rocks; all of the samples are coated with a thick layer of manganese oxide. Dredge D3 sampled a seamount exposed in the east-facing upper western scarp that appears to have been cut by the bounding normal fault of the trough (Supplementary Data Fig. A2). The other dredge lines on the western flank (D1 and D2) were positioned on the upper scarp facing away from any obvious seamounts in an attempt to sample oceanic crust (Supplementary Data Fig. A1). The fourth dredging site (D4) is a volcano duplet located in the middle of the Adare Trough at >2000 mbsl (Supplementary Data Fig. A3) and the samples acquired were mainly angular fragments of vesicular basalt and some pebbles and cobbles of IRD. The manganese oxide coating on these samples is very thin when compared with the samples from the western flank. A cluster of more than 100 seamounts was found in the southern portion of the Adare Basin and on the shelf. Thirteen of these seamounts were dredged. The shallowest ones (D5 to D7) on the continental shelf, ~ 15 nautical miles away from Cape Adare, are ~ 400 to 600 mbsl (Supplementary Data Figs A4 and A5) and heavily covered with coralline materials. The farthest seamount (D17), some 65 nautical miles from Cape Adare, is ~ 2000 to 1400 mbsl (Supplementary Data Fig. A9), is free of coralline materials.

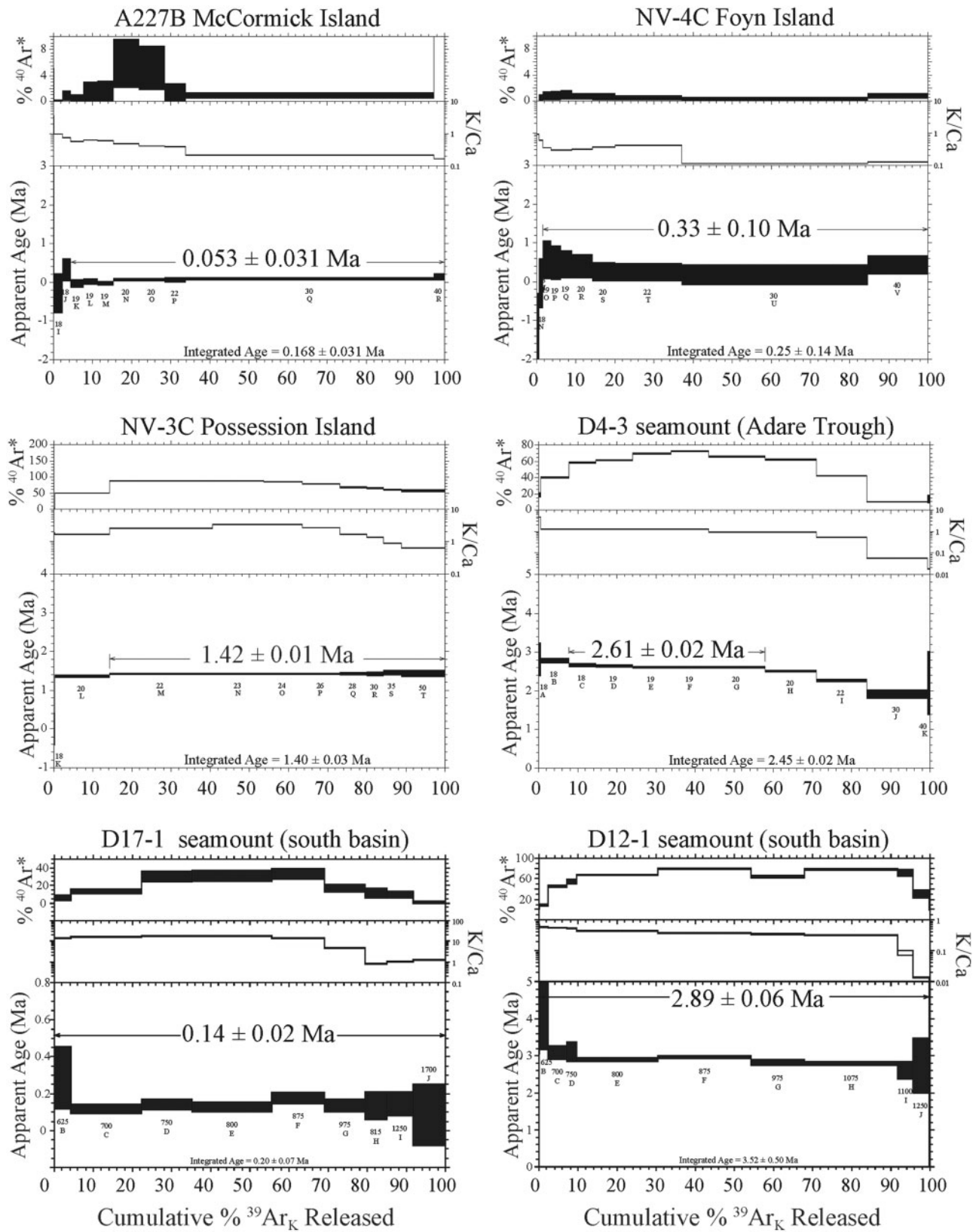
The seamounts were erupted through a thick (up to ~ 2000 m) sequence of sediments that has been accumulating in the basin since its opening at 43 Ma (Cande *et al.*, 2000); however, based on seismic stratigraphy that has been correlated to Deep Sea Drilling Project (DSDP) sites 273 and 274 (Granot *et al.*, 2010, and references therein) the sediments should be much younger (Early Oligocene to Pliocene). None of the seamounts sampled appear to be volcanically active, but the fact that a significant proportion of the lavas are glassy and lack manganese oxide coatings, except for those recovered from the western scarp of the Adare Trough, suggests that the volcanic activity in this region is relatively

young. Radial intergrowths (i.e. variolitic texture) of plagioclase and/or pyroxene in the glassy groundmass in many of the lavas indicate rapid undercooling, as would be expected with eruption on the seafloor. In this study, basalt from eight seamounts and basalt from the western scarp of the Adare Trough have been dated by the $^{40}\text{Ar}/^{39}\text{Ar}$ method to determine the age of volcanism and to provide further temporal constraints on the Neogene history of the Adare Basin. Furthermore, the age determinations are compared with the age of nearby onshore deposits to resolve the progression of magmatism in the NWRS region of the WARS.

$^{40}\text{Ar}/^{39}\text{Ar}$ chronology

New $^{40}\text{Ar}/^{39}\text{Ar}$ age dating results for four basalt samples dredged from the Adare Trough, five basalts from five different seamounts in the southern Adare Basin, and one basalt sample from a seamount located on the continental shelf, provide the first direct dating of oceanic volcanism in the NWRS. Additionally, five age determinations on basalt collected from the Possession Islands (two from Possession, two from Foyn and one from McCormick) provide the first age data for this island group. A rhyolite drop stone recovered at D17 was also dated to determine the age and provenance of the pyroclastic activity that produced it. The results and analytical details are provided in Table 1 and representative age release and Ca/K spectra are shown in Fig. 2. The remainder of the spectra and isotope correlation ($^{36}\text{Ar}/^{40}\text{Ar}$ vs $^{39}\text{Ar}/^{40}\text{Ar}$) diagrams are provided in Supplementary Data Fig. A10 and all $^{40}\text{Ar}/^{39}\text{Ar}$ analytical data are provided in Supplementary Data Table A2.

The new age data confirm the relatively young history of seamount volcanism in the NWRS. The ages range from 15.93 ± 0.76 Ma to 0.14 ± 0.02 Ma (Table 1), with a median value of 2.88 Ma. All of the seamounts dated are younger than 5 Ma, verifying the Pliocene age of the volcanism that was previously based on seismic stratigraphy (Granot *et al.*, 2010), but further reveal Pleistocene activity (≤ 2.6 Ma) at three seamounts (D4-3, D7-1 and D17-1). The middle Miocene age (~ 16 Ma) determined on basalt sample D2-1 collected on the western scarp face of the Adare Trough is too young to represent oceanic crust, which in this area has ages between 33.5 and 30.9 Ma (bounded by magnetic anomalies 12o and 13o; Granot *et al.*, 2010). Furthermore, its petrological characteristics are not those of oceanic crust formed at slow- to fast-spreading centers (also known as mid-ocean ridge basalt; MORB) but are the same as those of the seamounts (discussed below). The next oldest age determination at 4.61 ± 0.19 Ma (D3-1) is also from the western flank of the Adare Trough, but unlike D2-1 it was collected from a prominent seamount. It is interesting to note that this seamount is cut by the bounding fault, and if the age is representative of the seamount on the whole, then it would suggest fault activity younger than 4.6 Ma. Granot *et al.* (2010) concluded that uplift of the western flank of the Adare



Downloaded from https://academic.oup.com/petrology/article/59/3/517/4966906 by guest on 21 August 2022

Fig. 2. Representative ⁴⁰Ar/³⁹Ar ages for NWRS basalts. Age release, radiogenic argon release (⁴⁰Ar*) and Ca/K spectra on ground-mass concentrates are shown. Thickness of boxes for apparent age represent 2σ error.

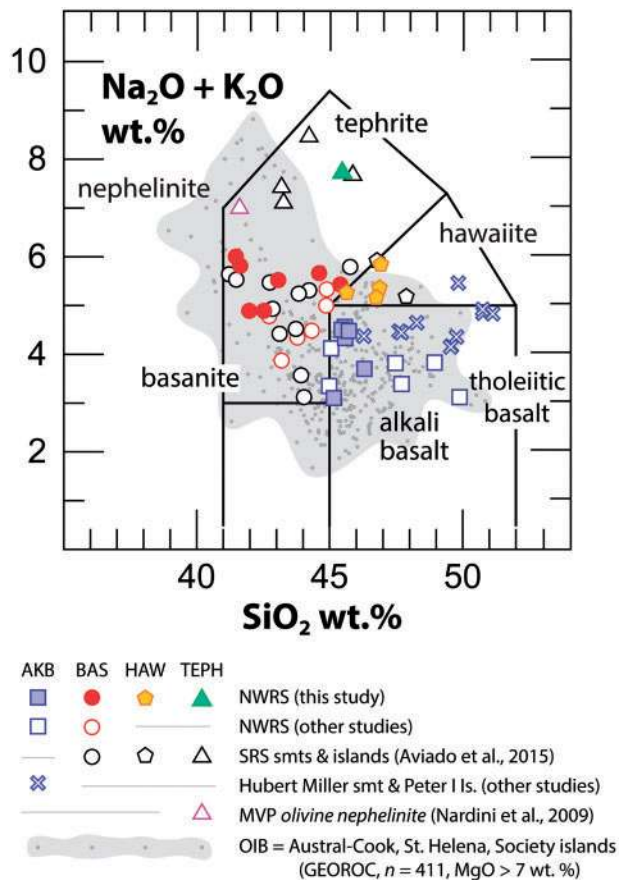


Fig. 3. Total alkalis vs SiO₂ (wt %) classification of basalts (Le Bas *et al.*, 1986). Thirty basalts from the NWRS (sample locations are shown in Fig. 1b and compositions in Table 2) are marked by solid color symbols (this study, $n = 18$), and open color symbols ($n = 12$) are analyses from Rocholl *et al.* (1995), Mortimer *et al.* (2007), Nardini *et al.* (2009) and Aviado *et al.* (2015). Southern Ross Sea (SRS) seamounts and islands (open black symbols) are from Aviado *et al.* (2015) and the Hubert Miller seamount (Marie Byrd seamount group) and Peter I Island (blue crosses) are from Hart *et al.* (1995) and Kipf *et al.* (2014). One sample (violet triangle, olivine nephelinite, SAX20, Nardini *et al.*, 2009) is from the Melbourne volcanic province (MVP), which lies adjacent and to the south of the NWRS area. All basalts plotted have MgO > 6 wt % and are normalized to 100% volatile-free with total Fe as FeO. Over 400 ocean island basalts (OIB) from the Saint Helena, Austral-Cook and Society Islands (GEOROC database, MgO > 7 wt %) are shown for comparison and include those derived from the melting of enriched (EM) and high U/Pb (HIMU) mantle sources.

Trough occurred much earlier (~17 Ma) but that vertical normal faulting may be younger and, in places, still active. The age determined for the western flank seamount is ~1 Myr older than the seamount dated in the center of the Trough (D4). The two age determinations from this volcano (2.51 ± 0.09 Ma and 3.35 ± 0.11 Ma) bracket the range determined for four of the five seamounts dated in the southern Adare Basin (Table 1). The two youngest seamount samples, one from the continental shelf (D7-1, 0.32 ± 0.23 Ma) and the other from the easternmost seamount dredged within the basin (D17-1, 0.14 ± 0.02 Ma), reveal significantly younger, Pleistocene activity.

The Possession Islands are the closest land deposits to the Adare Basin and are located adjacent to the Adare Peninsula (Fig. 1b). Age determinations for five basalts collected from three islands range from 1.42 ± 0.01 Ma to 0.053 ± 0.031 Ma (Table 1) and have a median value of 0.24 Ma. The new ages represent the youngest volcanic activity yet recorded within the Hallett volcanic province. Smellie *et al.* (2011) provided ⁴⁰Ar/³⁹Ar age data as well as a compilation of ages from previous dating campaigns (⁴⁰Ar/³⁹Ar and K–Ar ages) that range from ~13.8 Ma to ~2.3 Ma. The youngest date, 2.27 ± 0.5 Ma (K–Ar age; McIntosh & Kyle, 1990), is from Cape Roget located at the southern end of the Adare Peninsula and within 15 km of Foyen Island (Possession Islands).

Previous studies indicate that there is no overall migration of activity within the Hallett volcanic province; however, three overlapping volcanic centers on the Daniell Peninsula (Fig. 1b) show a northward-younging age progression over a period of ~5 Myr between ~10 Ma and ~5 Ma (Smellie *et al.*, 2011). New age determinations in this study show that there has been a very broad northeasterly shift in the location and volume of eruptive activity in the NWRS from continental shield volcanism along the coastline in the middle to late Miocene (~14 to > 5 Ma) to monogenetic island and seamount volcanism on the continental shelf and Adare Basin in the Pliocene to Pleistocene (< 5 Ma to < 100 ka). Evidence for this broad shift in activity is underscored when taking into account the occurrence of Eocene–Oligocene (48–23 Ma) plutonic and subvolcanic alkaline rocks (Meander Intrusive Group), which are found within the Melbourne volcanic province (Kyle, 1990) immediately adjacent to and to the SW of the Hallett volcanic province, and are considered the earliest expression of WARS magmatism (Rocchi *et al.*, 2002).

Petrography and mineral chemistry

Twenty of the 30 basalts analyzed for whole-rock chemistry and isotopes for the NWRS were examined petrographically. Their phenocrysts were analyzed by Krans (2013).

Basalts from the NWRS are porphyritic and groundmass ranges from holocrystalline to holohyaline with pilotaxitic to trachytic textures. The glassy groundmasses are most prominent in seamount samples. The samples are variably vesicular and some basalts from seamounts display amygdaloidal textures, with vesicles partially filled with calcite and clay material. Olivine and clinopyroxene are the dominant phenocryst phases, with subordinate plagioclase and amphibole. Plagioclase and magnetite are common groundmass phases, with lesser amounts of clinopyroxene, olivine and amphibole. In a few samples plagioclase is absent altogether.

Olivine is euhedral to subhedral. It often contains inclusions of opaque oxide and melt inclusions that make up to 2% by volume. In seamount samples skeletal crystals of olivine are common and are the result of

quench crystallization owing to rapid undercooling. Also in seamount samples some olivine grains show minor alteration to iddingsite along cleavage fractures. The forsterite (Fo) content [$100\text{Mg}/(\text{Mg} + \text{Fe}^{2+})$] of olivine ranges from Fo70 to Fo90 with an average of Fo81. Most olivines display weak to strong normal zoning (decrease of 1–17 mol% Fo), with rare reverse (up to 3 mol% increase in Fo) and oscillatory zoning.

Clinopyroxene is euhedral to subhedral with up to 3 vol. % opaque oxide and melt inclusions. In seamount samples microphenocrysts of clinopyroxene often occur as radial intergrowths (variolitic texture) with plagioclase that, like the occurrence of skeletal olivine, indicate a high degree of undercooling. Clinopyroxene phenocrysts are bimodal in their size distribution. The larger phenocrysts (≥ 0.5 mm) often exhibit disequilibrium textures with spongy cores and prominent zoning, whereas smaller phenocrysts (< 0.5 mm) are euhedral to subhedral and are only occasionally zoned. The clinopyroxenes are classified as diopside and core compositions are in the range of Wo 37–52, En 31–52 and Fs 7–21, with $\text{Mg}\#_{\text{cpx}}$ varying from 70 to 90. Diopside phenocrysts generally display weak to strong normal zoning (up to 3% decrease in $\text{Mg}\#_{\text{cpx}}$ from core to rim) and less common, reverse zoning (up to 3% increase in $\text{Mg}\#_{\text{cpx}}$ from core to rim).

Plagioclase phenocrysts are present in only six of the 20 NWRS basalts examined. Euhedral plagioclase phenocrysts have core compositions that range from An42 to An69; most are subhedral to anhedral with sieve textures and reaction rims. In addition, they are reversely zoned with anorthite contents that show an increase from core to rim by up to 22 mol%. The evidence for disequilibrium in the majority of plagioclase suggests that they are antecrysts (i.e. crystals that formed earlier in the differentiation process and have been reincorporated into the magma).

Amphibole phenocrysts are less common, observed in five of the 20 basalts examined, and typically exhibit weak to extensive reaction rims. The amphibole is ferri-kaersutite, following the classification scheme and nomenclature of Hawthorne *et al.* (2012), with $\text{Mg}\#_{\text{amp}}$ 66–72. Kaersutitic amphibole is often found in alkaline basalts and xenoliths within the NWRS and the adjacent Melbourne Volcanic Province (Kyle, 1986; Rocchi *et al.*, 2002; Coltorti *et al.*, 2004; Perinelli *et al.*, 2006, 2011; Armienti & Perinelli, 2010; Perinelli *et al.*, 2017).

Major and trace element characteristics

The whole-rock composition of the 30 selected NWRS basalts includes alkali basalt, basanite, hawaiite and tephrite (Table 2, Fig. 3). All were selected to represent relatively unfractionated compositions ($\text{MgO} \geq 6$ wt %) and include deposits located on the continent, continental shelf and oceanic Adare Basin (Fig. 1b). The major and trace element compositions of NWRS basalts are plotted in Figs 3–5 with other basalts ($\text{MgO} \geq 6$ wt %) from seamounts and islands located in the southern

Ross Sea (Terror Rift basin; Aviado *et al.*, 2015) and in the Amundsen Sea off the Marie Byrd Land coastline (Hubert Miller seamount and Peter I Island: Hart *et al.*, 1995; Kipf *et al.*, 2014) (Fig. 1a). The purpose is to compare basalts derived from melting beneath regions that have minimum crustal thicknesses and from oceanic settings that are considered to be related to the WARS. Also shown are a selection of mafic alkaline ocean island basalts (OIB) from the Atlantic and southern Pacific oceans whose geochemical characteristics (and isotopic signatures discussed below) have been repeatedly likened to basalts from the WARS.

The composition of NWRS basalts ranges from strongly silica-undersaturated (*Ne*-normative > 8 to 21 wt %) basanite and tephrite to more moderately silica-undersaturated (*Ne*-normative ≤ 11 wt %) hawaiite and alkali basalt, two of which are silica-saturated (*Hy*-normative) (Table 2). In addition to their higher silica and lower total alkali ($\text{K}_2\text{O} + \text{Na}_2\text{O}$) contents, the alkali basalt also has overall lower TiO_2 and P_2O_5 (Fig. 4) and lower concentrations of highly incompatible trace elements (e.g. La, Ce, Sr and Zr) relative to basanite and tephrite (Fig. 5). The overall compositional spectrum of the NWRS basalt matches that of WARS basalt from the southern Ross Sea (Aviado *et al.*, 2015) and Amundsen Sea (Hart *et al.*, 1995; Kipf *et al.*, 2014) as well as OIB, with the notable exception of Yb, which is much lower in concentration for Peter I Island (Fig. 5). There are no distinct compositional trends on plots of major and trace elements versus MgO wt % with the exception of Al_2O_3 and Cr (Figs 4 and 5). The variation in concentration of these elements with decreasing MgO content indicates an overall control by clinopyroxene during magmatic differentiation. Nickel contents (not shown) decrease with MgO in samples with Ni < 250 ppm, indicating olivine control.

Primitive mantle normalized trace element patterns (Fig. 6a–c) of basalts from the NWRS, along with other WARS basalts, display enriched patterns and well-developed K and Pb negative anomalies for nearly all samples. Alkali basalts are again distinguished from basanite (and tephrite) by having overall lower elemental concentrations, less pronounced K and Pb anomalies and small negative P anomalies (Fig. 6b). All of the basalts are enriched in light rare earth elements (LREE) relative to heavy REE (HREE), which is typically linked to garnet control during small degrees of mantle partial melting. Alkali basalts have lower La_N/Yb_N ratios (≤ 15) compared with basanites and tephrites ($\text{La}_N/\text{Yb}_N \geq 12$ –27) in NWRS samples, contributing to their slightly flatter patterns. Chondrite-normalized REE plots of NWRS and other WARS basalts lack Eu anomalies (Eu/Eu^* between ~ 0.9 and 1.1) indicating that the magmas were not influenced by the fractionation or accumulation of plagioclase. All of the WARS basalts fall within the compositional range of OIB and display very similar trace element distribution patterns.

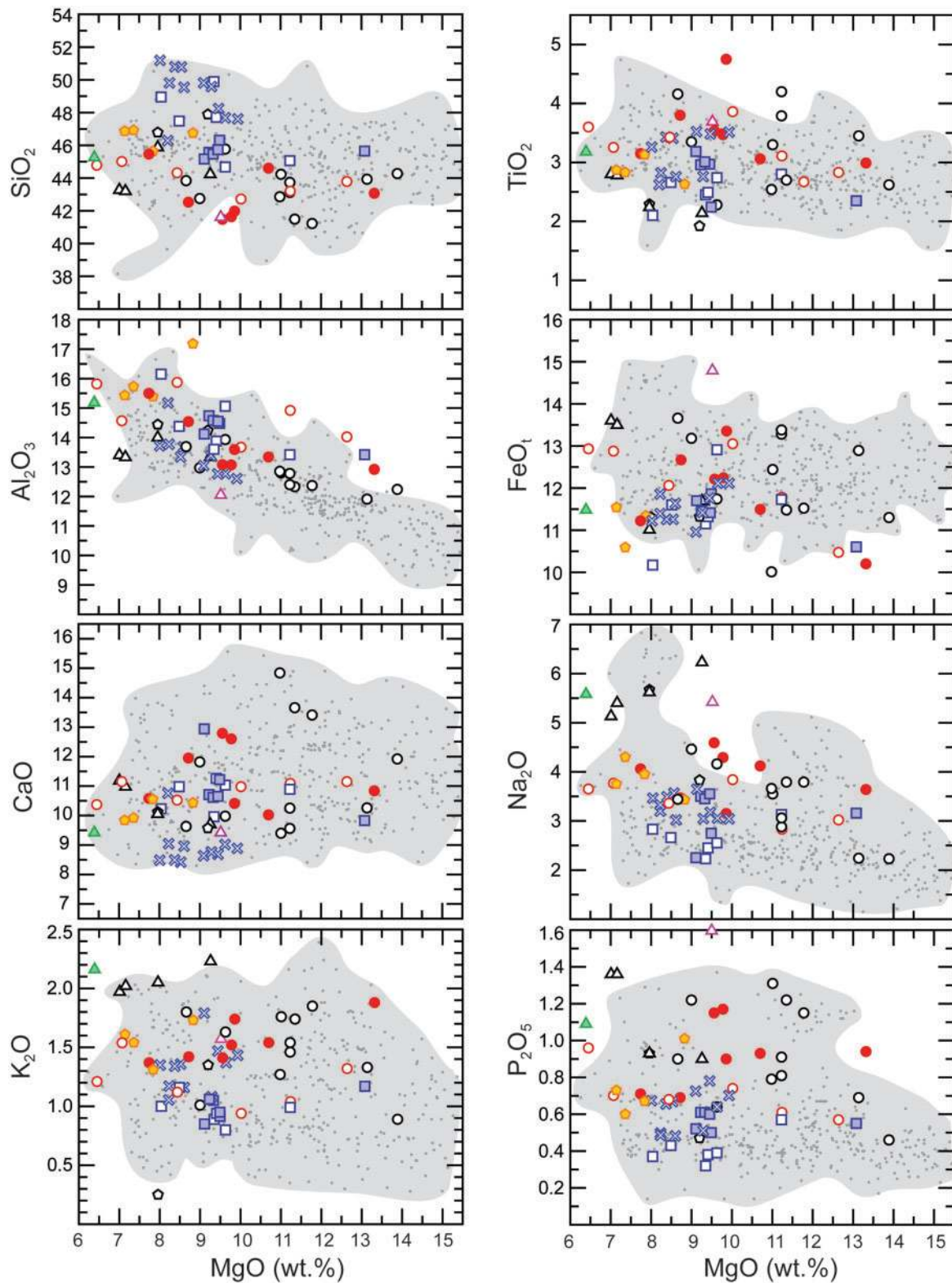


Fig. 4. Major elements (wt %) vs MgO (wt %). References, symbols and data criteria are given in Fig. 3 and Table 2.

Sr–Nd–Pb isotopes

Radiogenic isotope ratios for NWRS basalts are reported in Table 2 and plotted with other WARS basalts and alkaline OIB in Fig. 7. Apart from one sample from the Malta Plateau (MA009a), NWRS basalts

encompass a moderate range in measured $^{87}\text{Sr}/^{86}\text{Sr}$ (0.70278–0.70379) and a narrow range in measured $^{143}\text{Nd}/^{144}\text{Nd}$ (0.51282–0.51300). Pb isotope compositions measured for NWRS basalts also show a restricted range in $^{207}\text{Pb}/^{204}\text{Pb}$ (15.52–15.68) and a

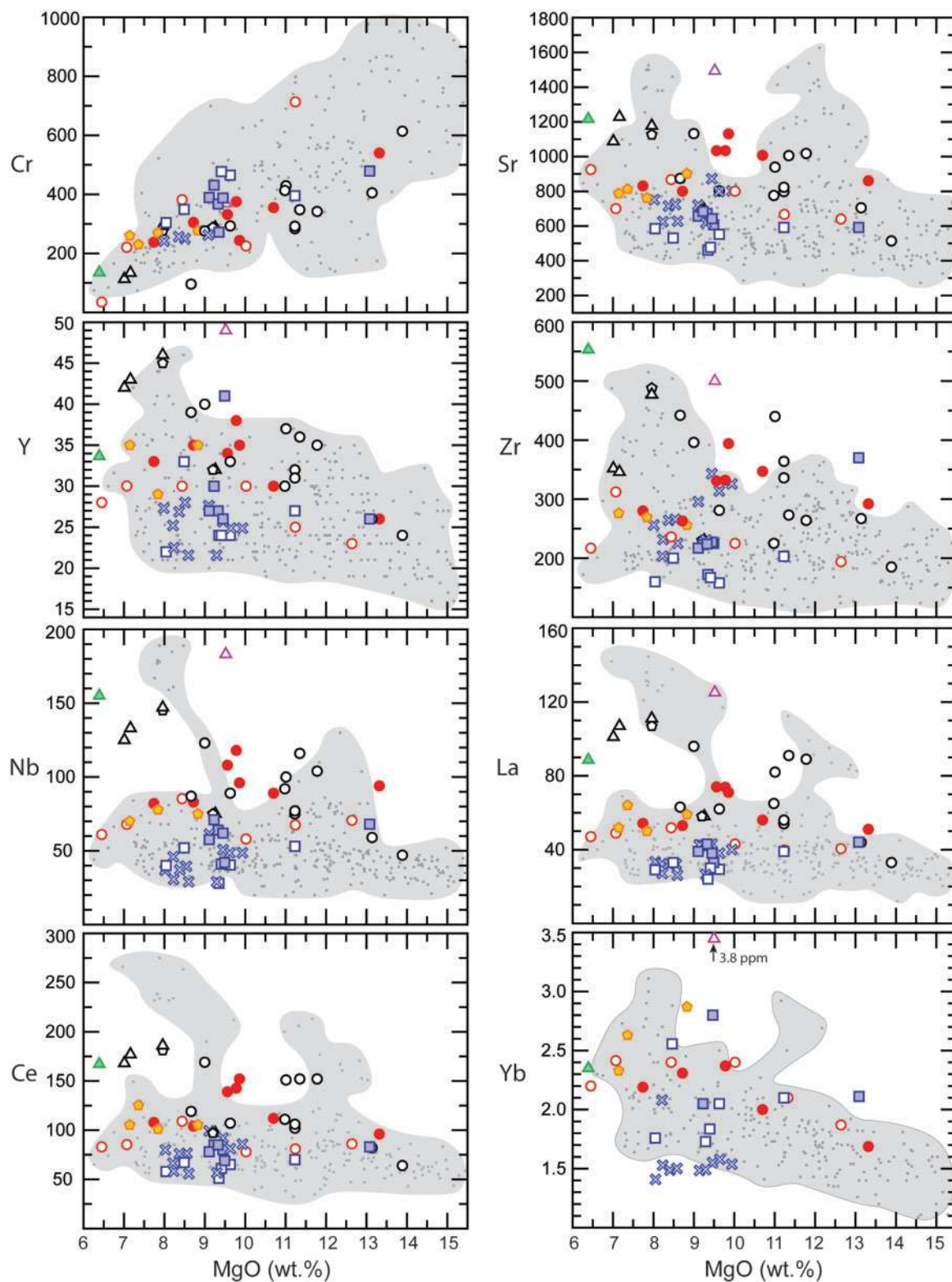


Fig. 5. Selected trace elements (ppm) vs MgO (wt %). Symbols and data criteria are given in Fig. 3 and Table 2.

moderately wide range in $^{208}\text{Pb}/^{204}\text{Pb}$ (38.81–39.92) and $^{206}\text{Pb}/^{204}\text{Pb}$ (19.22–20.23). Values for other WARS basalts fall within the same range, except for Peter I Island, which has a much higher $^{207}\text{Pb}/^{204}\text{Pb}$ (>15.7) that is explained by derivation from a localized EMII-like

source (Hart *et al.*, 1995; Kipf *et al.*, 2014). Seven NWRS basalts have high $^{206}\text{Pb}/^{204}\text{Pb}$ (> 20), six of which also have low $^{87}\text{Sr}/^{86}\text{Sr}$ (< 0.7030) and high $^{143}\text{Nd}/^{144}\text{Nd}$ (> 0.5129) (Table 2). The isotopic signatures coupled with their OIB-like compositional characteristics trend

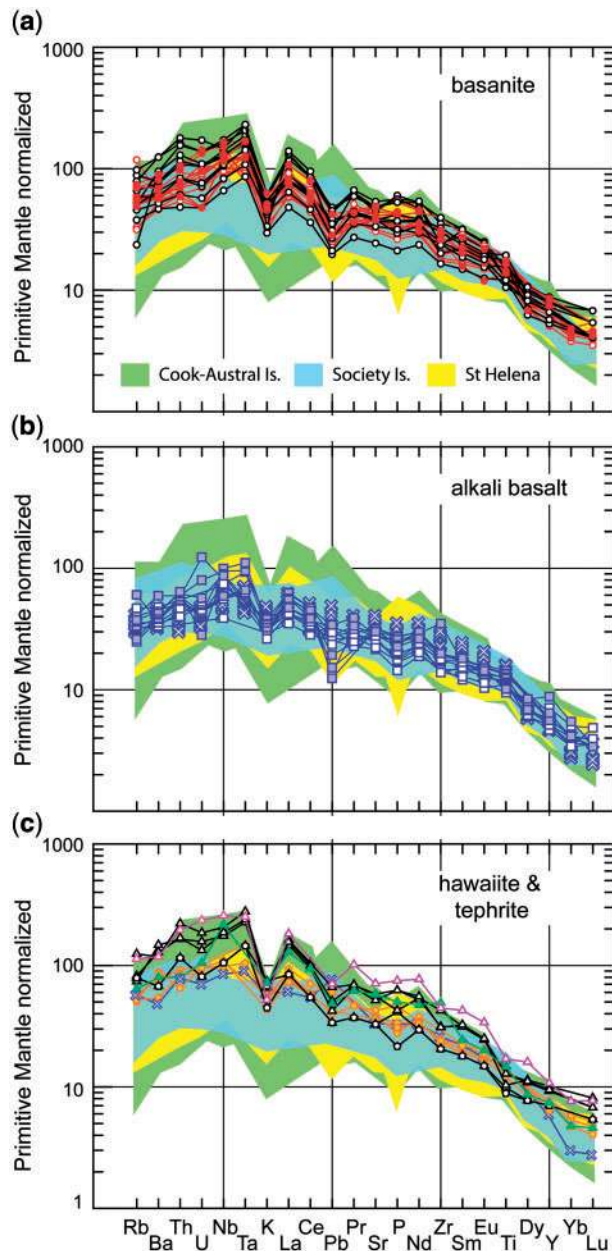


Fig. 6. Primitive mantle normalized (Sun & McDonough, 1989) trace element diagrams. References, symbols and data criteria are the same as in previous figures.

towards what has been referred to as HIMU [i.e. derived from melting of a mantle source with high- $\mu = ({}^{238}\text{U}/{}^{204}\text{Pb})_{t=0}$] (Rocholl *et al.*, 1995; Hart *et al.*, 1997; Panter *et al.*, 1997, 2000, 2006; Rocchi *et al.*, 2002; Nardini *et al.*, 2009; Martin *et al.*, 2013; Kipf *et al.*, 2014; Aviado *et al.*, 2015). Nevertheless, most of the basalts in this study fall within the range of OIB compositions assigned to a PREMA (PREvalent MAnTle; Zindler & Hart, 1986) mantle source; specifically falling within the DM (Depleted Mantle)–PREMA array as defined by Stracke (2012, and references therein). The development of the DM–PREMA array is attributed to the continuous subduction and aging of MORB-type crust

during recycling through the mantle (Stracke *et al.*, 2005). Alternatively, PREMA, which is very similar, if not identical, to the so-called focal zone (FOZO; Hart *et al.*, 1992) or the common component ('C'; Hanan & Graham, 1996) in the mantle sources of oceanic basalts, is the lithospheric mantle portion of the subducting slab (Castillo, 2015, 2016). Accordingly, the DM–PREMA array may simply be the long-time (some billions of years) integrated record of geochemical depletion of the upper mantle with time, from Bulk Silicate Earth (BSE) to modern DMM (Depleted MORB Mantle).

Oxygen isotopes

Oxygen isotopic compositions determined by conventional laser fluorination (LF) and by secondary ionization mass spectrometry (SIMS) for NWRS basalts are listed in Table 3 and plotted against olivine Fo content and whole-rock MgO in Fig. 8. Oxygen isotopes measured by LF for nine NWRS basalts range from 4.86 to 5.26‰. Overall, the average LF values for NWRS olivine in this study ($5.03 \pm 0.16\text{‰}$, 2SD) are statistically indistinguishable from average olivine LF values ($\delta^{18}\text{O} = 5.29 \pm 0.13\text{‰}$, 2SD) reported for other Northern Victoria Land (NVL) basalts (Nardini *et al.*, 2009), as well as olivine LF values ($\delta^{18}\text{O} = 5.29 \pm 0.18\text{‰}$, 2SD) from xenoliths hosted in NVL basalts, which are considered to represent cumulates from near-primary mantle melts (Perinelli *et al.*, 2011).

Olivine measured by SIMS, including core and rim analyses, and multiple analyses on single grain cores (Core*), vary from 4.4 to 5.9‰ (range = 1.5‰) and average $5.21 \pm 0.26\text{‰}$ (2SD, number of samples $n_s = 21$, number of analyses $n_a = 176$). Intra-crystal variations in $\delta^{18}\text{O}_{\text{ol}}$ are as much as 0.6‰ lighter to 0.5‰ heavier at rims than cores (average $\Delta_{\text{core-rim}} = 0.02\text{‰}$) and are not statistically significant with respect to instrument precision based on the SCOL standard ($\pm 0.28\text{‰}$ at 2SD). The lowest single spot $\delta^{18}\text{O}_{\text{ol}}$ values are from samples NV-4 (4.5‰) and NV-4C (4.4‰), with average values being slightly higher at $4.82 \pm 0.18\text{‰}$ ($n_a = 7$) and $4.66 \pm 0.25\text{‰}$ ($n_a = 13$), respectively. The highest single spot $\delta^{18}\text{O}_{\text{ol}}$ values are from samples MA-009a and MA-117 (5.9‰), with averages at $5.54 \pm 0.22\text{‰}$ ($n_a = 14$) and $5.57 \pm 0.26\text{‰}$ ($n_a = 13$), respectively. The difference between single spot analysis of high and low $\delta^{18}\text{O}_{\text{ol}}$ values is resolvable beyond analytical precision.

SIMS $\delta^{18}\text{O}_{\text{ol}}$ average values are not statistically different from LF average values for individual samples (Table 3) or for the dataset as a whole (Fig. 8). Multiple core analyses on single grains measured by SIMS (Core*) are either indistinguishable (e.g. NV-4) or heavier (e.g. D4-3 and MA-117) relative to LF (Table 3). It is interesting to note that out of the seven samples measured using the Core* technique, five show heavier values (A225A, D4-3, MA-009a, MA-117 and P74833) than standard SIMS measurements. It should be recalled that the standard measurement is an average of multiple spots on two to three grains (mostly cores but includes some rims) and that Core* is the average of

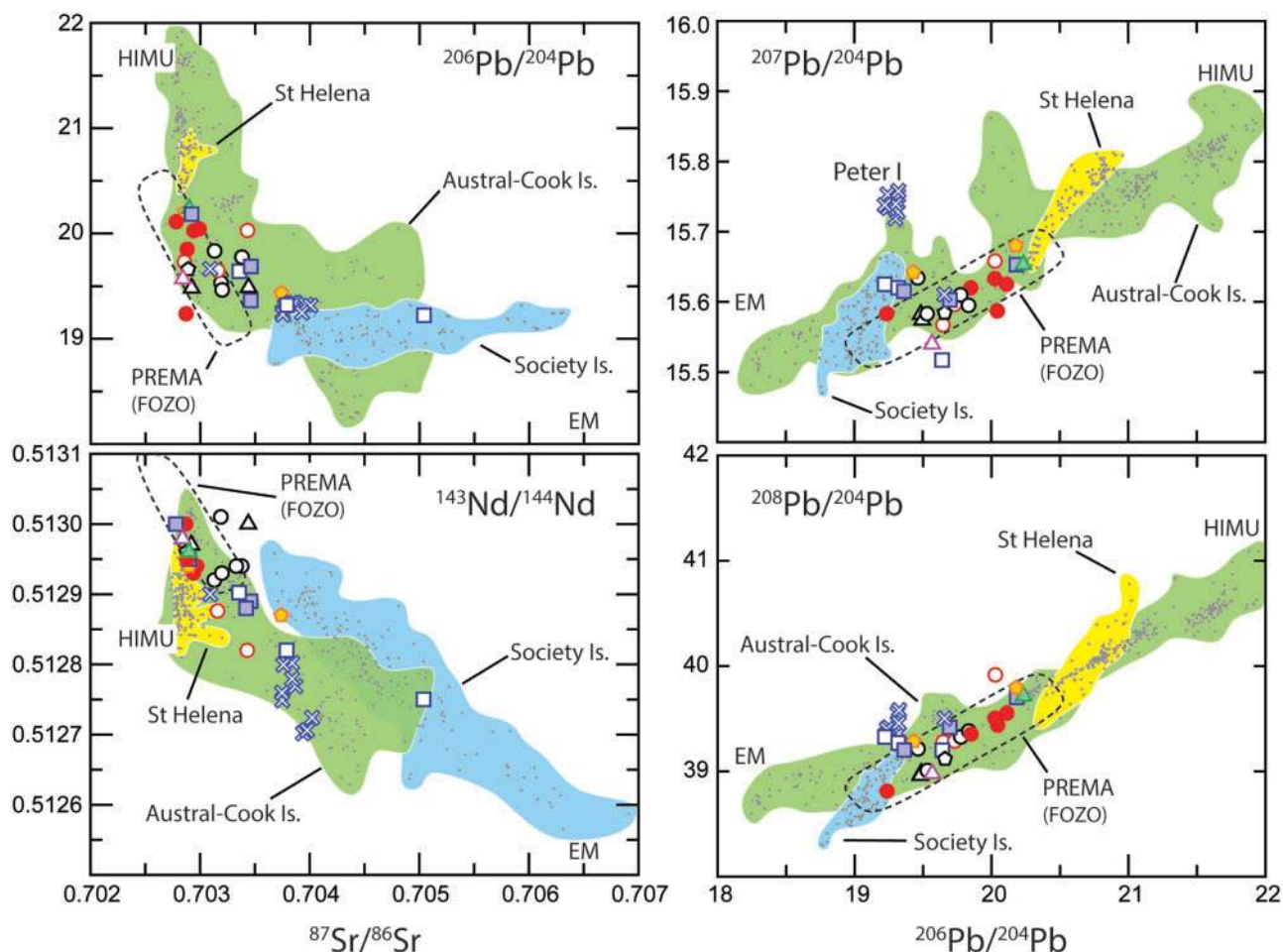


Fig. 7. Measured Radiogenic isotope (Sr, Nd, Pb) compositions of Antarctic basalts compared with ocean island basalts. Mantle source endmembers PREMA (FOZO), HIMU and EM are taken from [Stracke \(2012\)](#). References, symbols and data criteria are given in [Fig. 3](#) and [Table 3](#). Basalts MA009a and MA-117 from the Malta Plateau ([Rocholl et al., 1995](#)) were measured for Pb isotopes in this study and the results are presented in [Table 2](#).

multiple spots in the core of one grain only. It is possible that there is some sampling bias contributing to the difference between the two techniques but, if so, the differences fall within analytical precision.

All $\delta^{18}\text{O}_{\text{ol}}$ analyses by SIMS and LF (this study and [Nardini et al., 2009](#)) are plotted against Fo % and presented in [Fig. 8a](#). Also plotted is a range of mantle olivine values from peridotite (LF; [Mattey et al., 1994](#)) and olivine data from basalts at several oceanic locations that include the Canary Islands (LF and SIMS; [Gurenko et al., 2006, 2011](#)), Reykjanes Peninsula, Iceland (LF; [Peate et al., 2009](#)) and the Azores Islands (LF; [Grenske et al., 2013](#)), all of which have also been interpreted to represent mantle values. The LF data for NWRS olivine have nearly the same range in values as measured for the Canary and Azores islands. Individual SIMS analyses for NWRS olivine have a greater range, encompassing these islands and most $\delta^{18}\text{O}_{\text{ol}}$ values for OIB measured by LF ([Eiler, 2001](#)). However, the average value of all $\delta^{18}\text{O}_{\text{ol}}$ analyses in this study ($5.20 \pm 0.25\text{‰}$) is similar to average mantle $\delta^{18}\text{O}_{\text{ol}}$ ($5.18 \pm 0.28\text{‰}$; [Mattey et al., 1994](#)). There is neither an overall

correlation between Fo content and $\delta^{18}\text{O}_{\text{ol}}$ nor a correlation with respect to whole-rock composition (i.e. basanite, alkali basalt, etc.). There is a very weak positive correlation, however, when considering only LF analyses (this study and [Nardini et al., 2009](#)). In [Fig. 8b](#), whole-rock MgO (wt %) is plotted versus average $\delta^{18}\text{O}_{\text{ol}}$ LF and SIMS data for each sample. Again, there is a very weak positive correlation (i.e. lighter $\delta^{18}\text{O}_{\text{ol}}$ with decreasing MgO content) mainly exhibited by LF analyses, but when considering both SIMS and LF data for basanite and alkali basalt there is no correlation; in fact, nearly the full range of $\delta^{18}\text{O}_{\text{ol}}$ values for NWRS basalt falls between 9 and 10 wt % MgO ([Fig. 8b](#)).

$\delta^{18}\text{O}_{\text{ol}}$ analyses by SIMS and LF averaged for each sample are plotted against measured Sr, Nd and Pb isotopic compositions, as shown in [Fig. 9](#). There is a broad correlation between oxygen and radiogenic isotopes, where lower $\delta^{18}\text{O}_{\text{ol}}$ corresponds to lower $^{87}\text{Sr}/^{86}\text{Sr}$ and higher $^{143}\text{Nd}/^{144}\text{Nd}$ and $^{206}\text{Pb}/^{204}\text{Pb}$ ratios (as well as $^{207}\text{Pb}/^{204}\text{Pb}$, not shown). Significantly, a similar relationship had been generally observed in OIB samples ([Eiler et al., 1996](#)).

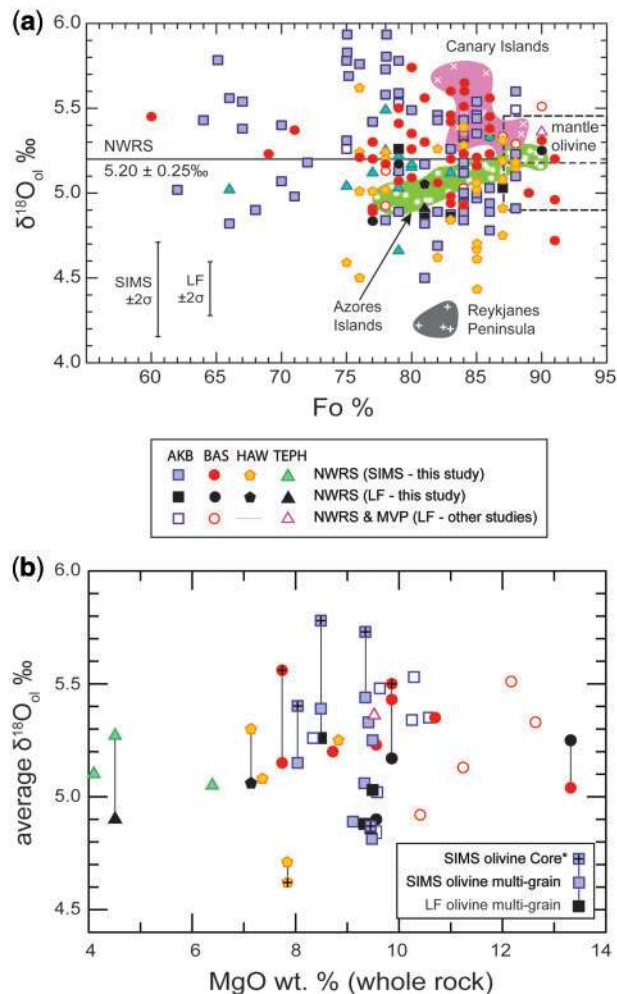


Fig. 8. Relationships between $\delta^{18}\text{O}_{\text{ol}}$ and (a) average Fo % and (b) whole-rock MgO wt %. Oxygen isotope compositions of olivine were measured by SIMS (single spot) and LF (4–5 grains) analysis for NWRS samples (this study) and LF analyses of olivine from other NVL basalts, including those in the NWRS and MVP (Mortimer *et al.*, 2007; Nardini *et al.*, 2009). (a) $\delta^{18}\text{O}_{\text{ol}}$ obtained by SIMS and Fo% by EMPA include both cores and rims of individual olivine grains, comprising a total of 21 samples (Table 3). The line marking the average $\delta^{18}\text{O}$ value of NWRS olivine ($5.20 \pm 0.25\text{‰}$, 2SD) is based on 190 analyses, including nine samples by LF (Table 3). The Fo content for samples analyzed by LF is the average of multiple grains determined by EMPA in same sample. The dashed field for mantle olivine represents an average value of $5.18 \pm 0.28\text{‰}$ at 2SD (LF; Matthey *et al.*, 1994) and Fo % of 87–96 (Deer *et al.*, 1992). For comparison, values for olivine from the Canary Islands (LF and SIMS; Gurenko *et al.*, 2006, 2011), Reykjanes Peninsula, Iceland (LF; Peate *et al.*, 2009) and the Azores Islands (LF; Genske *et al.*, 2013) are shown. (b) SIMS $\delta^{18}\text{O}_{\text{ol}}$ are the average of all spot analyses within a single sample (cores and rims on several grains). Tie-lines connect individual samples that have been analyzed by multiple methods. Core* is the average $\delta^{18}\text{O}_{\text{ol}}$ value of 5–6 spots within the core of a single olivine grain.

Geochemical and isotopic variation across the ocean–continent transition

The 30 basalts from the NWRS (Table 2 and Fig. 1b) are plotted versus decimal degree longitude in Fig. 10 and display systematic variations in major and trace elements as well as isotopic ratios across the transition

from land to sea. Oceanward, the basalts show an increase in total alkalis, silica-undersaturation ($Ne + Lc$ normative, not shown), P_2O_5 and incompatible trace elements Sr, Zr, Nb, LREE (not shown), and LREE/HREE ratios. Also towards the ocean, the $^{87}\text{Sr}/^{86}\text{Sr}$ ratios decrease and $^{143}\text{Nd}/^{144}\text{Nd}$ and $^{206}\text{Pb}/^{204}\text{Pb}$ ratios increase. Trends in $^{207}\text{Pb}/^{204}\text{Pb}$ and $^{208}\text{Pb}/^{204}\text{Pb}$ isotopes (not shown), although poorly defined, also generally increase oceanward. Variations in oxygen isotopes are less well defined but when samples classified as alkali basalt are considered (Figs 1b and 3) there is a general decrease (i.e. values become lighter) towards the ocean (Fig. 10). The systematic compositional variation requires the evaluation of gradational changes in mantle source, melting processes and/or contamination of the melt as it rises through the lithosphere.

DISCUSSION

The main objective of this study is to better understand the mantle sources and processes responsible for the production of alkaline magmas within the WARS. The unique contribution of this research relative to past efforts is the location of our basaltic sample suite, which encompasses both oceanic and continental domains (Fig. 1). Given their similar composition and roughly equivalent age, the oceanic and continental basalts must share a common origin and therefore provide an effective assessment of the role of continental lithosphere in magma genesis. In addition, the NWRS was located adjacent to the former pan-Pacific margin of Gondwana, where subduction dominated the tectonic regime from the Neoproterozoic to the Late Cretaceous (~450 Myr); thus, the influence of subduction-related processes on mantle source domains is also examined.

Contamination by crust?

The increase in silica-saturation, and correlation of higher $^{87}\text{Sr}/^{86}\text{Sr}$ and lower $^{143}\text{Nd}/^{144}\text{Nd}$ with higher $\delta^{18}\text{O}_{\text{ol}}$ values in NWRS basalts erupted on the Antarctic continent might suggest that the magmas have assimilated crust. Contrary to this presumption is the fact that our ‘continental’ samples are also distinguished by having lower incompatible element concentrations relative to their oceanic counterparts (Fig. 10). Progressive assimilation of silicic crust coupled with fractional crystallization (AFC; DePaolo, 1981) should produce the opposite relationship. In Fig. 11 we have modeled the effects of AFC processes using a variety of crustal rock types found within NVL. The plots clearly show that the assimilation of these rocks by basaltic magmas will lead to lower Nd and higher Sr isotopic signatures, but will also produce higher concentrations of incompatible elements such as Rb (as well as Nb, Zr, Ba, LREE) even if they are significantly lower in the assimilant (e.g. gabbro). Furthermore, there is no systematic increase or decrease in MgO, Al_2O_3 and CaO or weakly incompatible to compatible trace element (e.g. Y, Yb, Cr) contents

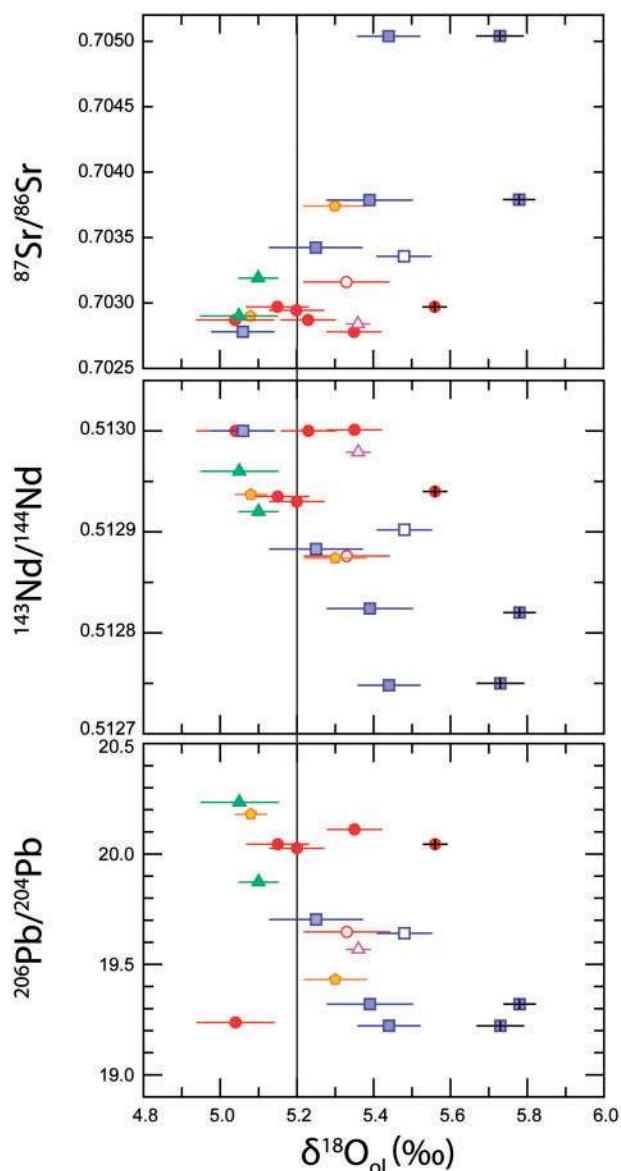


Fig. 9. $\delta^{18}\text{O}_{\text{ol}}$ vs measured Sr, Nd and Pb isotope compositions. The oxygen isotopic values for olivine phenocrysts from NWRS basalts are LF (open symbols) and SIMS data averaged for multiple spots on 2–3 grains in each sample (Table 3). Error bars are standard error of the mean (SEM). Symbols for the basalts are the same as those given in Fig. 8. Radiogenic isotope ratios are measured values on whole-rocks. Vertical line marks the average $\delta^{18}\text{O}$ value of NWRS olivine (5.20‰) calculated for all analyses ($n = 190$).

from ocean to continent, which would be very difficult to explain if the continental basalts were preferentially contaminated by crust. However, simple mixing of magma with mafic rocks such as gabbro or eclogite could predict many of the geochemical and Sr–Nd isotopic variations but require a mixture that consists of $\geq 40\%$ of those crust types. Achieving this proportion, especially at shallow depths with relatively small volumes of magma, is unlikely.

Oxygen isotopes have long been used to assess contamination of magma by crust and are a particularly strong tool for detecting the assimilation of ^{18}O -rich

continental rocks by mantle-derived magmas (Harmon & Hoefs, 1995; Eiler, 2001, and references therein). In cases where anomalously light oxygen isotope signatures for olivine (i.e. low $\delta^{18}\text{O}_{\text{ol}}$) occur in OIB, they have been attributed to the assimilation of hydrothermally altered oceanic lower crust (Hart *et al.*, 1999; Skovgaard *et al.*, 2001; Genske *et al.*, 2013) or cannibalization of hydrothermally altered lavas within the volcanic edifice itself (Wang & Eiler, 2008; Garcia *et al.*, 2008). A rough positive correlation between $\delta^{18}\text{O}_{\text{ol}}$ and Fo %, first reported by Nardini *et al.* (2009) and weakly supported by additional LF analyses in this study (Fig. 8a), led the authors to conclude that the trend towards lighter $\delta^{18}\text{O}_{\text{ol}}$ values found in NVL basalts is the result of cannibalization of altered volcanic rocks. To more fully assess the possible effects of assimilation we have selected, in addition to NVL crustal rocks, an altered mugearite lava from Mount Sidley, Marie Byrd Land, which has a very low $\delta^{18}\text{O}$ whole-rock value of 1.8‰: a result of alteration by highly ^{18}O -depleted Antarctic meteoric water (Panter *et al.*, 1997). The interaction between basalts and potential contaminants is evaluated on a plot of $\delta^{18}\text{O}_{\text{ol}}$ versus whole-rock Sr concentration shown in Fig. 12. The trend in $\delta^{18}\text{O}_{\text{ol}}$ of the alkali basalts with longitude (Fig. 10i) and the strong correlation with Sr concentration (Fig. 12) may be explained by (1) AFC involving ‘normal’ to slightly ^{18}O -enriched basaltic magma interacting with low $\delta^{18}\text{O}$ volcanic rocks and the contamination increasing oceanward, (2) mixing between low $\delta^{18}\text{O}$ ($< 5\%$) basaltic magma and mafic crust (e.g. gabbro, $\delta^{18}\text{O} \sim 7\%$) with the proportion of crust increasing continentward, or (3) reaction between low $\delta^{18}\text{O}$ melt and peridotite (e.g. $\text{Opx} + \text{Liq}_0 \leftrightarrow \text{Ol} + \text{Liq}_1$; Yaxley & Green, 1998; Pilet *et al.*, 2008; Lambart *et al.*, 2012) that is enhanced continentward as melt migrates through thicker mantle lithosphere. The first scenario (cannibalization) is difficult to defend given the trend of the alkali basalts towards lower $^{87}\text{Sr}/^{86}\text{Sr}$ and higher $^{143}\text{Nd}/^{144}\text{Nd}$ ratios oceanward (Fig. 10g and h). The Sr and Nd isotopic ratios should remain relatively constant if the contaminant was altered by Antarctic meteoric water. If the low $\delta^{18}\text{O}$ signature of the contaminant was a result of alteration by seawater at high temperatures ($\geq 250^\circ\text{C}$; Muehlenbachs, 1986; Gao *et al.*, 2012) it would also possess an elevated Sr isotope signature, and therefore assimilation would lead to a magma that has higher $^{87}\text{Sr}/^{86}\text{Sr}$ along with a low $\delta^{18}\text{O}$ value, which is not the case here. Simple mixing provides a better fit for the geochemical and isotopic trends exhibited by the alkali basalts (Figs 11 and 12) but again requires a significant proportion of mafic crust (i.e. gabbro/eclogite) and a source for low $\delta^{18}\text{O}$ magma. There is a general positive correlation between $\delta^{18}\text{O}_{\text{ol}}$ and Sr concentration for basanite, hawaiiite and tephrite lavas, which can be mostly enveloped by AFC model curves constructed based on the interaction between a low- ^{18}O magma (e.g. NV-4C) and gabbroic crust, but only if the proportion of assimilation to crystal fractionation is allowed to vary significantly ($r \sim 1$ to 0.3; Fig. 12). In addition, the

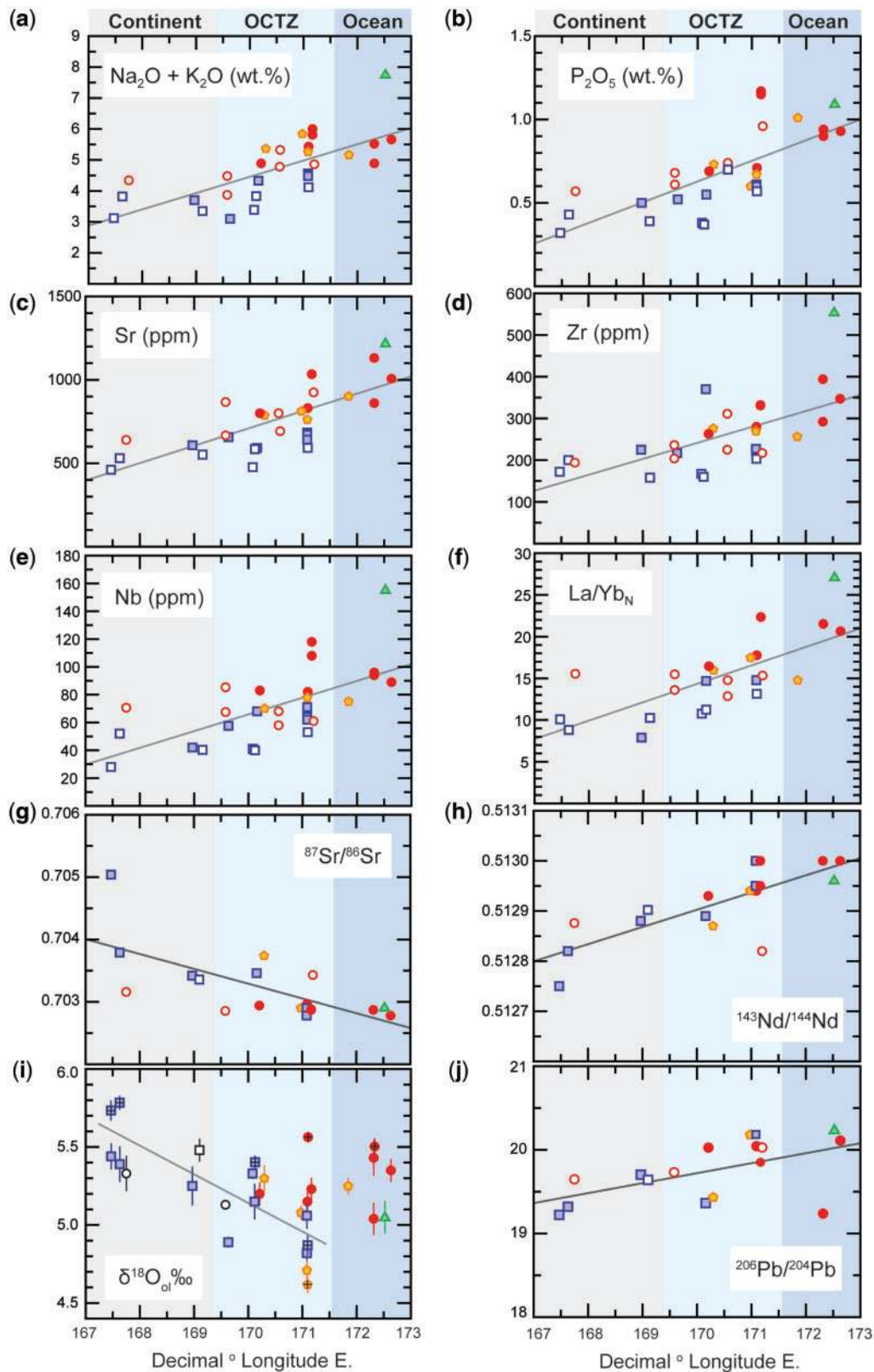


Fig. 10. Variation in major and trace elements and measured Sr–Nd–Pb–O isotopes with decimal degree longitude for NWRS basalts. References, symbols and data criteria are the same as in Fig. 3, and for oxygen isotopes, Fig. 8. The geographical location of each sample is shown in Fig. 1b. Ocean and continental sectors are defined in Fig. 1b and the ocean to continent transition zone (OCTZ) is demarcated as the region between the base of the continental shelf (~1500 mbsl) and the inferred boundary between the East Antarctica craton and extended lithosphere comprising the WARS (bold dashed line in Fig. 1b). Lines of regression, which include all data, have r^2 that range from 0.4 to 0.6 and Spearman rank correlation coefficients that range from 0.6 to 0.8. For $\delta^{18}\text{O}_{\text{ol}}$ only alkali basalt is regressed. Oxygen values are SIMS analyses except for three NWRS samples (open symbols) measured by LF from Nardini *et al.* (2009). Error bars represent the standard error of the mean (SEM). Sample La/Yb ratios are normalized to primitive mantle (Sun & McDonough, 1989).

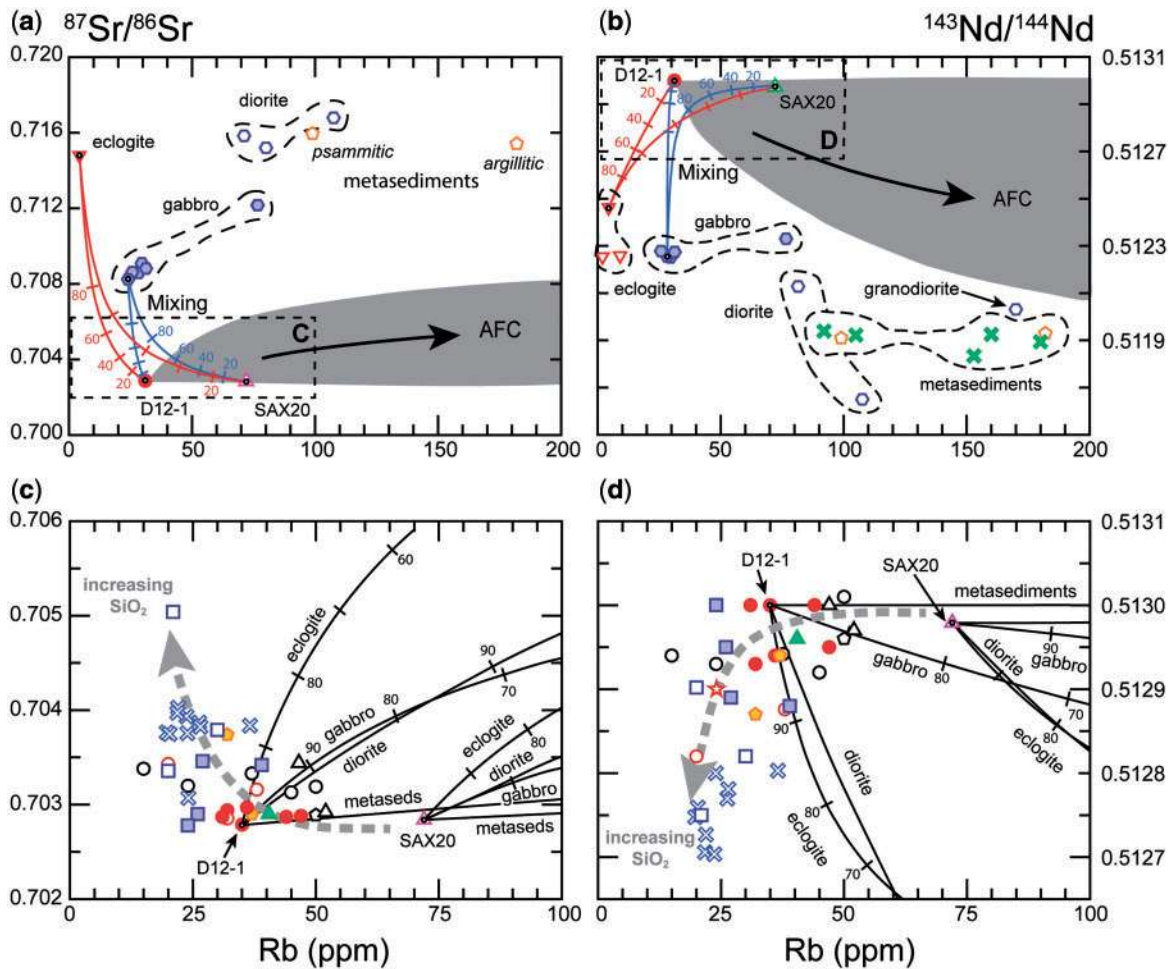


Fig. 11. Measured Sr and Nd isotopic compositions vs Rb concentrations (ppm). (a, b) Selected basalt and crustal rock compositions used for mixing (Langmuir *et al.*, 1977) and assimilation–fractional crystallization (AFC; DePaolo, 1981) models. Basalt sample D12-1 was chosen to be representative of a parental magma composition based on its oceanic location and relatively unfractionated composition ($\text{MgO} = 10.7 \text{ wt } \%$, $\text{Cr} = 355 \text{ ppm}$, $\text{Ni} = 205 \text{ ppm}$; Table 2). Also selected is sample SAX20 (Table 2), which is overall the most incompatible element enriched sample (Fig. 6) and has been equated to a primary (metasomatic) melt by Coltorti *et al.* (2004) and Perinelli *et al.* (2006). Crustal rocks from the NVL consist of gabbro, diorite and granodiorite (Di Vincenzo & Rocchi, 1999; Dallai *et al.*, 2003), metasediment (Henjes-Kunst & Schussler, 2003; Di Vincenzo *et al.*, 2014) and eclogite (Di Vincenzo *et al.*, 1997; Ghiribelli, 2000). Gray fields encompass AFC model curves [shown in detail in (c) and (d)] using $D_{\text{Rb}} = 0.01$, $D_{\text{Sr}} = 0.1$, $D_{\text{Nd}} = 0.4$ and proportion of assimilation to crystallization ($r = 0.8$). Mixing curves between basalt, eclogite and gabbro are also shown. Numbered tick marks are the percentage of crust in each mixture. (c, d) Detail showing AFC model curves using basalts D12-1 (Table 2) and SAX20 (Nardini *et al.*, 2009) and different contaminants (eclogite is sample G3; gabbro is DR13 and AC6; diorite is sample AF16; metasediment is argillitic). Numbers along each curve represents the fraction of liquid remaining (F). Gray dashed arrow shows the trend of increasing SiO_2 (wt %) in basalt samples. References, symbols and data criteria for the basalts are the same as those given in Fig. 3.

lower Sr concentrations in alkali basalts relative to basanite and tephrite cannot be explained by these models.

In summary, processes involving shallow-level contamination by crust do not adequately account for the variation in major and trace elements and isotopes shown by the NWRS basalts. Furthermore, none of the scenarios discussed above are able to emulate the well-defined trends in major and trace elements and isotopes between land and sea (Fig. 10). Consequently, the third scenario, which discounts the involvement of crust altogether, will be evaluated along with melting processes and mantle source(s) in the following section.

Mantle sources

The wide range in $\delta^{18}\text{O}_{\text{OI}}$ exhibited by NWRS basalts (variation of $\sim 1.5\text{‰}$; Fig. 8a) is comparable with the range observed in OIB, which has been explained by mantle source heterogeneity; a result of variably altered, recycled oceanic crust (\pm sediments) within the convecting mantle (Eiler *et al.*, 1996; Eiler, 2001; Day *et al.*, 2010; Gurenko *et al.*, 2011). A recent comprehensive review of petrological and geochemical constraints on the origin of mafic alkaline rocks (primarily OIB) has been provided by Pilet (2015) and details how the direct melting of pyroxenite (recycled upper or lower oceanic crust = MORB or gabbro, respectively), with or without added sediment, cannot reproduce the major element

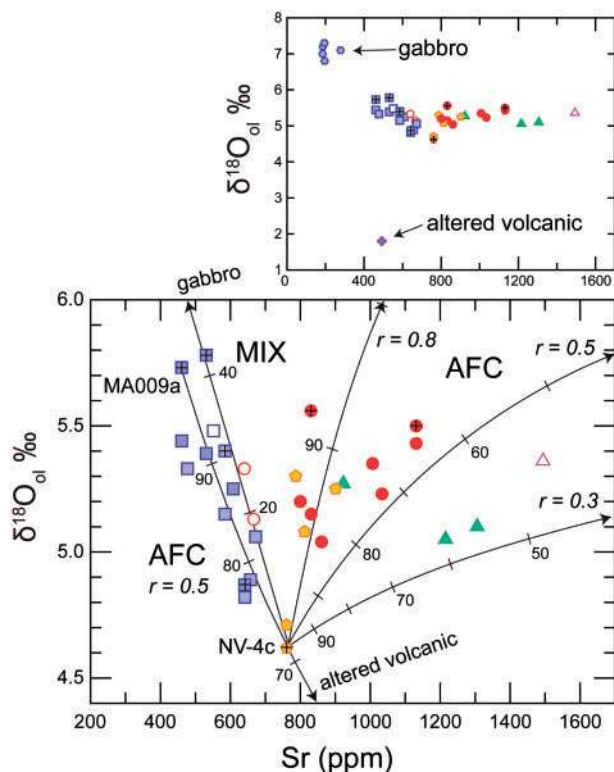


Fig. 12. Variations in $\delta^{18}\text{O}_{\text{ol}}$ with whole-rock Sr concentrations for NWRS basalts modeled by AFC using an altered basaltic composition (mugearite MB32.11; Panter *et al.*, 1997) and mixing and AFC using gabbro from NVL (Di Vincenzo & Rocchi, 1999; Dallai *et al.*, 2003). Sample MA009a was selected to represent a slightly ^{18}O -enriched basaltic magma and sample NV-4c was selected to represent a low $\delta^{18}\text{O}$ basaltic magma (Tables 2 and 3). AFC models use $D_{\text{Sr}} = 0.1$, oxygen isotope bulk mineral–melt fractionation = 0.4‰ (Eiler, 2001), and the proportion of assimilation to crystallization (r) = 0.8, 0.5 and 0.3. Numbered tick marks on AFC curves represent the amount of liquid remaining and tick marks on the mixing curve represent the proportion of gabbro in the mixture. All but two of the basalts have $\text{MgO} > 6\text{ wt } \%$ (Table 3) and the symbols used are the same as in Fig. 8. The method for mixing and AFC are the same as in Fig. 11.

compositions of low-silica alkaline basalts, which include basanite, tephrite and nephelinite (Fig. 3). The melting experiments for silica-deficient pyroxenite in the presence of CO_2 (Dasgupta, 2006; Gerbode & Dasgupta, 2010), however, can produce liquids that are closer in SiO_2 and total alkalis content but have $\text{Al}_2\text{O}_3/\text{TiO}_2$ and $\text{Na}_2\text{O}/\text{K}_2\text{O}$ ratios that vary significantly, which is in contrast to the relatively low and constant ratios observed in natural low-silica alkaline basalts (Pilet, 2015), including basalts from the NWRS (5.05 ± 1.06 and 2.75 ± 0.47 , respectively). Therefore, to account for the trace element and radiogenic isotope signatures in mafic alkaline rocks, which are ultimately attributed to recycled materials, a pyroxenitic melt must be further conditioned and homogenized before it reaches the surface. Pilet (2015) described three possible scenarios for this: (1) pyroxenite melt infiltrates and enriches (metasomatizes) peridotite in the asthenosphere, which is then melted at low degrees ($\sim 1\text{--}5\%$) in the presence of

CO_2 (Dasgupta & Hirschman, 2007); (2) pyroxenite melt reacts with peridotite (dissolution/precipitation reaction = olivine + liquid \leftrightarrow orthopyroxene + liquid; precipitation of either orthopyroxene or olivine may also include clinopyroxene and garnet) under dry conditions (Lambart *et al.*, 2012; Mallik & Dasgupta, 2014) or in the presence of CO_2 (Mallik & Dasgupta, 2014) prior to reaching the surface; (3) a multi-stage process that begins with a low-degree melt from the asthenosphere that penetrates and forms amphibole-bearing cumulates within the lithospheric mantle. Later melting of these relatively small-volume, trace element and volatile-rich cumulates (metasomatic veins) at high degrees, and reaction of this liquid [as in (2)] with the surrounding mantle on its way to the surface, can reproduce the major and trace element characteristics of the mafic alkaline magma (Pilet *et al.*, 2008).

The third source type, metasomatized lithosphere, has also been proposed to explain the petrogenesis of alkaline basalts erupted in continental settings (Stein *et al.*, 1997; Jung *et al.*, 2005; Panter *et al.*, 2006; Ma *et al.*, 2011; Mayer *et al.*, 2014; Rooney *et al.*, 2014, 2017) including those within the WARS (Rocchi *et al.*, 2002; Panter *et al.*, 2003; Nardini *et al.*, 2009; Perinelli *et al.*, 2011; Martin *et al.*, 2013; Aviado *et al.*, 2015). In the continental NVL, Perinelli *et al.* (2011) considered the variability in olivine oxygen isotope data for mantle cumulate xenoliths ($5.00\text{--}5.72\text{‰}$), together with olivine from alkaline basalts ($4.92\text{--}5.53\text{‰}$; Nardini *et al.*, 2009) and peridotites ($4.80\text{--}5.81\text{‰}$; Perinelli *et al.*, 2006) to signify extensive ^{18}O compositional heterogeneity in the lithospheric mantle. Our new $\delta^{18}\text{O}_{\text{ol}}$ values collected from continental and oceanic NWRS basalts extend that range ($4.44\text{--}5.92\text{‰}$; Fig. 8a). Perinelli *et al.* (2011) concluded that mantle cumulates were modally and cryptically metasomatized by low $\delta^{18}\text{O}$ melts, which in turn originated by the melting of earlier formed metasomes emplaced within the continental lithosphere during rifting in the Late Cretaceous. The ultimate origin of the low $\delta^{18}\text{O}$ mantle signature found in NVL and the NWRS will be discussed below.

The major element compositions of continental and oceanic basalts from West Antarctica reported in this study are consistent with their being derived from mantle sources that are predominantly silica-undersaturated and contain amphibole-rich lithologies (Fig. 13) and align with the metasomatized lithospheric hypothesis. The presence of amphibole in the source is also supported by negative K anomalies and high Nb–Ta contents displayed on multi-element, primitive mantle-normalized patterns (Fig. 6). Potassium occurs in stoichiometric proportions in the mantle minerals amphibole (pargasite, kaersutite) and mica (phlogopite). If these minerals are not completely consumed during mantle partial melting, then K will be retained in the source and the melt will be depleted in K relative to neighboring trace elements (e.g. Nb, Ta, La and Ce), which will behave incompatibly (LaTourrette *et al.*, 1995; Ionov *et al.*, 2002; Tiepolo *et al.*, 2007, and

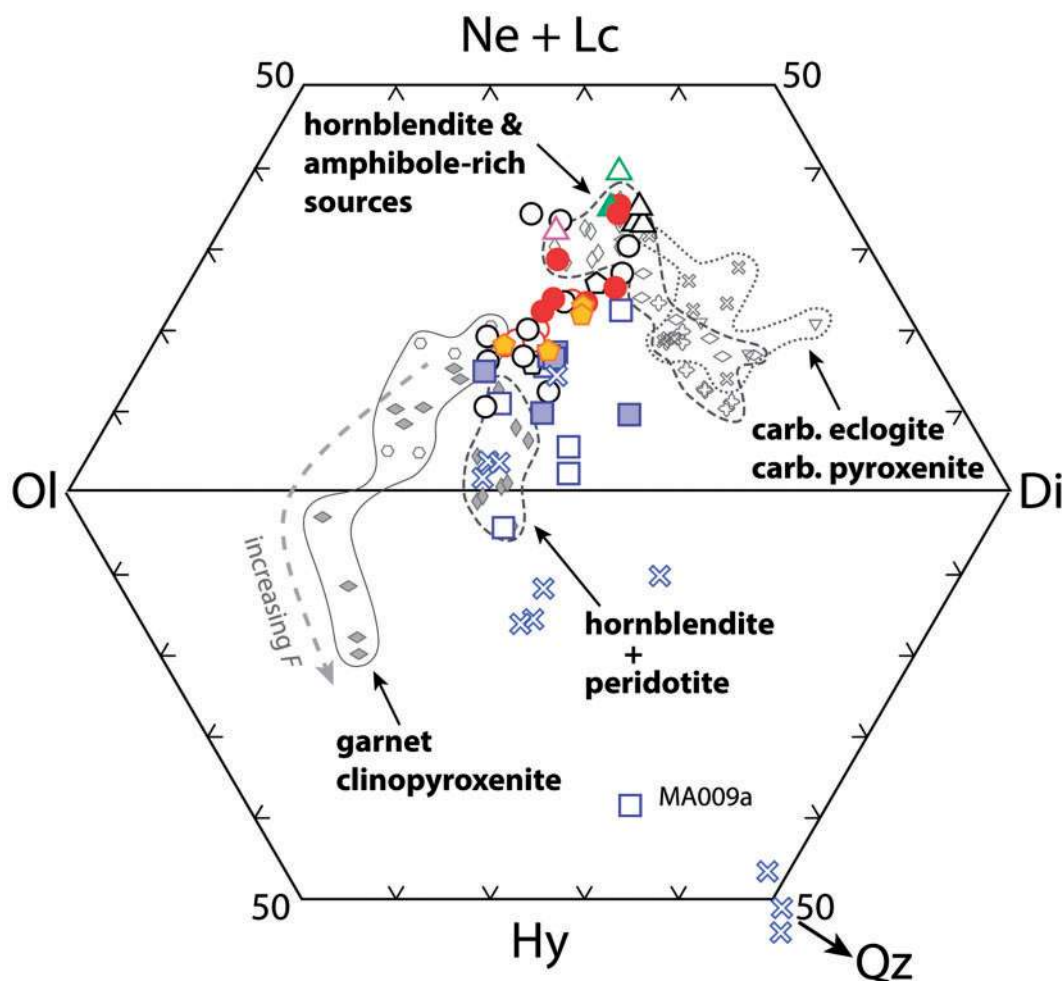


Fig. 13. Plot of normalized (CIPW) compositions calculated from whole-rock major element data. Silica-undersaturated compositions plot within the OI–Ne + Lc–Di triangle (truncated at 50 wt % Ne + Lc) and silica-saturated compositions plot within the OI–Hy–Di triangle (up to 50 wt % Hy). Symbols and data criteria are the same as in previous figures. Fields for basaltic compositions derived from melting experiments include carbonated pyroxenite (2.9 GPa, 1275–1475°C; Gerbode & Dasgupta, 2010), carbonated eclogite (3.5 GPa, 1250–1400°C; Kiseeva *et al.*, 2012), hornblende (1.5 GPa, 1150–1350°C; Pilet *et al.*, 2008), clinopyroxene hornblende (1 GPa, 1250–1400°C; Pilet *et al.*, 2008), amphibole wehrlite (1.0 GPa, 1225–1350°C; Médard *et al.*, 2006), garnet clinopyroxenite (2–2.5 GPa, 1340–1500°C; Hirschmann *et al.*, 2003; Keshav *et al.*, 2004). Also included is melt derived from hornblende plus peridotite sandwich experiments (1.5 GPa, 1225–1325°C; Pilet *et al.*, 2008). Dashed gray arrow represents increasing proportion of melt fraction (*F*) determined for garnet clinopyroxenite in experiments by Keshav *et al.* (2004).

references therein). High Nb and Ta concentrations ($\geq 100 \times$ primitive mantle; Sun & McDonough, 1989) have been measured on vein amphibole in peridotite (Ionov & Hofmann, 1995; Ionov *et al.*, 2002) and for both vein and disseminated amphibole found in peridotite from NVL (Coltorti *et al.*, 2004; Perinelli *et al.*, 2006). Niobium enrichment of the lithospheric mantle has also been related to metasomatism by carbonatite, which can have concentrations $> 200\text{--}1000 \times$ primitive mantle (Pfänder *et al.*, 2012, and references therein). Martin *et al.* (2013) ascribed variations in minor and trace element ratios (e.g. elevated Nb/Ta as established by Pfänder *et al.*, 2012) to signify carbonate metasomatism in the lithospheric mantle sources of alkaline basaltic rocks from Mount Morning in Southern Victoria Land (SVL, Fig. 1a). This is also consistent with the Nb/Ta ratio (39) measured on mantle phlogopite from Mount

Morning, which is close to the global average for carbonatites (35; Chakhmouradian, 2006), as well as having a Nb concentration (547 ppm) that is mostly higher than phlogopite (and amphibole) from mantle xenoliths that have been attributed to mantle lithosphere enriched by carbonate-rich silicate liquids (Ionov & Hofmann, 1995; Ionov *et al.*, 2002). Experimental results indicate that carbonate phases can coexist with amphibole and phlogopite in spinel and garnet peridotite at high pressures (Brey *et al.*, 1983; Olafsson & Eggler, 1983). Sources with elevated Nb and Ta concentrations may also reside in rutile-bearing peridotite (Kalfoun *et al.*, 2002) and eclogite (Rudnick *et al.*, 2000; John *et al.*, 2004). An eclogitic contribution to the metasomatic enrichment of the sub-continental lithosphere beneath NVL has been proposed by Melchiorre *et al.* (2011) based on radiogenic values of Os and Hf isotopes

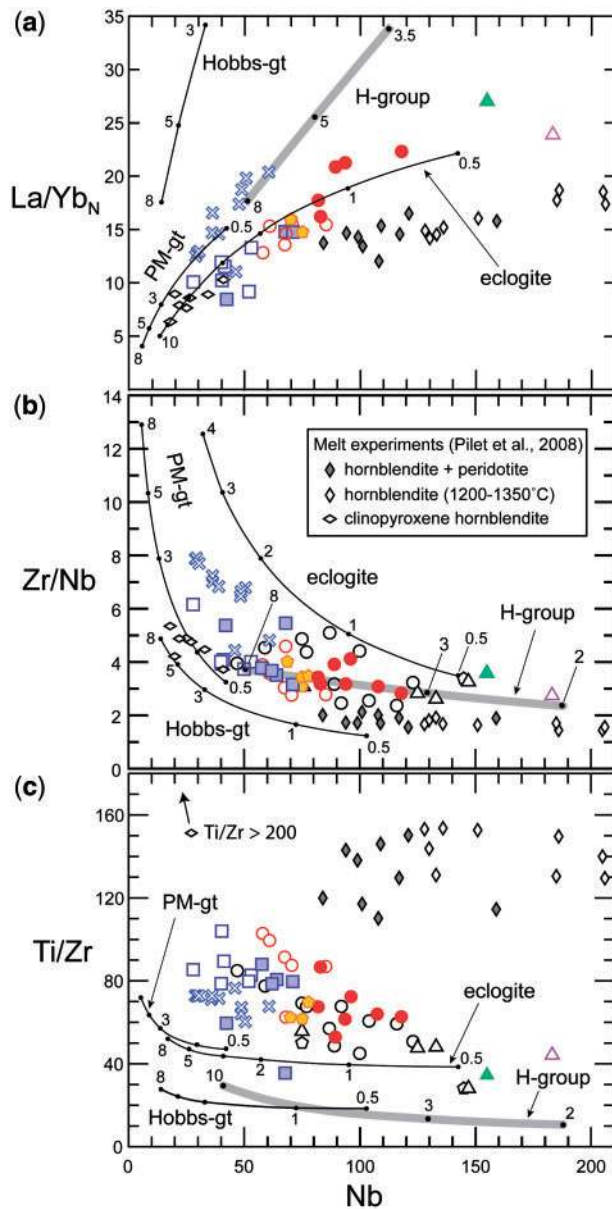


Fig. 14. La/Yb_N , Zr/Nb and Ti/Zr vs Nb (ppm). Basalts are compared with experimental melts by Pilet *et al.* (2008) on amphibole-bearing lithologies at 1.5 GPa and temperatures 1200–1400°C. La/Yb ratio is normalized to primitive mantle from Sun & McDonough (1989). Symbols and data criteria for the basalts are the same as those given in Fig. 3. Curves represent modal and non-modal batch melting using four different source compositions. Model batch melt of eclogite (see Pfänder *et al.*, 2007) uses an average eclogite composition (including Group III type) from John *et al.* (2004), source and melt mode of 0.80 clinopyroxene, 0.20 garnet, and partition coefficients from Pertermann *et al.* (2004; experiment A343). Non-modal batch melting of garnet lherzolite uses the source composition for primitive mantle (PM) from Hofmann (1988), excepting Nb concentration, which has been reset to 0.491 ppm (Münker *et al.*, 2003), and a source derived from Hobbs Coast basalts in Marie Byrd Land by Hart *et al.* (1997). Source mode and melt mode reactions follow Salters (1996) where the source mode is 0.53 olivine, 0.04 orthopyroxene, 0.38 clinopyroxene and 0.05 garnet, and the melt mode is 0.05 olivine, 0.49 orthopyroxene, 1.31 clinopyroxene and 0.13 garnet. Partition coefficients are from Pilet *et al.* (2011, and references therein). The fourth source is spinel peridotite that has experienced metasomatic enrichment (average ‘H-group’, high-potassium, phlogopite-

measured on sulfide and clinopyroxene (respectively) from amphibole-bearing and dry peridotite xenoliths.

Here we also emphasize that the radiogenic isotope signatures in mafic alkaline rocks are ultimately sourced from materials recycled by subduction. The trace element and Sr, Nd and Pb isotopic signatures of the alkaline rocks fall within the compositional range of OIB. The Sr, Nd and Pb isotopic composition of OIB, however, comes from recycled subducted materials (Hofmann, 2014; White, 2015, and references therein). Specifically, the Pb isotope compositions of some of the alkaline rocks are highly radiogenic, similar to HIMU OIB, whereas those of the bulk of the rocks are less radiogenic, akin to PREMA (or FOZO)-type OIB, which are also sometimes called young HIMU (Thirlwall, 1997; Stracke *et al.*, 2005). Although it is widely accepted that the highly radiogenic Pb signature of HIMU is due to recycling of variably altered basaltic crust (e.g. Hofmann, 2014; White, 2015, and references therein), a recycled marine carbonate source for the radiogenic Pb isotope composition of HIMU has recently been proposed (Castillo, 2015, 2016). This alternative proposal posits that recycled marine carbonates act as dirty Pb isotopic ‘spike’ that variably contaminates (i.e. from PREMA to HIMU) the mantle sources of OIB and other intraplate lavas. Additionally, the Nb–Ta enrichment but Pb depletion that are pervasive features of OIB (e.g. Hart & Gaetani, 2006; Jackson *et al.*, 2008; Hofmann, 2014; Peters & Day, 2014) is strongly complemented by the Nb–Ta depletion but Pb enrichment in subduction-related lavas (Castillo, 2015). Notably, the K depletion of the alkaline rocks is also an additional, distinctive feature of HIMU-type OIB (Castillo, 2015; Weiss *et al.*, 2016). Thus, we propose that a compositional connection exists between the mafic alkaline rocks and previously subducted carbonate-rich materials. This does not conflict with our proposal for metasomatized lithosphere given that the metasomatizing fluids that form the amphibole-rich metasomes are considered to be themselves derived from melting of a sublithospheric source containing recycled subducted materials (discussed below).

Mantle melting

The variation in major and trace elements and isotopes displayed by NWRS basalts in Fig. 10 has been suggested to be the result of the tapping of a heterogeneous, metasomatically enriched, mantle lithosphere at

bearing) from Hartmann & Wedepohl (1990) with source and melt mode reactions and partition coefficients from Pfänder *et al.* (2012, and references therein). Titanium is compatible in phlogopite ($K_D^{\text{phl/melt}} = 3$, Pilet *et al.*, 2011, and references therein) and therefore non-modal batch melting of phlogopite-bearing peridotite (H-group) in (c) was modeled using a source mode of 0.55 olivine, 0.22 orthopyroxene, 0.15 clinopyroxene, 0.03 spinel, 0.05 phlogopite and a melt mode of 0.05:0.05:0.65:0.05:0.2, respectively (see Ersoy *et al.*, 2010). Numbers along the curves represent the degrees of melting in per cent.

progressively smaller melt fractions oceanward (Panter *et al.*, 2011). In Fig. 14, basalts from the NWRS along with the other oceanic WARS basalts highlighted in this study are compared with model curves for modal and non-modal batch melting that involve three potential mantle sources that are relevant to what has been discussed above. They include a mantle composition calculated as the source of the basaltic volcanism erupted near the Hobbs Coast in Marie Byrd Land (Hart *et al.*, 1997), an average of Zambian eclogites interpreted to represent fossil subducted slab material (John *et al.*, 2004) and an average composition for metasomatized (high-K, phlogopite-bearing) spinel peridotite xenoliths from NW Germany (H-group; Hartmann & Wedepohl, 1990). Melting of a primitive mantle (PM) composition (Hofmann, 1988) is also shown. Additionally, for comparison, the results of high-pressure and high-temperature melting experiments on natural hornblende and clinopyroxene hornblende from Pilet *et al.* (2008) are plotted.

Models for PM, Hobbs and H-group sources produce steeper positive slopes with decreasing melt fractions in Nb versus La/Yb_N relative to the data arrays for basalt and melting experiments (Fig. 14a), whereas eclogite provides a very good fit to the data. In Nb versus Zr/Nb (Fig. 14b), melting of metasomatized peridotite (H-group) provides the best fit, but eclogite is also reasonable at low melt fractions. All four models produce low Ti/Zr ratios (Fig. 14c), but at lower melt fractions (1–3%) ratios for eclogite are similar to those of the basalts. In general, the results demonstrate that the overall trend of increasing Nb concentration from alkali basalt to basanite to tephrite could be explained by melting to a smaller degree of an enriched mantle source, which in the case of the NWRS occurs oceanward, as indicated by the more common occurrence of strongly silica-undersaturated compositions (i.e. basanite and tephrite) away from the continent (Figs 1b and 10).

There are two fundamental short-falls with this hypothesis. First is the difficulty in matching compositions (both major and trace elements) derived by low-degree melting of eclogitic and peridotitic sources to those of low-Si alkaline basalts (< 45 wt % SiO₂) as emphasized by Pilet (2015). Although models of low degrees of melting (≤ 3%) of eclogite produce similar high field strength element (HFSE; e.g. Nb, Zr, Ti) concentrations, they also generate significantly higher large ion lithophile element (LILE; e.g. Rb, Ba, and K) and Pb concentrations and lower HREE (Yb and Lu) and Y concentrations compared with the basalts. The melting of metasomatized peridotite (H-group) yields a better match for LILE and HFSE, but the Ti concentrations produced are too low (< 1 wt %) relative to the basalts (2.0–4.8 wt %, Table 2) and thus give much lower Ti/Zr ratios (Fig. 14c). Second is the difficulty in explaining the systematic variation in major and trace elements of the NWRS basalts across the continent to ocean transition (Fig. 10) by changes in the degree of partial melting. This is problematic as the lithospheric thickness across

the continent to ocean boundary differs substantially. Estimates of crustal thicknesses predict Moho depths beneath the eastern flank of Transantarctic Mountains to be between 25 and 35 km (Behrendt, 1999; Salimbeni *et al.*, 2010) and in the Northern Basin (Fig. 1) between 20 and 15 km (Busetti *et al.*, 1999). A Moho depth of 5–6 km is estimated at the shelf break between the Northern Basin and the Adare Basin (Selvans *et al.*, 2014) and that depth extends north into the Adare Trough (Müller *et al.*, 2005; Selvans *et al.*, 2014). The depth to the base of the lithosphere is broadly resolved through regional tomographic studies that indicate thicknesses of > 150 km beneath the East Antarctic craton, 100–70 km within the West Antarctic rift and < 80 km beneath oceanic lithosphere (Danesi & Morelli, 2001; Ritzwoller *et al.*, 2001; Heeszel *et al.*, 2016). If mantle source compositions and mantle potential temperatures near the base of the lithosphere are similar across the region, then partial melting should occur at much shallower depths beneath the Adare Basin relative to the continent. This scenario would result in higher degrees of partial melting away from the continent, which is contrary to the interpretation based solely on geochemistry.

The most Si-undersaturated and incompatible element enriched basalts (basanite and tephrite) in the NWRS were also interpreted by Panter *et al.* (2011) to represent small-degree melts that scavenged the most easily fusible material in the lithosphere (i.e. amphibole). Higher Nb/Y ratios in WARS basalts correlate with the higher values anticipated for melting of carbonated peridotite sources (Herzberg & Asimow, 2008) and the higher *Ne*+*Lc* normative contents, and are similar to experimental results from high-degree melting of hornblende (Figs 13 and 15a and b). As mentioned above, Nb can reach high concentrations in amphibole and in mantle that has experienced carbonatite metasomatism. Furthermore, the compatibility of Nb in amphibole is mostly less than unity whereas Y is compatible [$D^{\text{amph/melt}} = 0.53$ and 1.48, respectively; average values calculated by Pilet *et al.* (2011) using data from Tiepolo *et al.* (2000a, 2000b, 2007)]. Thus we interpret the higher Nb/Y ratios in basanite and tephrite as indicating greater contributions from amphibole-rich (± CO₂) metasomes within the lithospheric mantle. In the case of the NWRS, the signature becomes more prominent oceanward (Fig. 15c).

Melt genesis between ocean and continent

We propose that the geochemical signature of mafic alkaline basalts in the NWRS is a consequence of high-degree melting of amphibole-bearing metasomatic veins in both oceanic and continental lithosphere and that the progressive interaction of the melt with the surrounding mantle (see Pilet *et al.*, 2008), occurring to a greater extent continentward, provides the best explanation for the systematic, gradational (i.e. non-stepwise) variation in major and trace element and isotopic data

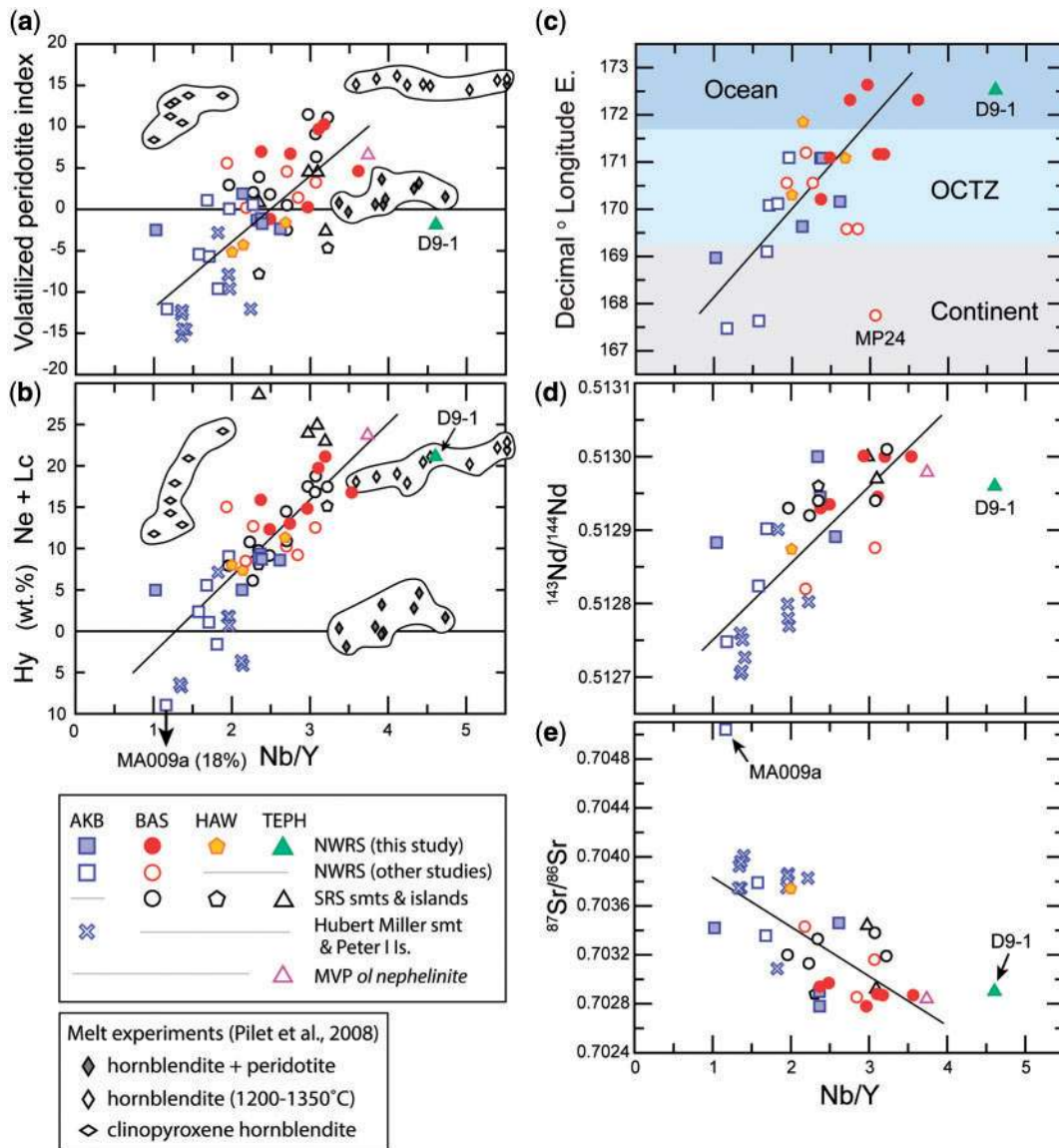


Fig. 15. Compositional parameters and geographical locations (NWRS) of basalts plotted vs Nb/Y ratios. Symbols and data criteria for the basalts are the same as those given in Fig. 3. (a) Volatilized peridotite index [= $\text{CaO} - (2.318\text{SiO}_2 - 93.626)$] defined by Herzberg & Asimow (2008) as a line on a CaO vs SiO₂ diagram that separates magmas derived from carbonated peridotite (Dasgupta *et al.*, 2007), values > 0, and magma derived from carbonate-free peridotite (Walter, 1998; Herzberg, 2004, 2006), values < 0. Experimental melts of amphibole-rich sources (Pilet *et al.*, 2008) are also shown. Line of regression excludes tephrite sample D9-1 (solid green triangle). (b) Normalized (CIPW) values of basalts and experimental melts. Line of regression excludes sample MA009a. (c) Longitude of NWRS basalts vs Nb/Y (refer to Fig. 8 for criteria for geographical sectors). Line of regression excludes tephrite D9-1 and a basanite from the continental sector (MP24, Nardini *et al.*, 2009). (d, e) Nd and Sr isotope compositions vs Nb/Y. Tephrite D9-1 is excluded from the regression in both plots and MA009a is also excluded in (e).

(Figs 10 and 15c). As briefly outlined above, the multi-step process to produce low-Si alkaline basalts proposed by Pilet *et al.* (2004, 2005, 2008, 2010, 2011) and Pilet (2015) requires lithospheric enrichment by small-degree melts from sub-lithospheric mantle sources, followed by high-degree melting of the resultant amphibole-rich metasomes, which in turn react with the surrounding peridotite during melt migration. There are several important aspects of the Pilet *et al.* model that need to be emphasized and aligned with what is being proposed here. First, their model demonstrates (theoretically and experimentally) that the major and trace

element composition of amphibole cumulates is not dependent on the composition of the underlying asthenosphere. The major element composition, including K and Ti, of amphibole-bearing cumulates is controlled by the stoichiometry of the minerals, whereas the trace element content is controlled mostly by the exchange equilibrium between minerals and liquid ($K_D^{\text{min/melt}}$). A second vital feature of their model is that unlike major and trace elements, the isotopic composition of the cumulate is inherited from the underlying asthenosphere. Therefore it is suggested that the isotopic signature of the most Si-undersaturated and incompatible element

enriched basalts with the highest Nb/Y ratios may best represent the composition of the sub-lithospheric source with low $^{87}\text{Sr}/^{86}\text{Sr}$ (≤ 0.7030), high $^{143}\text{Nd}/^{144}\text{Nd}$ (~ 0.5130) and high $^{206}\text{Pb}/^{204}\text{Pb}$ (≥ 20) (Figs 7, 10, 12 and 15d, e). This isotopic 'endmember' is characteristic of sources for Cenozoic alkaline magmas in West Antarctica, as well as alkaline basalts erupted on widely scattered continental fragments of East Gondwana (Zealandia and eastern Australia). As noted above, the signature has been deemed 'young HIMU' or more recently 'CarboHIMU' (McCoy-West *et al.*, 2016) to distinguish it from endmember HIMU from oceanic settings (e.g. St Helena) and plots within the DMM–PREMA field (Fig. 7) defined by Stracke (2012). Indeed, most researchers agree that the potential mantle sources for this diffuse alkaline magmatic province (DAMP; Finn *et al.*, 2005) reside in metasomatized continental lithospheric domains, although the timing and cause of metasomatism as well as the ultimate source of the isotopic signatures remain controversial (Rocchi *et al.*, 2002; Panter *et al.*, 2006; Timm *et al.*, 2010; Scott *et al.*, 2014; McCoy-West *et al.*, 2010, 2016; van der Meer *et al.*, 2017). The results presented here and by Kipf *et al.* (2013) confirm that PREMA (i.e. young HIMU or CarboHIMU) isotopic signatures are also present in basalts erupted through oceanic lithosphere.

As proposed earlier, the trace element and radiogenic isotopic signatures of PREMA and HIMU originate from previously subducted slab materials. Specifically, the endmember HIMU may owe its highly radiogenic Pb, low $^{87}\text{Sr}/^{86}\text{Sr}$, and distinctive trace element signatures to Archaean marine carbonates (Castillo, 2015, 2016; Weiss *et al.*, 2016). The variable and less radiogenic Pb plus slightly higher $^{87}\text{Sr}/^{86}\text{Sr}$ of PREMA, on the other hand, come from subducted lithospheric mantle that was carbonated, or 'spiked' by a lesser amount of Archaean or possibly younger marine carbonates. Notably, our proposal is consistent with recent results indicating that alkaline and carbonatitic rocks from the northern and eastern regions near the edges of the North China Craton acquire some of their distinctive compositional features from subducted marine carbonates (Chen *et al.*, 2016; Li *et al.*, 2017, and references therein). These regions are tectonically similar to WARS in that they were previous convergent margins.

In the NWRS, measured $^{87}\text{Sr}/^{86}\text{Sr}$ increases whereas $^{143}\text{Nd}/^{144}\text{Nd}$ and $^{206}\text{Pb}/^{204}\text{Pb}$ decrease in basalts erupted with decreasing distance from the continent (Fig. 10). The overall age of the volcanism also increases continentward; however, applying an age-correction for radiogenic in-growth cannot explain this variation (i.e. corrections are $< 5 \times 10^{-5}$ for all three isotopic systems). What is changing is the thickness and age of the lithosphere, both of which increase from the Adare Basin towards the East Antarctic craton. Additionally, as inferred from the correlation between isotopic and Nb/Y ratios (Fig. 15d and e), the basalts erupted closer to the continent are interpreted to have less contribution (i.e. lower Nb/Y ratios) from metasomes and thus their

isotopic compositions may be displaced from sub-lithospheric sources by acquisition of lithospheric mantle signatures. The longer residence time required for a melt, which is generated from amphibole-bearing veins near the base of the lithosphere, to migrate upward through progressively thicker and older lithospheric mantle will advance melt–peridotite reactions. Experimental studies show that the reaction between Si-undersaturated (i.e. Ne-normative) liquid and peridotite will cause dissolution of orthopyroxene and the liquid will become enriched in silica while crystallizing olivine (Shaw *et al.*, 1998; Shaw, 1999; Lundstrom *et al.*, 2000). Average olivine–liquid equilibrium temperatures calculated for the NWRS basalts (Krans, 2013) are $1244 \pm 40^\circ\text{C}$ for anhydrous conditions (Beattie, 1993), $1211 \pm 37^\circ\text{C}$ for hydrous conditions (Putirka *et al.*, 2007) and $1145 \pm 29^\circ\text{C}$ for CO_2 -rich conditions (Sisson & Grove, 1993), and do not vary systematically between continent and ocean. Layered hornblendite and peridotite melting experiments performed at 1.5–2.5 GPa and 1200–1325°C on natural samples by Pilet *et al.* (2008) demonstrate that this reaction will evolve liquids with lower alkalinity, TiO_2 , CaO, FeO and incompatible trace element contents. It will also produce slightly higher MgO and Al_2O_3 contents, while maintaining relatively constant $\text{K}_2\text{O}/\text{Na}_2\text{O}$ and $\text{Al}_2\text{O}_3/\text{TiO}_2$ ratios. These features are consistent with the major and trace element trends from nephelinite/basanite to alkali basalt (~ 41 – 50 wt % SiO_2 ; Fig. 3) that are documented in this study. Alternatively, increasing the degree of partial melting of a common mantle source has been used to explain this compositional continuum observed in both oceanic and continental lavas (Frey *et al.*, 1978; Caroff *et al.*, 1997; Beccaluva *et al.*, 2007; Bosch *et al.*, 2014). However, following the arguments that we have presented above, we consider the reaction of Si-undersaturated liquids (i.e. nephelinitic/basanitic) with surrounding peridotite in the lithosphere to be a more plausible explanation for the systematic geochemical and isotopic variation in the NWRS basalts from ocean to continent.

Further support for this assertion is provided by the olivine oxygen isotope data. It should be recalled that $\delta^{18}\text{O}_{\text{ol}}$ values for NWRS basalts are highly variable ($\Delta \sim 1.5\text{‰}$; Fig. 8a) and are not adequately explained by crustal contamination (Fig. 12). High $\delta^{18}\text{O}_{\text{ol}}$ values correlate with the lower Nb/Y ratios of corresponding whole-rock compositions (Fig. 16a) and trend towards mineral values for orthopyroxene separated from peridotite xenoliths hosted by NVL basalts (Perinelli *et al.*, 2006). The correlation is consistent with reaction between low $\delta^{18}\text{O}$ liquid generated by melting of amphibole-rich metasomes (i.e. high Nb/Y source) and peridotite, where dissolution of orthopyroxene and crystallization of olivine evolve the liquid towards more Si-saturated (Fig. 16b) and ^{18}O -enriched compositions. Moreover, variations in trace elements, including Th and La, with SiO_2 content (Fig. 16c and d) parallel the trends produced by the melting and reaction

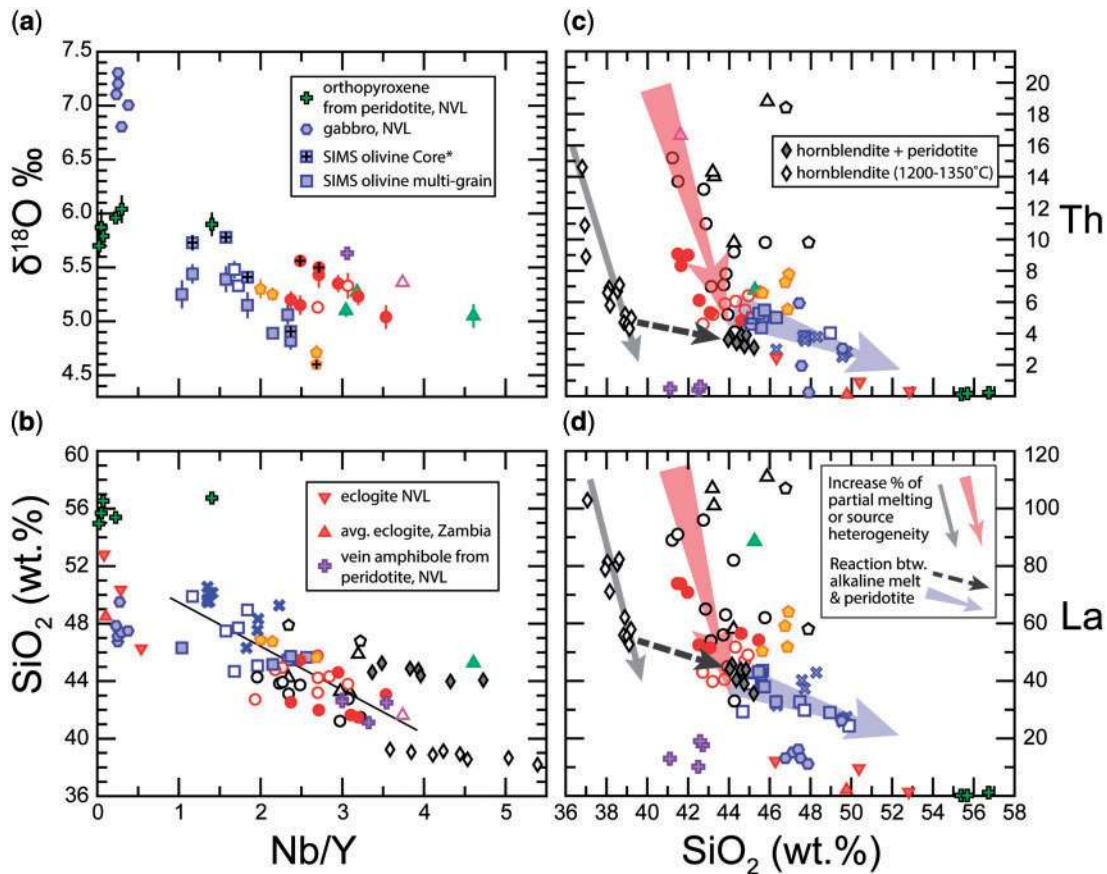


Fig. 16. (a) Nb/Y ratio vs $\delta^{18}\text{O}$ (‰). Oxygen isotopes for olivine phenocrysts from NWRS basalts were measured by LF and SIMS analysis (Table 3). Only samples with whole-rock MgO values greater than 6 wt % are plotted. Open symbols represent LF analyses of olivine from Nardini *et al.* (2009). In this study multiple grains of olivine in the same sample were analyzed by SIMS and averaged (solid colored symbols). Also shown are the average of multiple SIMS spot analyses (Core*) within the cores of individual olivine grains for several samples (symbols filled with cross). The Nb/Y ratios represent whole-rock values of the basalts that host the olivine. Orthopyroxene and vein amphibole $\delta^{18}\text{O}$ and Nb/Y ratios measured on peridotite xenoliths from NVL are from Perinelli *et al.* (2006). Whole-rock gabbro values provided by Dallai *et al.* (2003) for rocks from NVL. Error bars represent standard error of mean (SEM). (b) SiO_2 (wt %) vs Nb/Y ratios (symbols and data criteria of basalts are the same as in Fig. 3) are compared with the mineral chemistry of orthopyroxene and amphibole from peridotite xenoliths hosted in alkaline basalts from NVL (Coltorti *et al.*, 2004; Perinelli *et al.*, 2006). Whole-rock eclogite from NVL provided by Di Vincenzo *et al.* (1997) and average eclogite composition for whole-rocks from Zambia are from John *et al.* (2004). Line of regression ($r^2 = 0.52$, Spearman rank = 0.68) for Antarctic basalts excludes sample D9-1 (solid green triangle). SiO_2 (wt %) vs Th (c) and La (d) ppm of basalts are compared with natural peridotite, eclogite and gabbro as in (b), along with results of melting experiments conducted by Pilet *et al.* (2008). The experimental data are interpreted to represent changes in degree of partial melting or source heterogeneity (solid gray arrow) and reaction between basaltic melt and peridotite (dashed black arrow). These trends are emulated by basanite and tephrite/nephelinite (red arrow) and alkali basalt (blue arrow) in this study.

experiments of Pilet *et al.* (2008), providing additional support for this hypothesis.

An alternative explanation, however, is that the trends may be a result of mixing between Si-undersaturated melt and a liquid generated by the partial melting of recycled pyroxenite (pyroxene + garnet). Mixing proportions require >20–80% of gabbro/eclogite to account for the compositional range of the basalts (Figs 11, 12 and 16a, b). Based on experimental and thermodynamic constraints, partial melting of volatile-free pyroxenite cannot explain the major element compositions of the low- SiO_2 alkaline basalts (Lambart *et al.*, 2013; Pilet, 2015, and references therein), although homogenization with volatile-rich Si-undersaturated melt may have some merit. Even so, a model

for mixing must be able to emulate the systematic geochemical variation from land to sea in the NWRS, which would require the proportion of pyroxenite to increase towards the continent. Here again we favor the melt-peridotite reaction scenario in that it is better constrained by the evidence and provides a much more straightforward model (compare Occam's razor) for NWRS volcanism, yet some contribution from recycled pyroxenite may be warranted. Melchiorre *et al.* (2011) called upon the melting of a sub-lithospheric source containing between 15 and 60% eclogite to explain the radiogenic Os and Hf isotope values measured in metasomatized peridotite xenoliths from the NVL. Evidence from xenoliths, seismic and geodynamic investigations indicate that recycled volatiles and eclogitic material

are likely to have been introduced into the sublithospheric mantle beneath West Antarctica during Paleozoic–Mesozoic Gondwana subduction (Finn *et al.*, 2005; Sutherland *et al.*, 2010; Melchiorre *et al.*, 2011; Emry *et al.*, 2015; Martin *et al.*, 2015; Broadley *et al.*, 2016).

Subduction-related agents in metasomes

The lower oxygen isotope values measured on olivine ($\delta^{18}\text{O} \leq 5\text{‰}$) in the NWRS basalts are most probably a signature derived from hydrothermally altered subducted materials. Metasomatism of the NVL lithosphere by seawater-derived volatiles is indicated by heavy halogen (Br, I) and noble gas (Ar, Kr, Xe) compositions liberated from fluid inclusions in olivine and pyroxene in peridotite xenoliths (Broadley *et al.*, 2016). Broadley *et al.* (2016) suggested that the volatiles were released, possibly at depths up to 200 km (Sumino *et al.*, 2010; Kendrick *et al.*, 2013), during subduction and were incorporated into the overlying mantle wedge and subcontinental lithospheric mantle beneath the Gondwana continental arc during the Paleozoic. Their investigation along with those of Coltorti *et al.* (2004), Perinelli *et al.* (2006, 2011) and Melchiorre *et al.* (2011) provide strong support for metasomatism of the lithosphere by subduction zone processes and contributions from recycled subducted material to the source of the alkaline magmas in the NVL, including the NWRS.

Mafic eclogites formed by past subduction of oceanic lithosphere have highly variable oxygen isotopic compositions that range from extremely heavy ($\delta^{18}\text{O} > +10\text{‰}$) to extremely light ($\delta^{18}\text{O} < -10\text{‰}$) values for mineral and whole-rock samples (Zheng *et al.*, 1998, 2003; Putlitz *et al.*, 2000; Früh-Green *et al.*, 2001). The variability of $\delta^{18}\text{O}$ is explained by the exchange between fluids (meteoric or seawater $\delta^{18}\text{O} \leq 0\text{‰}$) and rock ($\delta^{18}\text{O}_{\text{basalt/gabbro/peridotite}} > 5\text{--}7\text{‰}$) over a wide range of temperatures and fluid/rock ratios in low- to high-pressure environments during the subduction cycle. Generally, lower temperature hydrothermal alteration within the upper oceanic crust will enrich rocks in $^{18}\text{O}/^{16}\text{O}$ whereas higher temperature ($\geq 250^\circ\text{C}$) exchange within the lower crust and upper mantle will deplete rocks in $^{18}\text{O}/^{16}\text{O}$ (Muehlenbachs, 1986). Low oxygen isotope values ($\delta^{18}\text{O} \leq 5\text{‰}$) measured on whole-rocks and clinopyroxene in veins and eclogitized metabasalt from the Erro–Tobbio peridotite, Italian Alps, were explained by Früh-Green *et al.* (2001) to be a consequence of high-temperature alteration of lower oceanic crust and upper mantle by seawater that has been preserved (i.e. lack of oxygen isotopic re-equilibration with ambient mantle) through eclogitization and limited fluid circulation within a relatively closed system at high pressures (≥ 2 GPa).

In HIMU ocean island basalts, low oxygen values ($\delta^{18}\text{O}_{\text{ol}} 4.7\text{--}5.2\text{‰}$) are also interpreted to be a consequence of long-term recycling of subducted materials (Eiler *et al.*, 1996; Eiler, 2001). Day *et al.* (2010) called

upon partial melting of metasomatized mantle peridotite that contains $\sim 10\%$ recycled pyroxenite/eclogite, itself a product of high-temperature alteration of oceanic crust and mantle, to account for the correlation between low $\delta^{18}\text{O}_{\text{ol}}$ ($4.87 \pm 0.18\text{‰}$) and high $^{206}\text{Pb}/^{204}\text{Pb}$ (values up to ≥ 20) in basalts from La Palma, Canary Islands. $\delta^{18}\text{O}_{\text{ol}}$ values for NWRS basalt display a weak correlation with $^{206}\text{Pb}/^{204}\text{Pb}$, as well as Sr and Nd isotopes (Fig. 9) and indicate that the low $\delta^{18}\text{O}$ signature is associated with the low $^{87}\text{Sr}/^{86}\text{Sr}$, high $^{143}\text{Nd}/^{144}\text{Nd}$ and high $^{206}\text{Pb}/^{204}\text{Pb}$. As discussed above, the origin of radiogenic Pb signatures (> 19.5) in mafic alkaline rocks found throughout West Antarctica and continental fragments of Gondwana (DAMP; Finn *et al.*, 2005) is controversial and has been related to both lithospheric and sublithospheric sources. The highest $^{206}\text{Pb}/^{204}\text{Pb}$ ratios (> 20.7) measured in mafic alkaline rocks are from continental basalts in Marie Byrd Land and Chatham Island (Panter *et al.*, 2000, 2006) and values greater than 21 have been measured on spinel peridotite xenoliths from Chatham Island and the Waitaha domain of southern New Zealand (McCoy-West *et al.*, 2016). For basalts within the NWRS the highest $^{206}\text{Pb}/^{204}\text{Pb}$ ratios (> 20) occur oceanward (Fig. 10) and, as discussed above, we consider that this signature, along with radiogenic Nd and depleted Sr and O isotopic values, was 'originally' derived from recycled crustal materials and transferred by small-degree melts to the lithosphere and stored in amphibole-rich cumulates (i.e. metasomes). The higher $^{206}\text{Pb}/^{204}\text{Pb}$ ratios found in some continental basalts and xenoliths scattered across the DAMP may be explained by compositional heterogeneity of the recycled material in the sub-lithospheric mantle, melting of higher proportions of the recycled material (see Day *et al.*, 2010), and/or may be due to rapid in-growth facilitated by high U/Pb ratios (McCoy-West *et al.*, 2016). The fractionation required to produce high U/Pb has been explained by compatibility differences between these elements during carbonatite metasomatism (McCoy-West *et al.*, 2016) or during post-metasomatic partial dehydration (Panter *et al.*, 2006).

Importantly, the fractionation of oxygen isotopes ($^{18}\text{O}/^{16}\text{O}$) between silicate liquids and silicate minerals at asthenospheric temperatures ($\geq 1350^\circ\text{C}$) or temperatures in the lithospheric mantle [$> 900\text{--}1100^\circ\text{C}$ at 0.9–1.7 GPa; spinel peridotite stability determined for continental NVL by Armienti & Perinelli (2010)] would be negligible. Therefore if the increase in $^{206}\text{Pb}/^{204}\text{Pb}$ observed in the NWRS basalts oceanward (Fig. 10) is a result of radiogenic in-growth, then the correlation with $\delta^{18}\text{O}$ (Fig. 9) would not be expected (i.e. decoupled systems). Once again, we regard the deviation in oxygen and radiogenic isotopes from the ocean 'endmember' of the NWRS to be a consequence of the reaction between silica-undersaturated melts derived from metasomes and surrounding peridotite, increasing as melt migrates through thicker mantle lithosphere continentward. The isotopic signatures of the metasomes, on the other hand, were ultimately formed from recycled

oceanic crustal and mantle materials that were transferred to the asthenosphere through carbonatitic silicate melts derived from the down-going slab (Castillo, 2015, 2016).

Relative timing of extension, metasomatism and magmatism

There are significant time offsets between major episodes of extension and alkaline magmatism in West Antarctica. The earliest magmatism, the Meander Intrusive Group (48 to 23 Ma), in NVL followed Gondwana break-up and a broad phase of rifting within the WARS (105 to 80 Ma) by ~ 30 Myr. A focused phase of continental extension within the WARS (80 to 40 Ma) occurred ~ 25 Myr prior to the activity that formed the larger shield volcanoes along the continental coastline in the NWRS (~ 14 to > 5 Ma). Monogenetic island and seamount volcanism on the continental shelf and Adare Basin (< 5 to < 100 ka) followed extension in the Northern Basin and seafloor spreading in the Adare Basin (43 to 26 Ma) by ~ 20 Myr. Although the estimates are loosely constrained, it appears that progressively shorter time periods of offset between extension and magmatism (i.e. $\sim 30 \rightarrow 25 \rightarrow 20$ Myr) are spatially coincident with the broad shift in the location and volume of volcanism, as well as with a decrease in post-extensional lithospheric thickness to the northeast within the NWRS.

The timing of metasomatism of the mantle lithosphere in West Antarctica and New Zealand has been estimated based on model ages from isotopes. Lead model ages evaluate the in-growth of high $^{206}\text{Pb}/^{204}\text{Pb}$ ratios (≥ 20) starting from a PREMA–FOZO composition (~ 19.5) with variable U/Pb ratios. Estimates range from 500 to 200 Ma (Hart *et al.*, 1997; Panter *et al.*, 2000) and 150 to 50 Ma (Nardini *et al.*, 2009). Model ages calculated for spinel peridotites from southern New Zealand reveal metasomatic enrichments of ≤ 180 Ma (McCoy-West *et al.*, 2016), including extremely rapid in-growth over 35 to 13 Ma for some samples with very high $^{238}\text{U}/^{204}\text{Pb}$ ratios ($\mu = 63\text{--}466$). Melchiorre *et al.* (2011) presented Os model ages (time of Re depletion) for interstitial sulfides in metasomatized peridotite xenoliths from NVL that span the evolutionary history of Antarctica from the Archean–Proterozoic up to the Cretaceous, but speculated that the high proportions of eclogite required to explain the radiogenic $^{187}\text{Os}/^{186}\text{Os}$ could have been introduced into the sub-lithospheric mantle by subduction during the Ross Orogeny (550–600 Ma). They concluded that the ancient eclogitic signatures were probably incorporated into partial melts during the initial phase of WARS extension.

According to Pilet (2015), the difference between how alkaline magmas are generated in continental versus oceanic settings is that in continental settings the episode of metasomatic enrichment may be decoupled from the events that cause melting of the metasomes. This scenario has been proposed in continental NVL

and is in accordance with the time offset between rifting and magmatism discussed above. Rocchi *et al.* (2002, 2005) and Nardini *et al.* (2009) suggested that during the initial Late Cretaceous phase of WARS extension small-volume melts from the asthenosphere produced amphibole-rich metasomatic veins that become a lithospheric mantle source for subsequent alkaline magmatism from the middle Eocene to Present. The timing is probably controlled by the thermal gradient in the lithosphere, which must reach temperatures of $1150\text{--}1175^\circ\text{C}$ to allow melting of amphibole-rich cumulates (Pilet *et al.*, 2008). Thermobarometric calculations for peridotite xenoliths (Armienti & Perinelli, 2010; Perinelli *et al.*, 2011) reveal a change in the geothermal gradient from 0.5 to $\sim 3^\circ\text{C km}^{-1}$ in NVL lithosphere. The thermal evolution is estimated to have taken ~ 10 Myr and is credited to the development of edge-driven mantle convection along the boundary between the thinned lithosphere of the WARS and the thick East Antarctic craton established by the Eocene (Faccenna *et al.*, 2008).

Here we extend the model for metasomatism to include the oceanic portion of the NWRS and call upon the influence of younger, mostly amagmatic rifting to generate the low-degree sub-lithospheric melts that have enriched the lithosphere. The ultraslow spreading in the Adare Basin ($\sim 12 \text{ mm a}^{-1}$; Cande *et al.*, 2000) and its crustal characteristics, which are consistent with oceanic core complexes observed at ultraslow-spreading ridges (Selvans *et al.*, 2014), probably facilitated the repose between the melting that formed amphibole-rich veins and the melting of these metasomes to produce alkaline volcanism. Studies of ultraslow seafloor spreading (Dick *et al.*, 2003; Michael *et al.*, 2003; Cannat *et al.*, 2006) reveal that mantle melting and the resulting volcanism is not a simple function of spreading rate but that mantle temperatures and mantle lithology/composition are also controlling factors. Ultraslow spreading will lead to cooler temperatures with depth and therefore thicker lithosphere (Reid & Jackson, 1981). Moreover, temperatures for sub-lithospheric mantle beneath ultraslow-spreading ridges (70–80 km depth) may be colder by $\geq 180^\circ\text{C}$ relative to mantle beneath fast-spreading ridges (Husson *et al.*, 2015). We suggest that the temperature at the base of the oceanic lithosphere beneath the Adare Basin was cool enough to ‘freeze-in’ low-degree melts, and the metasomatic cumulates that they produced, during or soon after seafloor spreading (43–26 Ma). Furthermore, we propose that the delay in melting of the metasomes leading to seamount volcanism in the Adare Basin (< 5 Ma to < 200 ka) was controlled by the rate of conductive heating from the base of the lithosphere. Basal heating was enhanced by regional mantle upwelling related to subduction death and the sinking of the Pacific slab into the lower mantle (Finn *et al.*, 2005; Sutherland *et al.*, 2010) and possibly more recent (Neogene) edge-driven flow (Faccenna *et al.*, 2008).

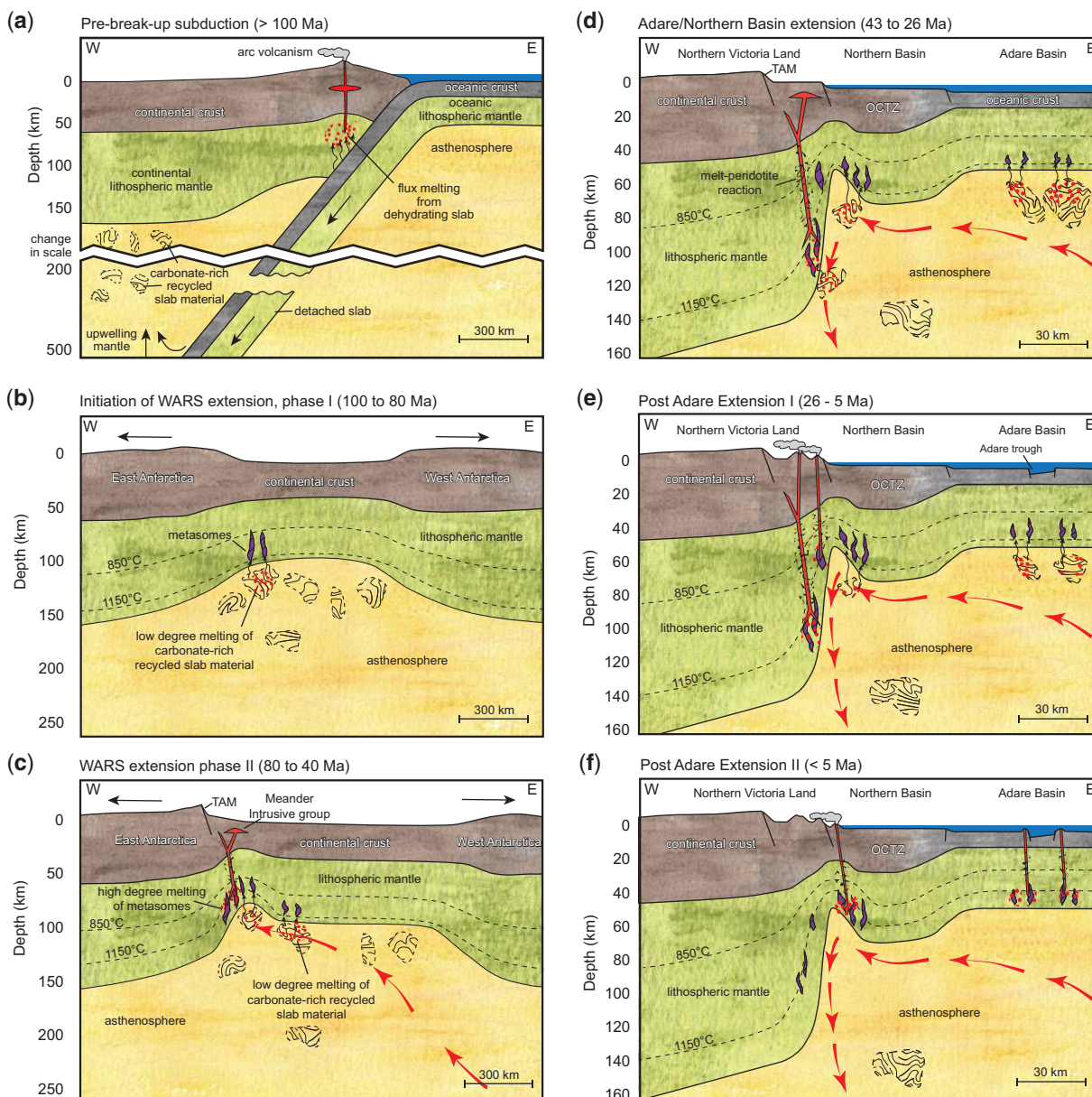


Fig. 17. Schematic illustration of Late Cretaceous to recent tectonism and the genesis of alkaline magmatism in the NWRS. (a) Pre-breakup continental arc. The subduction tectonic regime was nearly continuous from the late Neoproterozoic (~550 Ma) to Late Cretaceous (~100 Ma) along the Paleo-Pacific margin of Gondwana (Bradshaw, 1989; Cawood, 2005) and provided slab material to the asthenosphere either directly or recycled from depth in mantle upwellings. Deeper mantle upwelling may have also delivered more ancient subducted material to the asthenosphere (Castillo, 2016). (b) Broad regional extension (~100 to 80 Ma) of Antarctic continental lithosphere (DiVenere *et al.*, 1994; Luyendyk *et al.*, 1996) caused decompression melting of slab material to a small degree. The resultant carbonate-rich silicate liquids rose and froze within the cooler lithospheric mantle to produce metasomes (amphibole-rich veins; see Pilet *et al.*, 2008). The isotherms shown in this panel and in what follows are approximations that are in part constrained by the geothermal gradient estimated for NVL continental lithosphere by Armienti & Perinelli (2010). (c) Focused extension (~80 to 40 Ma) between East and West Antarctica caused incipient lithospheric necking (Huerta & Harry, 2007) and uplift of the Transantarctic Mountains (TAM; Fitzgerald *et al.*, 1986). Heating of the lithosphere at its base was intensified by mantle upwelling and the higher temperatures required to melt the metasomes (>1150°C) to a high degree occurred by about 50 Ma, which initiated the oldest known alkaline igneous activity (Meander Intrusive Group, ~48–23 Ma; Rocchi *et al.*, 2002) associated with the WARS. The silica-undersaturated liquid that was produced reacted with the surrounding peridotite as it traversed upward through the lithosphere [see (d)]. (d) (note the change in scale). Ultraslow seafloor spreading formed the oceanic lithosphere of the Adare Basin from 43 to 26 Ma (Cande *et al.*, 2000). The continuity of magnetic, seismic and structural trends from the Adare Basin into the Northern Basin (Cande & Stock, 2006; Davey *et al.*, 2006; Damaske *et al.*, 2007; Ferraccioli *et al.*, 2009; Selvans *et al.*, 2012) indicates that the oceanic crust extends across the continental shelf break (Granot *et al.*, 2013; Selvans *et al.*, 2016) and thus the transition in lithospheric type may be gradational from ocean to continent (OCTZ). Edge-driven convective flow was established at the boundary between thinned lithosphere and the thick East Antarctic craton (Faccenna *et al.*, 2008). Metasomes were formed in the cooler OCTZ and oceanic lithosphere while the earlier-formed metasomes in the warmed continental lithosphere continued to melt supplying magma for the Meander Intrusive Group until ~23 Ma. (e) Minor post-spreading extensional events in the Adare Basin occurred at ~24 and ~17 Ma and formation of the Adare Trough occurred (Granot *et al.*, 2010, 2013). Alkaline magmatism resumed after an ~10 Myr hiatus to form shield volcano complexes (~14 to > 5 Ma) located along rift-shoulder fault systems. (f) Thermal evolution of the lithosphere oceanward reached the melting temperature of metasomes by ~5 Ma to produce small-volume volcanic seamounts on the continental shelf and in the Adare Basin.

Integrated model for magmatism

The model we use to explain the origin of alkaline magmatism in the NWRS is illustrated in Fig. 17. Our model is intimately connected to what is known of the tectonic evolution of the region beginning at a time prior to the break-up of the proto-Pacific margin of Gondwana (Fig. 17a). The protracted history of subduction along this margin is considered to have supplied carbonate-rich slab material directly or by longer-term recycling into the upper asthenosphere; however, our model does not preclude the contribution from more ancient subduction-related sources. A series of extensional phases occurred in the development of the WARS, which caused lithospheric thinning and decompression melting of this recycled material in the asthenosphere, probably aided by heating from passive mantle upwelling and edge-driven flow (Fig. 17b–e). The carbonate-rich silicate melt produced by these small degrees of melting did not reach the crust but crystallized in the mantle lithosphere to form amphibole-rich cumulates (metasomes) that later became the source of alkaline magmatism. The metasomatic enrichment of the lithosphere is invoked in our model not only to explain some of the geochemical and isotopic characteristics of the basalts and xenoliths described in this and other studies, but also to explain why major periods of extension are not concurrent with, or immediately followed by, magmatism. Other geodynamic evidence for lithospheric mantle sources for alkaline magmatism found on former pieces of Gondwana (DAMP; Finn *et al.*, 2005) has been provided by Panter *et al.* (2006). They documented the occurrence of relatively uniform mafic alkaline compositions on Chatham Island that were derived from an amphibole-bearing mantle source and erupted intermittently over an 80 Myr period (85 to 5 Ma) as the continental lithosphere of Zealandia rifted away from West Antarctica and drifted north over a distance > 3000 km. Specific to the NWRS portion of the DAMP is that this region represents a recently rifted continental margin across which the lithosphere varies in both thickness and age (Fig. 17). We have shown that this is coincident with gradational changes in basalt geochemistry, Sr–Nd–Pb–O isotopes (Figs 10 and 15c) and broadly with eruption age. Our model explains these features by invoking an oceanward progression in melting of the metasomes facilitated by the thermal evolution of the lithosphere and coupled to a decrease in the extent of reaction between melt and peridotite prior to eruption, which, in turn, is controlled by lithospheric thickness (Fig. 17c–f).

This multi-stage model for alkaline volcanism in the NW Ross Sea is relevant to interpretations on the origin and cause of alkaline magmatism within the rest of the West Antarctic rift system, as well as other continental areas of the southwestern Pacific (i.e. DAMP). Importantly, our model is constructed using contemporaneous, petrogenetically related, alkaline magmas that show a transition (compositionally) across the

boundary between continental and oceanic lithosphere, and is further constrained by the dynamic thermal–tectonic evolution of the region. The contribution of lithospheric mantle, both continental and oceanic, as a source and a contaminant of Si-undersaturated melts is important to understand and should be carefully considered in studies of alkaline basalts worldwide.

ACKNOWLEDGEMENTS

We would like to thank Anne Grunow from the US Polar Rock Repository (supported by NSF OPP 1141906) and Nick Mortimer (GNS Science) for providing some of the land-based samples used in this study. We are especially grateful to the Captain and crew of RV/IB *Nathaniel B. Palmer* for the successful dredging campaign in the Adare Basin. We thank Mike Spicuzza for analysis of oxygen isotope ratios at University of Wisconsin–Madison by laser fluorination and gas-source mass spectrometry. Gordon Moore is thanked for his guidance with electron microprobe analysis at the University of Michigan. We are grateful for the thoughtful and constructive reviews provided by Joshua Schwartz, Sebastien Pilet and Karsten Haase, as well as the editorial handling by Georg Zellmer. Also, we are appreciative of the helpful comments provided by Tyrone Rooney and Adam Martin during the writing of this paper.

FUNDING

This study was supported by National Science Foundation grants ANT 0943503, ANT 0943274 and OPP 05-38374. P.R.K. acknowledges support from NSF grant ANT 1141534. WiscSIMS is supported by NSF EAR 1355590 and the University of Wisconsin–Madison.

SUPPLEMENTARY DATA

Supplementary data for this paper are available at *Journal of Petrology* online.

REFERENCES

- Abouchami, W., Galer, S. J. G. & Koschinsky, A. (1999). Pb and Nd isotopes in NE Atlantic Fe–Mn crusts: proxies for trace metal paleosources and paleocean circulation. *Geochimica et Cosmochimica Acta* **63**, 1489–1505.
- Armienti, P. & Perinelli, C. (2010). Cenozoic thermal evolution of lithospheric mantle in northern Victoria Land (Antarctica): evidences from mantle xenoliths. *Tectonophysics* **486**, 28–35.
- Armienti, P., Francalanci, L., Landi, P. & Vita, G. (2003). Age and geochemistry of volcanic rocks from Daniell Peninsula and Coulman Island, Hallett Volcanic Province, Antarctica. In: Tessensohn, F. & Ricci, C. A. (eds) *Aspects of a Suture Zone. Geologisches Jahrbuch, Polar Issue* **9**, 409–445.
- Aviado, K. B., Rilling-Hall, S., Bryce, J. G. & Mukasa, S. B. (2015). Submarine and subaerial lavas in the West Antarctic Rift System: temporal record of shifting magma source

- components from the lithosphere and asthenosphere. *Geochemistry, Geophysics, Geosystems* **16**, 4344–4361.
- Beattie, P. (1993). Olivine–melt and orthopyroxene–melt equilibria. *Contributions to Mineralogy and Petrology* **115**, 103–111.
- Beccaluva, L., Bianchini, G., Bonadiman, C., Coltorti, M., Milani, L., Salvini, L., Siena, F. & Tassinari, R. (2007). Intraplate lithospheric and sublithospheric components in the Adriatic domain: Nephelinite to tholeiite magma generation in the Paleogene Veneto volcanic province, Southern Alps. In: Beccaluva, L., Bianchini, G., & Wilson, W. (eds) *Cenozoic Volcanism in the Mediterranean Area*. Geological Society of America, Special Papers **418**, 131–152.
- Behrendt, J. C. (1999). Crustal and lithospheric structure of the West Antarctic Rift System from geophysical investigations—a review. *Global and Planetary Change* **23**, 25–44.
- Boger, S. D. & Miller, J. M. (2004). Terminal suturing of Gondwana and the onset of the Ross–Delamerian Orogeny: the cause and effect of an Early Cambrian reconfiguration of plate motions. *Earth and Planetary Science Letters* **219**, 35–48.
- Borg, S. G. & Stump, E. (1987). Paleozoic magmatism and associated tectonic problems of Northern Victoria Land, Antarctica. In: McKenzie, G. D. (ed.) *Gondwana Six: Structure, Tectonics, and Geophysics*. *Geophysical Monograph, American Geophysical Union* **40**, 67–75.
- Bosch, D., Maury, R. C., El Azzouzi, M., Bollinger, C., Bellon, H. & Verdoux, P. (2014). Lithospheric origin for Neogene–Quaternary Middle Atlas lavas (Morocco): clues from trace elements and Sr–Nd–Pb–Hf isotopes. *Lithos* **205**, 247–265.
- Bradshaw, J. D. (1989). Cretaceous geotectonic patterns in the New Zealand region. *Tectonics* **8**, 803–820.
- Brey, G., Brice, W. R., Ellis, D. J., Green, D. H., Harris, K. L. & Ryabchikov, I. D. (1983). Pyroxene–carbonate reactions in the upper mantle. *Earth and Planetary Science Letters* **62**, 63–74.
- Broadley, M. W., Ballentine, C. J., Chavrit, D., Dallai, L. & Burgess, R. (2016). Sedimentary halogens and noble gases within Western Antarctic xenoliths: implications of extensive volatile recycling to the subcontinental lithospheric mantle. *Geochimica et Cosmochimica Acta* **176**, 139–156.
- Buseti, M., Spadini, G., Van der Wateren, F. M., Cloetingh, S. & Zanolla, C. (1999). Kinematic modelling of the west Antarctic rift system, Ross Sea, Antarctica. *Global and Planetary Change* **23**, 79–103.
- Cande, S. C. & Stock, J. M. (2006). Constraints on the timing of extension in the Northern Basin, Ross Sea. In: Futterer, D. K., Damaske, D., Kleinschmidt, G., Miller, H. & Tessensohn, F. (eds) *Antarctica: Contributions to Global Earth Sciences*. Springer, pp. 319–326.
- Cande, S. C., Stock, J. M., Müller, R. D. & Ishihara, T. (2000). Cenozoic motion between east and west Antarctica. *Nature* **404**, 145–150.
- Cannat, M., Sauter, D., Mendel, V., Ruellan, E., Okino, K., Escartin, J., Combier, V. & Baala, M. (2006). Modes of sea-floor generation at a melt-poor ultraslow-spreading ridge. *Geology* **34**, 605–608.
- Caroff, M., Maury, R. C., Guille, G. & Cotten, J. (1997). Partial melting below Tubuai (Austral Islands, French Polynesia). *Contributions to Mineralogy and Petrology* **127**, 369–382.
- Castillo, P. R. (2015). The recycling of marine carbonates and sources of HIMU and FOZO ocean island basalts. *Lithos* **216–217**, 254–263.
- Castillo, P. R. (2016). A proposed new approach and unified solution to old Pb paradoxes. *Lithos* **252–253**, 32–40.
- Castillo, P. R., Clague, D. A., Davis, A. S. & Lonsdale, P. F. (2010). Petrogenesis of Davidson Seamount lavas and its implications for fossil spreading center and intraplate magmatism in the eastern Pacific. *Geochemistry, Geophysics, Geosystems* **11**, doi:10.1029/2009GC002992.
- Cawood, P. A. (2005). Terra Australis Orogen: Rodinia breakup and development of the Pacific and Iapetus margins of Gondwana during the Neoproterozoic and Paleozoic. *Earth-Science Reviews* **69**, 249–279.
- Chakhmouradian, A. R. (2006). High-field-strength elements in carbonatitic rocks: geochemistry, crystal chemistry and significance for constraining the sources of carbonatites. *Chemical Geology* **235**, 138–160.
- Chauvel, C., Hofmann, A. W. & Vidal, P. (1992). HIMU-EM: the French Polynesian connection. *Earth and Planetary Science Letters* **110**, 99–119.
- Chen, C., Liu, Y., Foley, S. F., Ducea, M. N., He, D., Hu, Z., Chen, W. & Zong, K. (2016). Paleo-Asian oceanic slab under the North China craton revealed by carbonatites derived from subducted limestones. *Geology* **44**, 1039–1042.
- Coltorti, M., Beccaluva, L., Bonadiman, C., Faccini, B., Ntaflou, T. & Siena, F. (2004). Amphibole genesis via metasomatic reaction with clinopyroxene in mantle xenoliths from Victoria Land, Antarctica. *Lithos* **75**, 115–139.
- Cooper, A. K., Davey, F. J. & Behrendt, J. C. (1987). Seismic stratigraphy and structure of the Victoria Land Basin, Western Ross Sea, Antarctica. In: Cooper, A. K. & Davey, F. J. (eds) *The Antarctic Continental Margin: Geology and Geophysics of the Western Ross Sea, CPCMR Earth Science Series, v. 5B*. Circum-Pacific Council for Energy and Mineral Resources, p. 27.
- Dallai, L., Ghezzi, C. & Sharp, Z. (2003). Oxygen isotope evidence for crustal assimilation and magma mixing in the Granite Harbour Intrusives, Northern Victoria Land, Antarctica. *Lithos* **67**, 135–151.
- Damaske, D., Läufer, A. L., Goldmann, F., Möller, H. D. & Lisker, F. (2007). Magnetic anomalies north-east of Cape Adare, northern Victoria Land (Antarctica), and their relation to on-shore structures. In: Cooper, A. K. & Raymond, C. R., et al. (eds) *Proceedings of the 10th International Symposium on Antarctic Earth Sciences. US Geological Survey Open-File Report 2007-1047*, Short Research Paper 016, p. 5.
- Danesi, S. & Morelli, A. (2001). Structure of the upper mantle under the Antarctic Plate from surface wave tomography. *Geophysical Research Letters* **28**, 4395–4398.
- Dasgupta, R., Hirschmann, M. M. & Stalker, K. (2006). Immiscible transition from carbonate-rich to silicate-rich melts in the 3 GPa melting interval of eclogite + CO₂ and genesis of silica-undersaturated ocean island lavas. *Journal of Petrology* **47**, 647–671.
- Dasgupta, R., Hirschmann, M. M. & Smith, N. D. (2007). Partial melting experiments on peridotite + CO₂ at 3 GPa and genesis of alkalic ocean island basalts. *Journal of Petrology* **48**, 2093–2124.
- Davey, F. J., Cande, S. C. & Stock, J. M. (2006). Extension in the western Ross Sea region—links between Adare Basin and Victoria Land Basin. *Geophysical Research Letters* **33**, doi: 10.1029/2006GL027383.
- Davy, B., Hoernle, K. & Werner, R. (2008). Hikurangi Plateau: crustal structure, rifted formation, and Gondwana subduction history. *Geochemistry, Geophysics, Geosystems* **9**, doi: 10.1029/2007GC001855.
- Day, J. M. D., Pearson, D. G., Macpherson, C. G., Lowry, D. & Carracedo, J. C. (2010). Evidence for distinct proportions of subducted oceanic crust and lithosphere in HIMU-type mantle beneath El Hierro and La Palma, Canary Islands. *Geochimica et Cosmochimica Acta* **74**, 6565–6589.

- Deer, W. A., Howie, R. A. & Zussman, J. (1992). *An Introduction to the Rock-Forming Minerals*, 2nd edn. Longman, 696 pp.
- DePaolo, D. J. (1981). Trace element and isotopic effects of combined wallrock assimilation and fractional crystallization. *Earth and Planetary Science Letters* **53**, 189–202.
- Dick, H. J., Lin, J. & Schouten, H. (2003). An ultraslow-spreading class of ocean ridge. *Nature* **426**, 405–412.
- DiVenere, V. J., Kent, D. V. & Dalziel, I. W. D. (1994). Mid-Cretaceous paleomagnetic results from Marie Byrd Land, West Antarctica: a test of post-100 Ma relative motion between East and West Antarctica. *Journal of Geophysical Research* **99**, 15115.
- Di Vincenzo, G. & Rocchi, S. (1999). Origin and interaction of mafic and felsic magmas in an evolving late orogenic setting: the Early Paleozoic Terra Nova Intrusive Complex, Antarctica. *Contributions to Mineralogy and Petrology* **137**, 15–35.
- Di Vincenzo, G., Palmeri, R., Talarico, F., Andriessen, P. A. M. & Ricci, G. A. (1997). Petrology and geochronology of eclogites from the Lanterman Range, Antarctica. *Journal of Petrology* **38**, 1391–1417.
- Di Vincenzo, G., Grande, A. & Rossetti, F. (2014). Paleozoic siliciclastic rocks from northern Victoria Land (Antarctica): provenance, timing of deformation, and implications for the Antarctica–Australia connection. *Geological Society of America Bulletin* **126**, 1416–1438.
- Di Vincenzo, G., Horton, F. & Palmeri, R. (2016). Protracted (~30 Ma) eclogite-facies metamorphism in northern Victoria Land (Antarctica): implications for the geodynamics of the Ross/Delamerian Orogen. *Gondwana Research* **40**, 91–106.
- Eiler, J. M. (2001). Oxygen isotope variations of basaltic lavas and upper mantle rocks. In: Valley, J. W. & Cole, D. (eds) *Stable Isotope Geochemistry*. Mineralogical Society of America and Geochemical Society, *Reviews in Mineralogy and Geochemistry* **43**, 319–364.
- Eiler, J. M., Farley, K. A., Valley, J. W., Hofmann, A. W. & Stolper, E. M. (1996). Oxygen isotope constraints on the sources of Hawaiian volcanism. *Earth and Planetary Science Letters* **144**, 453–468.
- Elliot, D. H. & Fleming, T. H. (2004). Occurrence and dispersal of magmas in the Jurassic Ferrar large igneous province, Antarctica. *Gondwana Research* **7**, 223–237.
- Elliot, D. H., Fleming, T. H., Kyle, P. R. & Foland, K. A. (1999). Long-distance transport of magmas in the Jurassic Ferrar Large Igneous Province, Antarctica. *Earth and Planetary Science Letters* **167**, 89–104.
- Emry, E. L., Nyblade, A. A., Julià, J., Anandakrishnan, S., Aster, R. C., Wiens, D. A., Huerta, A. D. & Wilson, T. J. (2015). The mantle transition zone beneath West Antarctica: seismic evidence for hydration and thermal upwellings. *Geochemistry, Geophysics, Geosystems* **16**, 40–58.
- Ersoy, E. Y., Helvacı, C. & Palmer, M. R. (2010). Mantle source characteristics and melting models for the early–middle Miocene mafic volcanism in Western Anatolia: implications for enrichment processes of mantle lithosphere and origin of K-rich volcanism in post-collisional settings. *Journal of Volcanology and Geothermal Research* **198**, 112–128.
- Faccenna, C., Rossetti, F., Becker, T. W., Danesi, S. & Morelli, A. (2008). Recent extension driven by mantle upwelling beneath the Admiralty Mountains (East Antarctica). *Tectonics* **27**, doi:10.1029/2007TC002197.
- Ferraccioli, F., Armadillo, E., Jordan, T., Bozzo, E. & Corr, H. (2009). Aeromagnetic exploration over the East Antarctic Ice Sheet: a new view of the Wilkes Subglacial Basin. *Tectonophysics* **478**, 62–77.
- Finn, C. A., Müller, R. D. & Panter, K. S. (2005). A Cenozoic diffuse alkaline magmatic province (DAMP) in the southwest Pacific without rift or plume origin. *Geochemistry, Geophysics, Geosystems* **6**, doi:10.1029/2004GC000723.
- Fitton, J. G. & Dunlop, H. M. (1985). The Cameroon line, West Africa, and its bearing on the origin of oceanic and continental alkali basalt. *Earth and Planetary Science Letters* **72**, 23–38.
- Fitzgerald, P. G., Sandiford, M., Barrett, P. J. & Gleadow, A. J. (1986). Asymmetric extension associated with uplift and subsidence in the Transantarctic Mountains and Ross Embayment. *Earth and Planetary Science Letters* **81**, 67–78.
- Fretwell, P., Pritchard, H. D., Vaughan, D. G., et al. (2013). Bedmap2: improved ice bed, surface and thickness datasets for Antarctica. *Cryosphere* **7**, 375–393.
- Frey, F. A., Green, D. H. & Roy, S. D. (1978). Integrated models of basalt petrogenesis: a study of quartz tholeiites to olivine melilitites from south eastern Australia utilizing geochemical and experimental petrological data. *Journal of Petrology* **19**, 463–513.
- Früh-Green, G. L., Scambelluri, M. & Vallis, F. (2001). O–H isotope ratios of high pressure ultramafic rocks: implications for fluid sources and mobility in the subducted hydrous mantle. *Contributions to Mineralogy and Petrology* **141**, 145–159.
- Gao, Y., Vils, F., Cooper, K. M., Banerjee, N., Harris, M., Hoefs, J., Teagle, D. A. H., Casey, J. F., Elliott, T., Laverne, C., Alt, J. C. & Muehlenbachs, K. (2012). Downhole variation of lithium and oxygen isotopic compositions of oceanic crust at East Pacific Rise, ODP Site 1256. *Geochemistry, Geophysics, Geosystems* **13**, doi:10.1029/2012GC004207.
- Garcia, M. O., Ito, E. & Eiler, J. M. (2007). Oxygen isotope evidence for chemical interaction of Kilauea historical magmas with basement rocks. *Journal of Petrology* **49**, 757–769.
- Genske, F. S., Beier, C., Haase, K. M., Turner, S. P., Krumm, S. & Brandl, P. A. (2013). Oxygen isotopes in the Azores islands: crustal assimilation recorded in olivine. *Geology* **41**, 491–494.
- Gerbode, C. & Dasgupta, R. (2010). Carbonate-fluxed melting of MORB-like pyroxenite at 2–9 GPa and genesis of HIMU ocean island basalts. *Journal of Petrology* **51**, 2067–2088.
- Ghiribelli, B. (2000). Evoluzione tettonica e metamorfica del margine attivo del Gondwana: Lanterman e Salamander Ranges (Antartide). PhD thesis, Università degli Studi di Siena, Siena, 127 pp.
- Granot, R., Cande, S. C., Stock, J. M., Davey, F. J. & Clayton, R. W. (2010). Postspreading rifting in the Adare Basin, Antarctica: regional tectonic consequences. *Geochemistry, Geophysics, Geosystems* **11**, doi:10.1029/2010GC003105.
- Granot, R., Cande, S. C., Stock, J. M. & Damaske, D. (2013). Revised Eocene–Oligocene kinematics for the West Antarctic rift system. *Geophysical Research Letters* **40**, 279–284.
- Gurenko, A. A., Hoernle, K. A., Hauff, F., Schmincke, H.-U., Han, D., Miura, Y. N. & Kaneoka, I. (2006). Major, trace element and Nd–Sr–Pb–O–He–Ar isotope signatures of shield stage lavas from the central and western Canary Islands: insights into mantle and crustal processes. *Chemical Geology* **233**, 75–112.
- Gurenko, A. A., Bindeman, I. N. & Chaussidon, M. (2011). Oxygen isotope heterogeneity of the mantle beneath the Canary Islands: insights from olivine phenocrysts. *Contributions to Mineralogy and Petrology* **162**, 349–363.
- Hallett, R. B. & Kyle, P. R. (1993). XRF and INAA determinations of major and trace elements in Geological Survey of Japan igneous and sedimentary rock standards. *Geostandards and Geoanalytical Research* **17**, 127–133.
- Hamilton, W. (1972). *The Hallett Volcanic Province*. US Geological Survey Professional Paper **456C**, 61 pp.

- Harmon, R. S. & Hoefs, J. (1995). Oxygen isotope heterogeneity of the mantle deduced from global ^{18}O systematics of basalts from different geotectonic settings. *Contributions to Mineralogy and Petrology* **120**, 95–114.
- Hart, S. R. & Gaetani, G. A. (2006). Mantle Pb paradoxes: the sulfide solution. *Contributions to Mineralogy and Petrology* **152**, 295–308.
- Hart, S. R., Hauri, E. H., Oschmann, L. A. & Whitehead, J. A. (1992). Mantle plumes and entrainment: isotopic evidence. *Science* **256**, 517–520.
- Hart, S. R., Blijstajin, J. & Craddock, C. (1995). Cenozoic volcanism in Antarctica; Jones Mountains and Peter I Island. *Geochimica et Cosmochimica Acta* **59**, 3379–3388.
- Hart, S. R., Blusztajn, J., LeMasurier, W. E. & Rex, D. C. (1997). Hobbs Coast Cenozoic volcanism: implications for the West Antarctic rift system. *Chemical Geology* **139**, 223–248.
- Hart, S. R., Blusztajn, J., Dick, H. J. B., Meyer, P. S. & Muehlenbachs, K. (1999). The fingerprint of seawater circulation in a 500-meter section of ocean crust gabbros. *Geochimica et Cosmochimica Acta* **63**, 4059–4080.
- Hartmann, G. & Wedepohl, K. H. (1990). Metasomatically altered peridotite xenoliths from the Hessian Depression (Northwest Germany). *Geochimica et Cosmochimica Acta* **54**, 71–86.
- Hawthorne, F. C., Oberti, R., Harlow, G. E., Maresch, W. V., Martin, R. F., Schumacher, J. C. & Welch, M. D. (2012). IMA report: nomenclature of the amphibole supergroup. *American Mineralogist* **97**, 2031–2048.
- Heeszel, D. S., Wiens, D. A., Anandakrishnan, S., Aster, R. C., Dalziel, I. W. D., Huerta, A. D., Nyblade, A. A., Wilson, T. J. & Winberry, J. P. (2016). Upper mantle structure of central and West Antarctica from array analysis of Rayleigh wave phase velocities: mantle structure of West Antarctica. *Journal of Geophysical Research: Solid Earth* **121**, 1758–1775.
- Henjes-Kunst, F. & Schussler, U. (2003). Metasedimentary units of the Cambro-Ordovician Ross Orogen in northern Victoria Land and Oates Land: implications for their provenance and geotectonic setting from geochemical and Nd–Sr isotope data. *Terra Antarctica* **10**, 105–128.
- Hergt, J. M., Peate, D. W. & Hawkesworth, C. J. (1991). The petrogenesis of Mesozoic Gondwana low-Ti flood basalts. *Earth and Planetary Science Letters* **105**, 134–148.
- Herzberg, C. (2006). Petrology and thermal structure of the Hawaiian plume from Mauna Kea volcano. *Nature* **444**, 605–609.
- Herzberg, C. & Asimow, P. D. (2008). Petrology of some oceanic island basalts: PRIMELT2.XLS software for primary magma calculation. *Geochemistry, Geophysics, Geosystems* **9**, doi: 10.1029/2008GC002057.
- Hirschmann, M. M., Kogiso, T., Baker, M. B. & Stolper, E. M. (2003). Alkalic magmas generated by partial melting of garnet pyroxenite. *Geology* **31**, 481–484.
- Hofmann, A. W. (1988). Chemical differentiation of the Earth: the relationship between mantle, continental crust, and oceanic crust. *Earth and Planetary Science Letters* **90**, 297–314.
- Hofmann, A. W. (2014). *Sampling Mantle Heterogeneity through Oceanic Basalts: Isotopes and Trace Elements*, Vol. 3, 2nd edn. *Treatise on Geochemistry*, Elsevier. pp. 67–101.
- Huerta, A. D. & Harry, D. L. (2007). The transition from diffuse to focused extension: modeled evolution of the West Antarctic Rift system. *Earth and Planetary Science Letters* **255**, 133–147.
- Husson, L., Yamato, P. & Bézou, A. (2015). Ultraslow, slow, or fast spreading ridges: arm wrestling between mantle convection and far-field tectonics. *Earth and Planetary Science Letters* **429**, 205–215.
- Ionov, D. A. & Hofmann, A. W. (1995). Nb–Ta-rich mantle amphiboles and micas: implications for subduction-related metasomatic trace element fractionations. *Earth and Planetary Science Letters* **131**, 341–356.
- Irvine, T. N. & Baragar, W. R. A. (1971). A guide to the chemical classification of the common volcanic rocks. *Canadian Journal of Earth Sciences* **8**, 523–548.
- Isbell, J. L. (1999). The Kukri Erosion Surface; a reassessment of its relationship to rocks of the Beacon Supergroup in the central Transantarctic Mountains, Antarctica. *Antarctic Science* **11**, 228–239.
- Ivanov, A. V., Meffre, S., Thompson, J., Corfu, F., Kamenetsky, V. S., Kamenetsky, M. B. & Demonerova, E. I. (2017). Timing and genesis of the Karoo–Ferrar large igneous province: new high precision U–Pb data for Tasmania confirm short duration of the major magmatic pulse. *Chemical Geology* **455**, 32–43.
- Jackson, M. G., Hart, S. R., Saal, A. E., Shimizu, N., Kurz, M. D., Blusztajn, J. S. & Skovgaard, A. C. (2008). Globally elevated titanium, tantalum, and niobium (TITAN) in ocean island basalts with high $^3\text{He}/^4\text{He}$. *Geochemistry, Geophysics, Geosystems* **9**, doi:10.1029/2007GC001876.
- Janney, P. E. & Castillo, P. R. (1996). Basalts from the Central Pacific Basin: evidence for the origin of Cretaceous igneous complexes in the Jurassic western Pacific. *Journal of Geophysical Research: Solid Earth* **101**, 2875–2893.
- John, T., Scherer, E. E., Haase, K. & Schenk, V. (2004). Trace element fractionation during fluid-induced eclogitization in a subducting slab: trace element and Lu–Hf–Sm–Nd isotope systematics. *Earth and Planetary Science Letters* **227**, 441–456.
- Jung, S., Pfänder, J. A., Brüggmann, G. & Stracke, A. (2005). Sources of primitive alkaline volcanic rocks from the Central European Volcanic Province (Rhön, Germany) inferred from Hf, Os and Pb isotopes. *Contributions to Mineralogy and Petrology* **150**, 546–559.
- Kalfoun, F., Ionov, D. & Merlet, C. (2002). HFSE residence and Nb/Ta ratios in metasomatised, rutile-bearing mantle peridotites. *Earth and Planetary Science Letters* **199**, 49–65.
- Kendrick, M. A., Honda, M., Pettke, T., Scambelluri, M., Phillips, D. & Giuliani, A. (2013). Subduction zone fluxes of halogens and noble gases in seafloor and forearc serpentinites. *Earth and Planetary Science Letters* **365**, 86–96.
- Keshav, S., Gudfinnsson, G. H., Sen, G. & Fei, Y. (2004). High-pressure melting experiments on garnet clinopyroxenite and the alkalic to tholeiitic transition in ocean-island basalts. *Earth and Planetary Science Letters* **223**, 365–379.
- Kipf, A., Hauff, F., Werner, R., Gohl, K., van den Bogaard, P., Hoernle, K., Maicher, D. & Klügel, A. (2014). Seamounts off the West Antarctic margin: a case for non-hotspot driven intraplate volcanism. *Gondwana Research* **25**, 1660–1679.
- Kita, N. T., Ushikubo, T., Fu, B. & Valley, J. W. (2009). High precision SIMS oxygen isotope analysis and the effect of sample topography. *Chemical Geology* **264**, 43–57.
- Krans, S. R. (2013). New mineral chemistry and oxygen isotopes from alkaline basalts in the Northwest Ross Sea, Antarctica: insights on magma genesis across rifted continental and oceanic lithosphere. MS thesis, Bowling Green State University, Bowling Green, OH.
- Kyle, P. R. (1986). Mineral chemistry of Late Cenozoic McMurdo Volcanic Group rocks from the Pleiades, Northern Victoria Land. In: Stump, E. (ed.) *Geological Investigations in Northern Victoria Land*. *Antarctic Research Series, American Geophysical Union* **46**, 305–337.
- Kyle, P. R. (1990). A. McMurdo Volcanic Group Western Ross Embayment. In: LeMasurier, W. E. & Thomson, J. W. (eds) *Volcanoes of the Antarctic Plate and Southern Oceans*.

- Antarctic Research Series, American Geophysical Union* **48**, 18–145.
- Kyle, P. R. & Muncy, H. L. (1989). The geochemistry of McMurdo Volcanic Group rocks. *Antarctic Journal of the United States* **1**, 14–16.
- Kyle, P. R., Moore, J. A. & Thirlwall, M. F. (1992). Petrologic evolution of anorthoclase phonolite lavas at Mount Erebus, Ross Island, Antarctica. *Journal of Petrology* **33**, 849–875.
- Lambart, S., Laporte, D., Provost, A. & Schiano, P. (2012). Fate of pyroxenite-derived melts in the peridotitic mantle: thermodynamic and experimental constraints. *Journal of Petrology* **53**, 451–476.
- Lambart, S., Laporte, D. & Schiano, P. (2013). Markers of the pyroxenite contribution in the major-element compositions of oceanic basalts: review of the experimental constraints. *Lithos* **160–161**, 14–36.
- Lanyon, R., Varne, R. & Crawford, A. J. (1993). Tasmanian Tertiary basalts, the Balleny plume, and opening of the Tasman Sea (southwest Pacific Ocean). *Geology* **21**, 555–558.
- LaTourrette, T., Hervig, R. L. & Holloway, J. R. (1995). Trace element partitioning between amphibole, phlogopite, and basanite melt. *Earth and Planetary Science Letters* **135**, 13–30.
- Le Bas, M. J. L., Le Maitre, R. W., Streckeisen, A. & Zanettin, B. (1986). A chemical classification of volcanic rocks based on the total alkali–silica diagram. *Journal of Petrology* **27**, 745–750.
- Li, H., Xu, Y., Ryan, J. G. & Whattam, S. A. (2017). Evolution of the mantle beneath the eastern North China Craton during the Cenozoic: linking geochemical and geophysical observations. *Journal of Geophysical Research: Solid Earth* **122**, 224–246.
- Lundstrom, C. C., Gill, J. & Williams, Q. (2000). A geochemically consistent hypothesis for MORB generation. *Chemical Geology* **162**, 105–126.
- Luyendyk, B. P. (1995). Hypothesis for Cretaceous rifting of east Gondwana caused by subducted slab capture. *Geology* **23**, 373–376.
- Luyendyk, B., Cisowski, S., Smith, C., Richard, S. & Kimbrough, D. (1996). Paleomagnetic study of the northern Ford Ranges, western Marie Byrd Land, West Antarctica: motion between West and East Antarctica. *Tectonics* **15**, 122–141.
- Ma, G. S.-K., Malpas, J., Xenophontos, C. & Chan, G. H.-N. (2011). Petrogenesis of latest Miocene–Quaternary continental intraplate volcanism along the northern Dead Sea fault system (Al Ghab–Homs Volcanic Field), Western Syria: evidence for lithosphere–asthenosphere interaction. *Journal of Petrology* **52**, 401–430.
- Mallik, A. & Dasgupta, R. (2014). Effect of variable CO₂ on eclogite-derived andesite and lherzolite reaction at 3 GPa—implications for mantle source characteristics of alkaline ocean island basalts. *Geochemistry, Geophysics, Geosystems* **15**, 1533–1557.
- Martin, A. P., Cooper, A. F. & Price, R. C. (2013). Petrogenesis of Cenozoic, alkalic volcanic lineages at Mount Morning, West Antarctica and their entrained lithospheric mantle xenoliths: lithospheric versus asthenospheric mantle sources. *Geochimica et Cosmochimica Acta* **122**, 127–152.
- Martin, A. P., Cooper, A. F. & Price, R. C. (2014). Increased mantle heat flow with on-going rifting of the West Antarctic rift system inferred from characterisation of plagioclase peridotite in the shallow Antarctic mantle. *Lithos* **190–191**, 173–190.
- Martin, A. P., Price, R. C., Cooper, A. F. & McCammon, C. A. (2015). Petrogenesis of the rifted southern Victoria Land lithospheric mantle, Antarctica, inferred from petrography, geochemistry, thermobarometry and oxybarometry of peridotite and pyroxenite xenoliths from the Mount Morning eruptive centre. *Journal of Petrology* **56**, 193–226.
- Mattey, D., Lowry, D. & Macpherson, C. (1994). Oxygen isotope composition of mantle peridotite. *Earth and Planetary Science Letters* **128**, 231–241.
- Mayer, B., Jung, S., Romer, R. L., Pfänder, J. A., Klügel, A., Pack, A. & Gröner, E. (2014). Amphibole in alkaline basalts from intraplate settings: implications for the petrogenesis of alkaline lavas from the metasomatised lithospheric mantle. *Contributions to Mineralogy and Petrology* **167**, 2095–2123.
- McCoy-West, A. J., Baker, J. A., Faure, K. & Wysoczanski, R. (2010). Petrogenesis and origins of mid-Cretaceous continental intraplate volcanism in Marlborough, New Zealand: implications for the long-lived HIMU magmatic mega-province of the SW Pacific. *Journal of Petrology* **51**, 2003–2045.
- McCoy-West, A. J., Bennett, V. C. & Amelin, Y. (2016). Rapid Cenozoic ingrowth of isotopic signatures simulating ‘HIMU’ in ancient lithospheric mantle: distinguishing source from process. *Geochimica et Cosmochimica Acta* **187**, 79–101.
- McIntosh, W. C. & Kyle, P. R. (1990). Adare Peninsula. In: LeMasurier, W. E. & Thomson, J. W. (eds) *Volcanoes of the Antarctic Plate and Southern Oceans, Antarctic Research Series, American Geophysical Union* **48**, 32–35.
- Médard, E., Schmidt, M. W., Schiano, P. & Ottolini, L. (2006). Melting of amphibole-bearing wehrlites: an experimental study on the origin of ultra-calcic nepheline-normative melts. *Journal of Petrology* **47**, 481–504.
- Melchiorre, M., Coltorti, M., Bonadiman, C., Faccini, B., O’Reilly, S. Y. & Pearson, N. J. (2011). The role of eclogite in the rift-related metasomatism and Cenozoic magmatism of Northern Victoria Land, Antarctica. *Lithos* **124**, 319–330.
- Michael, P. J., Langmuir, C. H., Dick, H. J. B., Snow, J. E., Goldstein, S. L., Graham, D. W., Lehnert, K., Kurras, G., Jokat, W., Mühe, R. & Edmonds, H. N. (2003). Magmatic and amagmatic seafloor generation at the ultraslow-spreading Gakkel ridge, Arctic Ocean. *Nature* **423**, 956–961.
- Molnar, P., Atwater, T., Mammerickx, J. & Smith, S. M. (1975). Magnetic anomalies, bathymetry and the tectonic evolution of the South Pacific since the Late Cretaceous. *Geophysical Journal International* **40**, 383–420.
- Mortimer, N., Dunlap, W. J., Isaac, M. J., Sutherland, R. P. & Faure, K. (2007). Basal Adare volcanics. Robertson Bay, North Victoria Land, Antarctica: late Miocene intraplate basalts of subaqueous origin. In: Cooper, A. K. & Raymond, C. R., et al. (eds) *Proceedings of the 10th International Symposium on Antarctic Earth Sciences. US Geological Survey Open-File Report 2007-1047*, Short Research Paper 045, 7 pp.
- Muehlenbachs, K. (1986). Alteration of the oceanic crust and the ¹⁸O history of seawater. In: Valley, J. W., Taylor, H. P., Jr & O’Neil, J. R. (eds) *Stable Isotopes in High Temperature Geological Processes. Mineralogical Society of America, Reviews in Mineralogy* **16**, 425–444.
- Mukasa, S. B. & Dalziel, I. W. D. (2000). Marie Byrd Land, West Antarctica: evolution of Gondwana’s Pacific margin constrained by zircon U–Pb geochronology and feldspar common-Pb isotopic compositions. *Geological Society of America Bulletin* **112**, 611–627.
- Müller, P., Schmidt-Thomé, M., Kreuzer, H., Tessensohn, H. & Vetter, U. (1991). Cenozoic peralkaline magmatism at the western margin of the Ross Sea, Antarctica. *Memorie della Società Geologica Italiana* **46**, 315–336.
- Müller, R. D., Cande, S. C., Stock, J. M. & Keller, W. R. (2005). Crustal structure and rift flank uplift of the Adare Trough,

- Antarctica. *Geochemistry, Geophysics, Geosystems* **6**, doi: 10.1029/2005GC001027.
- Münker, C., Pfänder, J. A., Weyer, S., Büchl, A., Kleine, T. & Mezger, K. (2003). Evolution of planetary cores and the Earth–Moon system from Nb/Ta systematics. *Science* **301**, 84–87.
- Nardini, I., Armienti, P., Rocchi, S. & Burgess, R. (2003). ^{40}Ar – ^{39}Ar chronology and petrology of the Miocene rift-related volcanism of Daniell Peninsula (Northern Victoria Land, Antarctica). *Terra Antarctica* **10**, 39–62.
- Nardini, I., Armienti, P., Rocchi, S., Dallai, L. & Harrison, D. (2009). Sr–Nd–Pb–He–O isotope and geochemical constraints on the genesis of Cenozoic magmas from the West Antarctic Rift. *Journal of Petrology* **50**, 1359–1375.
- Njome, M. S. & de Wit, M. J. (2014). The Cameroon Line: analysis of an intraplate magmatic province transecting both oceanic and continental lithospheres: constraints, controversies and models. *Earth-Science Reviews* **139**, 168–194.
- Olafsson, M. & Eggler, D. H. (1983). Phase relations of amphibole, amphibole–carbonate, and phlogopite–carbonate peridotite: petrologic constraints on the asthenosphere. *Earth and Planetary Science Letters* **64**, 305–315.
- Panther, K. S. & Castillo, P. (2007). Petrogenesis and source of lavas from seamounts in the Adare Basin, Western Ross Sea: implications for the origin of Cenozoic magmatism in Antarctica. In: Cooper, A. K. & Raymond, C. R., *et al.* (eds) *Proceedings of the 10th International Symposium on Antarctic Earth Sciences. US Geological Survey Open-File Report 2007-1047*, Extended Abstract 069, 4 pp.
- Panther, K. S. & Castillo, P. (2008). Petrology and source of lavas from seamounts in the Adare Basin, western Ross Sea: implications for the origin of Cenozoic magmatism in Antarctica. *EOS Transactions, American Geophysical Union* **89**, Fall Meeting Abstract V11F-05.
- Panther, K. S., Kyle, P. R. & Smellie, J. L. (1997). Petrogenesis of a phonolite–trachyte succession at Mount Sidley, Marie Byrd Land, Antarctica. *Journal of Petrology* **38**, 1225–1253.
- Panther, K. S., Hart, S. R., Kyle, P., Blusztajn, J. & Wilch, T. (2000). Geochemistry of late Cenozoic basalts from the Cray Mountains: characterization of mantle sources in Marie Byrd Land, Antarctica. *Chemical Geology* **165**, 215–241.
- Panther, K. S., Blusztajn, J., Wingrove, D., Hart, S. & Matthey, D. (2003). Sr, Nd, Pb, Os, O isotope, major and trace element data from basalts, South Victoria Land, Antarctica: evidence for open-system processes in the evolution of mafic alkaline magmas. *European Geophysical Society, Geophysical Research Abstracts* **5**, 07583.
- Panther, K. S., Blusztajn, J., Hart, S., Kyle, P., Esser, R. & McIntosh, W. (2006). The origin of HIMU in the SW Pacific: evidence from intraplate volcanism in Southern New Zealand and Subantarctic Islands. *Journal of Petrology* **47**, 1673–1704.
- Panther, K. S., Castillo, P. & McIntosh, W. C. (2011). Geochemical variations in alkaline magmas of HIMU affinity from continent to ocean, northwestern Ross Sea, Antarctica—constraints on mantle source, flow and melting for volcanism. *International Symposium on Antarctic Earth Science (ISAES) XI*, 10–15 July, Edinburgh, Scotland, Abstract PS5.9.
- Panther, K., Castillo, P., Krans, S. & McIntosh, W. (2016). Melt origin across a rifted continental edge: ^{40}Ar / ^{39}Ar geochronology, geochemistry and Sr–Nd–O isotope systematics of alkaline basalts, northwestern Ross Sea. *XXXIV SCAR Open Science Conference*, 22–26 August, Kuala Lumpur, Malaysia.
- Peate, D. W., Baker, J. A., Jakobsson, S. P., Waight, T. E., Kent, A. J. R., Grassineau, N. V. & Skovgaard, A. C. (2009). Historic magmatism on the Reykjanes Peninsula, Iceland: a snap-shot of melt generation at a ridge segment. *Contributions to Mineralogy and Petrology* **157**, 359–382.
- Perinelli, C., Armienti, P. & Dallai, L. (2006). Geochemical and O-isotope constraints on the evolution of lithospheric mantle in the Ross Sea rift area (Antarctica). *Contributions to Mineralogy and Petrology* **151**, 245–266.
- Perinelli, C., Armienti, P. & Dallai, L. (2011). Thermal evolution of the lithosphere in a rift environment as inferred from the geochemistry of mantle cumulates, Northern Victoria Land, Antarctica. *Journal of Petrology* **52**, 665–690.
- Perinelli, C., Gaeta, M. & Armienti, P. (2017). Cumulate xenoliths from Mt. Overlord, northern Victoria Land, Antarctica: a window into high pressure storage and differentiation of mantle-derived basalts. *Lithos* **268–271**, 225–239.
- Pertermann, M., Hirschmann, M. M., Hametner, K., Günther, D. & Schmidt, M. W. (2004). Experimental determination of trace element partitioning between garnet and silica-rich liquid during anhydrous partial melting of MORB-like eclogite. *Geochemistry, Geophysics, Geosystems* **5**, doi: 10.1029/2003GC000638.
- Peters, B. J. & Day, J. M. D. (2014). Assessment of relative Ti, Ta, and Nb (TITAN) enrichments in ocean island basalts. *Geochemistry, Geophysics, Geosystems* **15**, 4424–4444.
- Pfänder, J. A., Münker, C., Stracke, A. & Mezger, K. (2007). Nb/Ta and Zr/Hf in ocean island basalts—implications for crust–mantle differentiation and the fate of niobium. *Earth and Planetary Science Letters* **254**, 158–172.
- Pfänder, J. A., Jung, S., Münker, C., Stracke, A. & Mezger, K. (2012). A possible high Nb/Ta reservoir in the continental lithospheric mantle and consequences on the global Nb budget—evidence from continental basalts from Central Germany. *Geochimica et Cosmochimica Acta* **77**, 232–251.
- Pilet, S. (2015). Generation of low-silica alkaline lavas: petrological constraints, models, and thermal implications. In: Foulger, G.R., Lustrino, M. & King, S. D. (eds) *The Interdisciplinary Earth: In Honor of Don L. Anderson. Geological Society of America, Special Papers* **514**, 514–517.
- Pilet, S., Hernandez, J., Bussy, F. & Sylvester, P. J. (2004). Short-term metasomatic control of Nb/Th ratios in the mantle sources of intraplate basalts. *Geology* **32**, 113.
- Pilet, S., Hernandez, J., Sylvester, P. & Poujol, M. (2005). The metasomatic alternative for ocean island basalt chemical heterogeneity. *Earth and Planetary Science Letters* **236**, 148–166.
- Pilet, S., Baker, M. B. & Stolper, E. M. (2008). Metasomatized lithosphere and the origin of alkaline lavas. *Science* **320**, 916–919.
- Pilet, S., Ulmer, P. & Villiger, S. (2010). Liquid line of descent of a basanitic liquid at 1.5 GPa: constraints on the formation of metasomatic veins. *Contributions to Mineralogy and Petrology* **159**, 621–643.
- Pilet, S., Baker, M. B., Muntener, O. & Stolper, E. M. (2011). Monte Carlo simulations of metasomatic enrichment in the lithosphere and implications for the source of alkaline basalts. *Journal of Petrology* **52**, 1415–1442.
- Putirka, K. D., Perfit, M., Ryerson, F. J. & Jackson, M. G. (2007). Ambient and excess mantle temperatures, olivine thermometry, and active vs. passive upwelling. *Chemical Geology* **241**, 177–206.
- Putlitz, B., Matthews, A. & Valley, J. W. (2000). Oxygen and hydrogen isotope study of high-pressure metagabbros and metabasalts (Cyclades, Greece): implications for the subduction of oceanic crust. *Contributions to Mineralogy and Petrology* **138**, 114–126.

- Reid, I. & Jackson, H. R. (1981). Oceanic spreading rate and crustal thickness. *Marine Geophysical Researches* **5**, 165–172.
- Renne, P. R., Swisher, C. C., Deino, A. L., Karner, D. B., Owens, T. L. & DePaolo, D. J. (1998). Intercalibration of standards, absolute ages and uncertainties in $^{40}\text{Ar}/^{39}\text{Ar}$ dating. *Chemical Geology* **145**, 117–152.
- Ritzwoller, M. H., Shapiro, N. M., Levshin, A. L. & Leahy, G. M. (2001). Crustal and upper mantle structure beneath Antarctica and surrounding oceans. *Journal of Geophysical Research: Solid Earth* **106**, 30645–30670.
- Rocchi, S., Armienti, P., D'Orazio, M., Tonarini, S., Wijbrans, J. R. & Di Vincenzo, G. (2002). Cenozoic magmatism in the western Ross Embayment: role of mantle plume versus plate dynamics in the development of the West Antarctic Rift System. *Journal of Geophysical Research: Solid Earth* **107**, ECV 5-1–ECV 5-22.
- Rocchi, S., Armienti, P. & Di Vincenzo, G. (2005). No plume, no rift magmatism in the West Antarctic Rift. Plates, plumes and paradigms. In: *Geological Society of America, Special Papers* **388**, 435–447.
- Rocholl, A., Stein, M., Molzahn, M., Hart, S. R. & Wörner, G. (1995). Geochemical evolution of rift magmas by progressive tapping of a stratified mantle source beneath the Ross Sea Rift, Northern Victoria Land, Antarctica. *Earth and Planetary Science Letters* **131**, 207–224.
- Rooney, T. O., Nelson, W. R., Dosso, L., Furman, T. & Hanan, B. (2014). The role of continental lithosphere metasomes in the production of HIMU-like magmatism on the northeast African and Arabian plates. *Geology* **42**, 419–422.
- Rooney, T. O., Nelson, W. R., Ayalew, D., Hanan, B., Yirgu, G. & Kappelman, J. (2017). Melting the lithosphere: metasomes as a source for mantle-derived magmas. *Earth and Planetary Science Letters* **461**, 105–118.
- Rudnick, R. L., Barth, M., Horn, I. & McDonough, W. F. (2000). Rutile-bearing refractory eclogites: missing link between continents and depleted mantle. *Science* **287**, 278–281.
- Salimbeni, S., Pondrelli, S., Danesi, S. & Morelli, A. (2010). Seismic anisotropy of the Victoria Land region, Antarctica: seismic anisotropy beneath West Antarctica. *Geophysical Journal International* **182**, 421–432.
- Scott, J. M., Waight, T. E., van der Meer, Q. H. A., Palin, J. M., Cooper, A. F. & Münker, C. (2014). Metasomatized ancient lithospheric mantle beneath the young Zealandia microcontinent and its role in HIMU-like intraplate magmatism. *Geochemistry, Geophysics, Geosystems* **15**, 3477–3501.
- Selvans, M. M., Clayton, R. W., Stock, J. M. & Granot, R. (2012). Using overlapping sonobuoy data from the Ross Sea to construct a 2D deep crustal velocity model. *Marine Geophysical Research* **33**, 17–32.
- Selvans, M. M., Stock, J. M., Clayton, R. W., Cande, S. & Granot, R. (2014). Deep crustal structure of the Adare and Northern Basins, Ross Sea, Antarctica, from sonobuoy data. *Earth and Planetary Science Letters* **405**, 220–230.
- Shaw, C. S. (1999). Dissolution of orthopyroxene in basanitic magma between 0.4 and 2 GPa: further implications for the origin of Si-rich alkaline glass inclusions in mantle xenoliths. *Contributions to Mineralogy and Petrology* **135**, 114–132.
- Shaw, C. S., Thibault, Y., Edgar, A. D. & Lloyd, F. E. (1998). Mechanisms of orthopyroxene dissolution in silica-undersaturated melts at 1 atmosphere and implications for the origin of silica-rich glass in mantle xenoliths. *Contributions to Mineralogy and Petrology* **132**, 354–370.
- Sisson, T. W. & Grove, T. L. (1993). Experimental investigations of the role of H_2O in calc-alkaline differentiation and subduction zone magmatism. *Contributions to Mineralogy and Petrology* **113**, 143–166.
- Skovgaard, A. C., Storey, M., Baker, J., Blusztajn, J. & Hart, S. R. (2001). Osmium–oxygen isotopic evidence for a recycled and strongly depleted component in the Iceland mantle plume. *Earth and Planetary Science Letters* **194**, 259–275.
- Smellie, J. L., Rocchi, S., Gemelli, M., Di Vincenzo, G. & Armienti, P. (2011). A thin predominantly cold-based Late Miocene East Antarctic ice sheet inferred from glaciovolcanic sequences in northern Victoria Land, Antarctica. *Palaeogeography, Palaeoclimatology, Palaeoecology* **307**, 129–149.
- Stein, M., Navon, O. & Kessel, R. (1997). Chromatographic metasomatism of the Arabian–Nubian lithosphere. *Earth and Planetary Science Letters* **152**, 75–91.
- Storey, B. C. & Kyle, P. R. (1997). An active mantle mechanism for Gondwana breakup. *South African Journal of Geology* **100**, 283–290.
- Storey, B. C., Leat, P. T., Weaver, S. D., Pankhurst, R. J., Bradshaw, J. D. & Kelley, S. (1999). Mantle plumes and Antarctica–New Zealand rifting: evidence from mid-Cretaceous mafic dykes. *Journal of the Geological Society, London* **156**, 659–671.
- Stracke, A. (2012). Earth's heterogeneous mantle: a product of convection-driven interaction between crust and mantle. *Chemical Geology* **330–331**, 274–299.
- Stracke, A., Hofmann, A. W. & Hart, S. R. (2005). FOZO, HIMU, and the rest of the mantle zoo. *Geochemistry, Geophysics, Geosystems* **6**, Q05007, doi:10.1029/2004GC000824.
- Stump, E. (1995) *The Ross Orogen of the Transantarctic Mountains*. Cambridge University Press, 284 pp.
- Sumino, H., Burgess, R., Mizukami, T., Wallis, S. R., Holland, G. & Ballentine, C. J. (2010). Seawater-derived noble gases and halogens preserved in exhumed mantle wedge peridotite. *Earth and Planetary Science Letters* **294**, 163–172.
- Sun, S.-S. & McDonough, W. F. (1989). Chemical and isotopic systematics of oceanic basalts: implications for mantle composition and processes. In: Saunders, A. D. & Norry, M. J. (eds) *Magmatism in the Ocean Basins*. Geological Society, London, *Special Publications* **42**, 313–345.
- Sutherland, R., Spasojevic, S. & Gurnis, M. (2010). Mantle upwelling after Gondwana subduction death explains anomalous topography and subsidence histories of eastern New Zealand and West Antarctica. *Geology* **38**, 155–158.
- Thirlwall, M. F. (1997). Pb isotopic and elemental evidence for OIB derivation from young HIMU mantle. *Chemical Geology* **139**, 51–74.
- Tiepolo, M., Oberti, R., Zanetti, A., Vannucci, R., Foley, S. F. (2007). Trace-element partitioning between amphibole and silicate melt. In: Hawthorne, F. C., Oberti, R., Della Ventura, G. & Mottana, A. (eds) *Amphiboles: Crystal Chemistry, Occurrence and Health Issues*. Mineralogical Society of America and Geochemical Society, *Reviews in Mineralogy and Geochemistry* **67**, 417–452.
- Timm, C., Hoernle, K., Werner, R., Hauff, F., van den Bogaard, P., White, J., Mortimer, N. & Garbe-Schönberg, D. (2010). Temporal and geochemical evolution of the Cenozoic intraplate volcanism of Zealandia. *Earth-Science Reviews* **98**, 38–64.
- Todt, W., Cliff, R. A., Hanser, A. & Hoffman, A. W. (1996). Evaluation of a ^{202}Pb – ^{205}Pb double spike for high-precision lead isotope analysis. In: Basu, A. & Hart, S. (eds) *Earth Processes: Reading the Isotopic Code*. *Geophysical Monograph, American Geophysical Union* **95**, 429–437.
- Tonarini, S., Rocchi, S., Armienti, P. & Innocenti, F. (1997). Constraints on timing of Ross Sea rifting inferred from Cainozoic intrusions from northern Victoria Land, Antarctica. In: Ricci, C. A. (ed.) *The Antarctic Region: Geological Evolution and Processes, Proceedings of the 7th*

- International Symposium on Antarctic Earth Sciences*. Terra Antarctica, pp. 511–521.
- Tulloch, A. J., Ramezani, J., Mortimer, N., Mortensen, J., van den Bogaard, P. & Maas, R. (2009). Cretaceous felsic volcanism in New Zealand and Lord Howe Rise (Zealandia) as a precursor to final Gondwana break-up. In: Ring, U. & Wernicke, B. (eds) *Extending a Continent: Architecture, Rheology and Heat Budget*. Geological Society, London, *Special Publications* 321, 89–118.
- Valley, J. W. & Kita, N. T. (2009). *In situ* oxygen isotope geochemistry by ion microprobe. In: Fayek, M. (ed) *Secondary Ion Mass Spectrometry in the Earth Sciences: Gleaning the Big Picture from a Small Spot*. Mineralogical Association of Canada, *Short Course Series* 41, 19–63.
- Valley, J. W., Kitchen, N. E., Kohn, M. J., Niendorf, C. R. & Spicuzza, M. J. (1995). UWG-2, a garnet standard for oxygen isotope ratio: strategies for high precision and accuracy with laser heating. *Geochimica et Cosmochimica Acta* 59, 5223–5231.
- van der Meer, Q. H. A., Waight, T. E., Scott, J. M. & Münker, C. (2017). Variable sources for Cretaceous to recent HIMU and HIMU-like intraplate magmatism in New Zealand. *Earth and Planetary Science Letters* 469, 27–41.
- Vaughan, A. P. & Storey, B. C. (2007). A new supercontinent self-destruct mechanism: evidence from the Late Triassic–Early Jurassic. *Journal of the Geological Society, London* 164, 383–392.
- Vaughan, A. P. M. & Pankhurst, R. J. (2008). Tectonic overview of the West Gondwana margin. *Gondwana Research* 13, 150–162.
- Veevers, J. J. (2012). Reconstructions before rifting and drifting reveal the geological connections between Antarctica and its conjugates in Gondwanaland. *Earth-Science Reviews* 111, 249–318.
- Walter, M. J. (1998). Melting of garnet peridotite and the origin of komatiite and depleted lithosphere. *Journal of Petrology* 39, 29–60.
- Wang, X.-L., Coble, M. A., Valley, J. W., Shu, X.-J., Kitajima, K., Spicuzza, M. J. & Sun, T. (2014). Influence of radiation damage on late Jurassic zircon from southern China: evidence from *in situ* measurement of oxygen isotopes, laser Raman, U–Pb ages, and trace elements. *Chemical Geology* 389, 122–136.
- Wang, Z. & Eiler, J. (2008). Insights into the origin of low- $\delta^{18}\text{O}$ basaltic magmas in Hawaii revealed from *in situ* measurements of oxygen isotope compositions of olivines. *Earth and Planetary Science Letters* 269, 377–387.
- Weaver, B. L. (1991). The origin of ocean island basalt end-member compositions: trace element and isotopic constraints. *Earth and Planetary Science Letters* 104, 381–397.
- Weaver, S. D., Storey, B. C., Pankhurst, R. J., Mukasa, S. B., DiVenere, V. J. & Bradshaw, J. D. (1994). Antarctica–New Zealand rifting and Marie Byrd Land lithospheric magmatism linked to ridge subduction and mantle plume activity. *Geology* 22, 811–814.
- Weiss, Y., Class, C., Goldstein, S. L. & Hanyu, T. (2016). Key new pieces of the HIMU puzzle from olivines and diamond inclusions. *Nature* 537, 666–670.
- White, W. M. (2015). Probing the earth's deep interior through geochemistry. *Geochemical Perspectives* 4, 251.
- Willbold, M. & Stracke, A. (2010). Formation of enriched mantle components by recycling of upper and lower continental crust. *Chemical Geology* 276, 188–197.
- Yaxley, G. M. & Green, D. H. (1998). Reactions between eclogite and peridotite: mantle refertilisation by subduction of oceanic crust. *Schweizerische Mineralogische und Petrographische Mitteilungen* 78, 243–255.
- Zheng, Y.-F., Fu, B., Li, Y., Xiao, Y. & Li, S. (1998). Oxygen and hydrogen isotope geochemistry of ultrahigh-pressure eclogites from the Dabie Mountains and the Sulu terrane. *Earth and Planetary Science Letters* 155, 113–129.
- Zheng, Y.-F., Fu, B., Gong, B. & Li, L. (2003). Stable isotope geochemistry of ultrahigh pressure metamorphic rocks from the Dabie–Sulu orogen in China: implications for geodynamics and fluid regime. *Earth-Science Reviews* 62, 105–161.
- Zindler, A. & Hart, S. (1986). Chemical geodynamics. *Annual Review of Earth and Planetary Sciences* 14, 493–571.

